Epitaxial growth of Si and 3C-SiC by Chemical Vapor Deposition

Gilberto Vitor Zaia

Walter Schottky Institut
Technische Universität München

Epitaxial growth of Si and 3C-SiC by Chemical Vapor Deposition

Gilberto Vitor Zaia

Vollständiger Abdruck der von der Fakultät für Physik der Technischen Universität München zur Erlangung des akademischen Grades eines

Doktors der Naturwissenschaft

genehmigten Dissertation.

Vorsitzender:	Univ.-Prof. Dr. A. Groß
Prüfer der Dissertation:	1. Univ.-Prof. Dr. M. Stutzmann
	2. Univ.-Prof. Dr. W. Hiller

Die Dissertation wurde am 01.10.2002 bei der Technischen Universität München eingereicht und durch die Fakultät für Physik am 04.12.2002 angenommen.

O perfume sempre perdura na mão que deu a flor.

The perfume always lasts in the hand that offers the flower.

Der Duftstoff bleibt immer an der Hand, welche die Blume anbietet.

for my parents

Summary

This dissertation investigates the heteroepitaxy of 3C-SiC on Si (100)-substrates with an halogenic organosilicon precursor (MTS) and the growth of Si on Si (100)-substrates, with new precursors for selective deposition.

In first part of this work, the production of high quality 3C-SiC single crystal films with MTS is described. The MTS precursor is easy to handle and economically interesting as it is a by-product of the silicone industry. Silicon and carbon are present in the MTS molecule in an optimal 1:1 stoichiometric ratio. This is an advantage compared to the Buffer layer growth method using silicon and carbon provided by different molecules (such as C_3H_8 and SiH_4). Contrarily, to the formerly used APCVD method, the 3C-SiC films obtained in this work were homogeneous and can be deposited on large area Si-substrates. Furthermore, the substrate temperature during growth with the MTS precursor could be reduced by about 200 °C in comparison to the buffer layer method. This reduces crystal defects in the SiC film.

Many relevant factors were investigated to obtain high quality films of 3C-SiC:

-Temperature distribution in the deposition system, mainly at the substrate.

-Temperature ramps until the growth temperature has been reached.

-Flux and pressures of the precursor MTS and H_2.

-Proportion between MTS and H_2.

-Cleanliness of the system.

-Quality of the substrate surface.

The structure of the deposited 3C-SiC films were analyzed by XRD, Raman and PL spectroscopy, SEM, SAX, UV spectroscopy, Hall effect measurements and TEM. It could be demonstrated that the concentration of defects at the interface of the 3C-SiC film and the Si substrate is very high, as expected due to the high lattice mismatch and different thermal expansion coefficients of SiC and Si. The defect concentration decreases significantly by growing films thicker than 10 μm.

The second part of this work focuses on experiments with three newly developed silylene precursors. The characteristics of these precursors and the possibility of selective growth of a Si film via OMCVD were examined.

The utilization of these new precursors for Si homoepitaxy in substitution of the poisonous and explosive silane gas presents an interesting alternative for Si-device processing in industry.

Polycrystalline Si films were obtained with silylene diazide at a temperature of about 650 °C and with silylene dihydride at a temperature of about 500 °C. Many similarities between films grown with silylene and films grown with its germanium analogue (germylene) could be recognized.

The deposited Si films were characterized with SEM, XPS, XRD, EDX and did not show signs of delamination or cracking, but rather a good homogeneity and high mechanical stability.

These first results with the new precursors are promising and motivate further investigation for obtaining single crystal films on planar and pre-structured Si surfaces.

Zusammenfassung

Diese Dissertation behandelt zum einen die heteroepitaktische Abscheidung von 3C-SiC auf Si(100)-Substraten aus halogenierten Organosilizium-Verbindungen und zum anderen die Abscheidung von Si auf Si(100)-Substraten unter Einbeziehung von neuentwickelten Siliziumverbindungen.

Im ersten Teil dieser Arbeit werden hochwertige 3C-SiC-Schichten durch die Verwendung des MTS Precursors erzeugt. Diese Verbindung, ein preisgünstiges Nebenprodukt der Silikon-Industrie, erlaubt eine einfache Handhabung des CVD-Prozesses, da Silizium und Kohlenstoff im Ausgangsmolekül im stöchiometrisch optimalen Verhältnis von 1:1 enthalten sind. Im Vergleich dazu werden in herkömmlichen Bufferlayer-Prozessen Ausgangsverbindungen eingesetzt, die Silizium und Kohlenstoff durch unterschiedliche Moleküle (z.B. C_3H_8 und SiH_4) bereitstellen. Der Einsatz des LPCVD-Verfahrens zur Abscheidung von 3C-SiC ermöglicht im Vergleich zum bekannten APCVD-Prozeß eine homogenere Abscheidung, besonders auch auf großflächigen Si-Substraten. Schließlich verbessert auch die Reduzierung der Substrattemperatur um ca. 200 °C die Qualität der Abscheidung.

Die erfolgreiche Heteroepitaxie wurde durch die Untersuchung folgender Parameter ermöglicht:

-Temperaturen im gesamten System, besonders am Substrat.

-Temperaturrampen bis zum Erreichen der Abscheidetemperatur

-Durchflussgeschwindigkeiten und Partialdrücke des Precursors MTS und von H_2.

-Volumenanteile von MTS und H_2

-Reinheit des gesamten Aufbaus

-Qualität der Substratoberfläche.

Die Struktur der abgeschiedenen 3C-SiC Filme wurde durch Röntgendiffraktion, Raman- und Photolumineszenzspektroskopie, Rasterelektronenmikroskopie, SAX, Messungen der Leitfähigkeit und des Hallefekts, UV-Spektroskopie und TEM untersucht. Dabei zeigte sich, dass die Kristalldefekte hauptsächlich durch schlechte Gitteranpassung und durch die unterschiedlichen thermischen Ausdehnungskoeffizienten von SiC und Si an der Grenzfläche zwischen der abgelagerten Schicht und dem Substrat verursacht werden. Die Defektdichte nimmt dabei deutlich mit zunehmendem Abstand von der Si/SiC-Grenzfläche ab.

Im zweiten Teil dieser Arbeit werden Experimente mit drei neuen Silylene Precursoren und deren Resultate beschrieben. Die Charakterisierung dieser Verbindungen und die selektive Herstellung von Si-Schichten durch Verwendung von OMCVD standen dabei im Mittelpunkt.

Die Nutzung der neuen Precursoren als eine Alternative zum giftigen und explosiven Silan Gas stellt eine interessante Perspektive zur Herstellung von Si-Bauteilen dar.

Mit Erfolg wurden polykristallinen Schichten auf Si(100) bei der Verwendung des Precursors Silylene Diazide bei einer Temperatur von 650 °C und des Precursors Silylene Dihydride bei einer Temperatur von 500 °C realisiert. Desweiteren wurden Gemeinsamkeiten zwischen den Abscheidemechanismen bei der Verwendung von Silylene und dessen Germanium-Gegenstück (Germylene) betrachtet.

Die abgeschiedenen Si-Schichten wurden mittels SEM, XPS, XRD und EDX untersucht und zeigten eine hohe Homogenität und große mechanische Stabilität, ohne Risse.

Die ersten Resultate mit den neuen Precursoren sind vielversprechend und motivieren zu weiteren Untersuchungen der Herstellung von Einkristallfilmen auf ebenen und auch strukturierten Si-Oberflächen.

Glossary

AES	Auger Electron Spectroscopy
AMU	Atomic Mass Unit
APB	Antiphase Boundaries
APCVD	Atmospheric Pressure Chemical Vapor Deposition
CVD	Chemical Vapor Deposition
DPB	Double Position Boundaries
$\Delta G°$	Free Reaction Enthalpy
E_b	Breakdown Field
EDX	Energy Dispersive X-ray Analysis
E_g	Band Gap
ε	Dielectric Constant
ESR	Electron Spin Resonance
FWHM	Full Width at Half Maximum
G_L	Channel Gate Length
HJBT	Heterojunction Bipolar Transistor
HMDSO	Hexamethyldisiloxane
HRXRD	Highly Resolution X-ray Diffraction
IUPAC	International Union of Pure and Applied Chemistry
JFM	Johnson's Figure of Merit
JFETs	Junction Field Effect Transistor
KFM	Keye's Figure of Merit
λ	Wavelength
LED	Light Emitting Diode
LEED	Low Energy Electron Diffraction
LA	Longitudinal Acoustic
LO	Longitudinal Optical
LPCVD	Low Pressure Chemical Vapor Deposition
LPE	Liquid Phase Epitaxy
μ_e	Electron Mobility
μ_H	Hall Electron Mobility
m_e*	Electron Effective Mass
m_l*	Longitudinal Effective Mass
m_t	Transversal Effective Mass
MBE	Molecular Beam Epitaxy

MIBE	Molecular and Ion Beam Epitaxy
MESFET	Metal Semiconductor Field Effect Transistor
MOSFET	Metal Oxide Semiconductor Field Effect Transistor
MTS	Methyltrichlorosilane
NVRAMs	Non Volatile Random Access Memory
OMCVD	Organic Metal Chemical Vapor Deposition
PECVD	Plasma Enhanced Chemical Vapor Deposition
PL	Photoluminescence
QMS	Quadrupole Mass Spectrometer
RIE	Reactive Ion Etching
RMS	Reactive Magnetron Sputtering
r.u.	Reference Unit
ρ	Specific Resistivity
R_s	Serial Resistance
R_w	Silicon Substrate Resistance
SAX	Small Angle X-ray
SEM	Scanning Electron Microscopy
TA	Transversal Acoustic
TEOS	Tetraorthosilicate
THF	Tetrahydrofuran
TO	Transversal Optical
σ_T	Thermal Conductivity
σ	Electrical Conductivity
T_{max}	Maximum work temperature
TEM	Transmission Electron Microscopy
UHV	Ultra High Vacuum
UV	Ultraviolet
v_{sat}	Saturation Velocity
XPS	X-ray Photoelectron Spectroscopy
XRD	X-ray Diffraction
ZPL	Zero Phonon Line

-PART I-

Epitaxial growth of 3C-SiC by LPCVD

- PART II -

Silicon crystal growth by OMCVD

Part I

Epitaxial growth of 3C-SiC by LPCVD

1 Introduction to SiC Deposition

1.1 SiC Properties

The development of semiconductors is important for advances in computer science, electronics and optoelectronics. Semiconductor products have been integrated into every aspect of modern society. For demanding operating conditions such as high voltage, high frequency, high temperature, aggressive chemical environment and radioactivity, SiC is an excellent solution including properties that tolerate these extreme conditions.

Particular properties of interest of SiC are large band gap, a high breakdown field, a high thermal conductivity and an excellent mechanical and chemical stability.

Tab. 1.1 shows significant properties of 3C-SiC compared with another semiconductors.

Semiconductor	Si	GaAs	3C-SiC	4H-SiC	6H-SiC	GaN	Diamond
Specific density [$g \cdot cm^{-3}$]	2.33	5.32	3.21	-	3.21	6.1	3.51
Lattice constant [Å]	5.43	5.65	4.36	3.07	3.08	3.19	3.57
Vickers hardness [$kg \cdot mm^{-2}$]	1000	600	2600	2600	2600	-	10000
Band gap (Eg) [eV] 300 K	1.12	1.43	2.41	3.26	3.02	3.39	5.45
v_{sat} [$10^7 cm.s^{-1}$]	1.0	2.0	2.5	2.0	2.0		2.7.
T_{max} [K]	600	760	1200	-	1580	1100	1400
Melting point [K]	1690	1510	3000	3000	3000	1123	3820
Mechanical stability	High	Medium	High	High	High	High	High
n-mobility [$cm^2(Vs)^{-1}$]	1400	8500	1000	460	600	900	2200
p-mobility [$cm^2(Vs)^{-1}$]	600	400	40	115	50	150	1600
Breakdown electric field (E_b) [10^6 $V \cdot cm^{-1}$]	0.3	0.4	2.2	4	2.4	5	10
Thermal Conductivity [$W \cdot (cmK)^{-1}$]	1.45	0.46	4.9	3.7	4.9	1.3	20
Dielectric constant	11.8	12.8	9.7	-	9.66	9	5.5

(T_{max} = Maximum work temperature)

Tab. 1.1: Some properties (E_g: Band gap, v_{sat}: Saturation velocity, σ_T: Thermal conductivity, E_b: Breakdown field and ε: Relative dielectric constant) of 3C-SiC (cubic Silicon Carbide), in comparison to other semiconductors (4H-SiC, 6H-SiC, GaN, Si, GaAs and Diamond) [Pa 85] at ambient temperature.

To compare commounly used semiconductors, a parameter called "Figure of merit" is introduced. Fig. 1.1 shows an example of the application of the "Figure of merit" by Johnson [Jo 65] and Keyes [Ke 72].

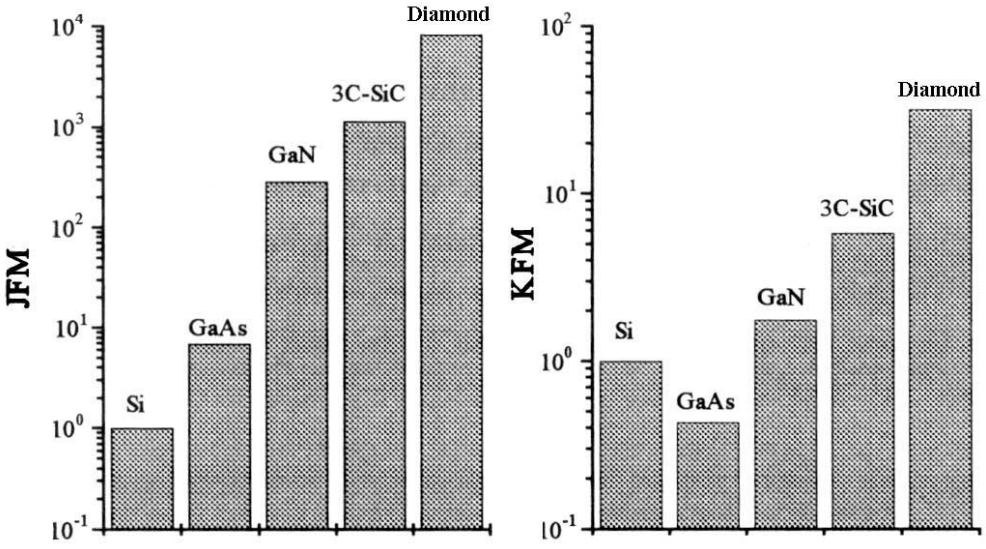

Fig. 1.1: Johnson's and Key's "Figure of merit" (JFM) [Da 92]

Johnson's "Figure of merit" (JFM) is based on E_b (breakdown field) and v_{sat} (saturation velocity)**.**

$$\text{JFM} = \frac{E_b^{\,2} \cdot v_{SAT}^{\,2}}{4\pi^2} \qquad \text{Eq. 1.1}$$

Keye´s "Figure of merit" (KFM) is based on the thermal conductivity σ_T, saturation velocity v_{sat} and relative dielectric constant, which are important for integrated circuits:

$$\text{KFM} = \sigma_T \cdot \left(\frac{V_{SAT} \cdot \varepsilon_0}{\varepsilon} \right)^{1/2} \qquad \text{Eq. 1.2}$$

According to Fig. 1.1, 3C-SiC is only exceeded in performance by diamond. The intrinsic properties of diamond such as electron mobility, electron concentration and thermal conductivity make it advantageous at room temperature. However is difficult to produce efficient n-type diamond [Ji 93], [Sa 95].

SiC as a material for electronic devices has a high development potential in modern microelectronics including high temperature applications.

The main problem in the production of SiC devices is the high cost involved in the epitaxial growth. Using the improved production process elucidated in the experimental part of this thesis can solve this problem. After the discovery of electroluminescence in SiC [Ro 07], it took almost 50 years until Lely [Le 55] produced SiC crystallites with various polytypes by a sublimation process. With the modification of the Lely technique, Tairov and Tsvertkov [Ta 78] produced SiC as a single crystal polytype on Si with a diameter of 8 mm. By using heteroepitaxial CVD with new precursors on Si, Nishino [Ni 83] was able to develop 3C-SiC in recent years.

There have been many publications on the subject of SiC in the last 10 years. Currently, it is possible to buy single crystalline wafers with different polytype. Cree Research Inc. offers SiC wafers for US$ 700 to 3200 depending on the size, polytype and doping. Hoya Corporation offers 5µm thick epitaxial films of 3C-SiC on Si for the production of microelectronics devices and sensors.

The first commercial electronic components made from SiC were LEDs, produced in a wide variety of types. They are produced and marketed by Siemens, Cree Research and Sanyo. For special applications, several SiC electronic devices are produced, e.g. Schottky diodes, MOSFETs, JFETs, MESFETs, UV-sensors, 3C-SiC/Si solar cells and NVRAMs.

Due to many technical difficulties of producing high quality single crystal material, new techniques were developed to optimize several physical parameters, in order to obtain the required high crystal quality. The reasons for these technical difficulties during the production of single crystal SiC with high quality are listed below:

- SiC has more than 200 crystal polytypes with different physical properties. The control of the polytype during crystal growth is very difficult, because the energy difference between polytypes is small. Until now, it has been problematic to grow a thick single crystal of cubic SiC.

- The difference between the lattice constant of the Si substrate and the epitaxial SiC layer causes stress and a high defect density particularly at the region near the interface.

- The precise reaction mechanism of SiC growth is not known.

For CVD, it is still not clear what happens from the time of introduction of the reaction gases to the time when they produce the SiC layer at the reaction site. There are many factors, which are still unknown [Ja 71,Ma 78, Mo 74,Ni 80].

After the initial success of Nishino [Ni 83] by employing Si substrate carbonization, there have been modifications by different research groups in the last 20 years [Ad 84, Bo 85, Ch 90, Ik 91, Ko 95, Li 95, Ni 87, Po 87, Sh 87, St 92a, St 92b, Ta 92, Yu 94, Zo 95, Da 01, Vo 01, Ra 01, Ch 01]. A main problem is that at 1350°C the carbonization process simultaneously produces defects (crystal defects, such as stacking faults, dislocations and voids), which are not compatible with current semiconductor technology.

One way to solve this problem is to decrease the growth temperature. This requires a new precursor with a weaker bond between Si and C and, consequently, smaller activation energy of the reaction.

To date those precursors tested include methylsilane [Go 92, Kr 95a, Oh 95] methyldisilane, methyltrichlorosilane [Ch 93, Ch 95, Ni 89, So 88], tetramethylsilane [He 93, Ro 95], hexamethyldisilane [No 95, Ta 92, Wu 96] and silanecyclobutane [Yu 94, St 93].

Some of these precursors have silicon and carbon in the stoichiometric proportion 1:1, which, in theory, is the most promising for SiC deposition.

The reproducibility of the SiC deposition and optimization of deposition parameters was verified in this thesis. The improved film quality and, prospectively, the development made in this dissertation can be used by industrial SiC film manufacturers in single crystal SiC production.

1.1.1 Polytypes

SiC is the most stable compound of carbon and silicon. The crystal structure of SiC is the compact form of double layers of Si and C. The bond between Si and C is 88 % covalent and 12 % ionic, with a bond length of 1.89 Å. Through sp^3 hybridization, each Si atom is surrounded by 4 C atoms and vice versa. This results in the fundamental tetrahedral structure of all SiC polytypes.

There are several ways to describe the SiC polytypes. One of them is called hexagonality percentage. For example, the 6H-polytype has 33% hexagonal character, the 2H-Polytype 100% hexagonal character. The tetrahedron shown in Fig. 1.2 is the fundamental structure of all SiC polytypes.

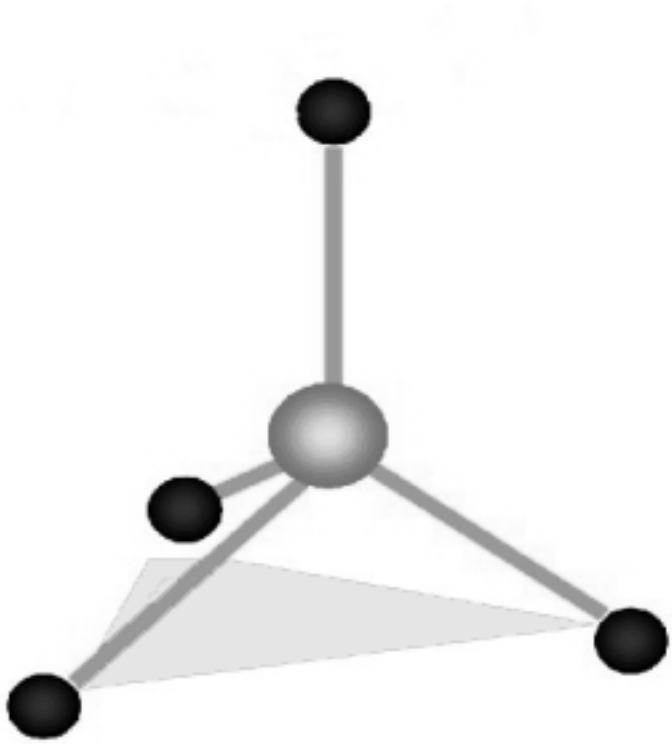

Fig. 1.2: Fundamental structure of SiC.

The symmetry of the hexagonal type is different. In this structure, a crystal is obtained with hexagonal symmetry where every second plane is the same. This polytype is called 2H-SiC (2 Si/C double layers per unit cell, H: Hexagonal). The crystal structures of 3C-SiC and 2H-SiC denominated (β-SiC) are shown below in Fig. 1.3.

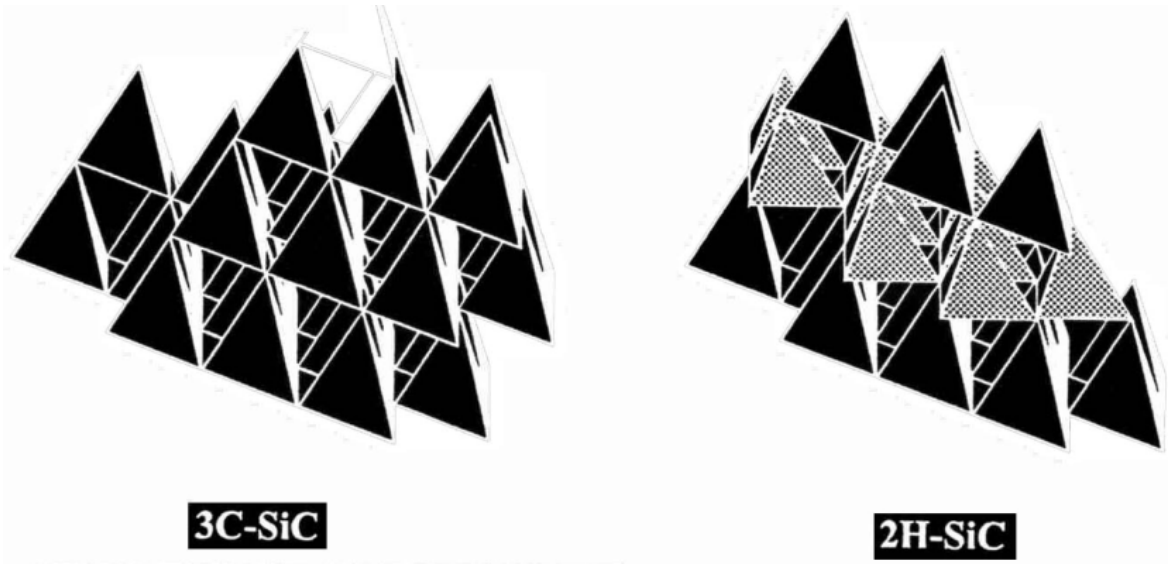

Fig. 1.3: Crystal structures of the 3C-SiC and 2H-SiC.

α-SiC denominated polytypes include more than 70 hexagonal types and 100 SiC rhombohedric types. Tab. 1.2 shows the polytypes of SiC.

Ramsdell	Thibault	Wells	Stacking sequence	Zhdanov	n*	
					c	h
3C-SiC	β-SiC	a	ABC	∞	1	0
2H-SiC	α-SiC	b	AB	11	0	1
4H-SiC	α-SiC	(aabb)	ABCB	22	1	1
6H-SiC	α-SiC	(aaabbb)	ABCACB	33	2	1
15R-SiC	α-SiC	$(aaabb)_3$	ABCBACABACBCCAB	$(23)_3$	3	2

Tab. 1.2: Polytypes of SiC as differentiated by important nomenclatures where n* is the number of inequivalent lattice positions (c cubic and h hexagonal).

For the different crystal types, there are different growth theories, which are separated in two classes:

-Kinetic theory of growth conditions.

-Thermodynamic theory.

To the first group of theories belongs the "Faulted Matrix Model" of Frank [Fr 51], Panday and Krishna [Pa 75, Pa 83]. To the second group belongs the "Jagodzinski Theory" [Ja 54], as well as the "Interlayer Interaction Model" of Cheng [Ch 87, Ch 89]. New work shows that for almost all growth processes, initially there occurs a cubic lattice formation, which converts to hexagonal, or rhomboedric form and stabilizes [Je 83, Ne 86]. Quantum mechanic

calculations of the cubic lattice energy show that is unfavorable in comparison to the 4H and 6H type (Fig. 1.4).

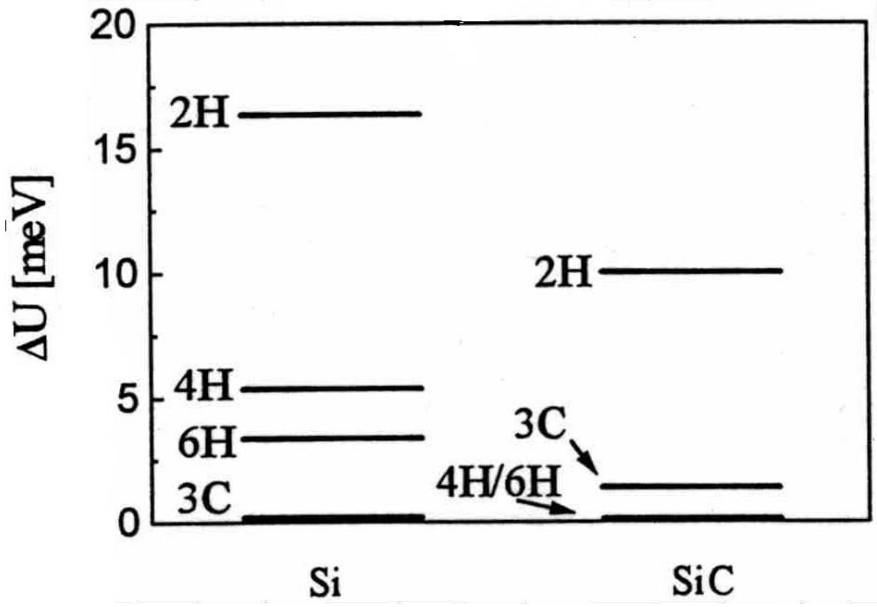

Fig. 1.4: Calculated relative energy (ΔU) per atom for different Si and SiC polytypes [Ch 87b, Ch 88].

Calculations by Heine [He 91] show that during crystal growth the cubic type is always formed as the minimum energy polytype. N-type dopants, e.g. nitrogen, favor 3C-SiC polytype formation, whereas acceptors have no influence. It is possible that, for heteroepitaxy on Si (cubic crystal structure) the formation of the cubic modification, which has a small energy difference from the stable 4H and 6H modifications, can be induced by the substrate.

Many factors e.g. temperature, growth rate, stoichiometry and cleanliness of the sample surface influence the crystal quality. There is no model that can describe SiC formation accurately, so far. Despite the difficulties with polytypes in the crystal growth, there is high potential for SiC. With precise parameter control, the desired polytype can be grown.

1.1.2 Optical and Electronic Properties

Optical Band gap (Eg)

All SiC polytypes have indirect band gaps, which increase continuously with increasing hexagonality: From Eg = 2.390 eV for 3C-SiC to Eg = 3.33 eV for 2H-SiC, see Tab. 1.3. For all polytypes the maximum of the valence band is in the center of the Brillouin zone. The minimum of the conduction band is polytype-dependent at different points of the Brillouin zone (X-point for 3C-SiC and K-point for 2H-SiC).

Polytype	Hexagonality	Band gap (eV) (T=298 K)	dE_g/dT ($eV \cdot K^{-1}$)
3C	0.00	2.390	-5.8×10^{-4}
6H	0.33	3.023	-3.3×10^{-4}
4H	0.50	3.263	
2H	1.00	3.330	

Tab. 1.3: Indirect band gaps and their temperature dependence for important SiC-polytypes [Ch 64, Pa 66, Da 65].

Based on the specific band gap of SiC, which is higher than that of Si devices produced from SiC can withstand temperatures up to 650°C.

Optical absorption and refractive index

The inter-band and defect absorption are responsible for characteristic colors of different SiC-polytypes see Tab. 1.4.

Polytype	3C	4H	6H	15R
Color	Yellow	Green	Green	Yellow

Tab. 1.4: Colors of different SiC-polytypes

For 3C-SiC, a green shift is produced [Pa 69] with growing n-doping (by defect absorption, preferential red absorption). A strong Al doping (p-doping) of 3C-SiC changes the color to dark yellow and dark green [Za 68]. The measured shape of the absorption coefficient is characteristic for the indirect band gap [Ni 75, So 92].

The refractive index of 3C-SiC is wavelength dependent (see Eq. 1.3) according to the following empirical formula [Sc 69]:

$$n(\lambda) = 2.55378 + (34170/(\lambda/\mathrm{nm})^2) \qquad \text{Eq. 1.3}$$

Charge carrier density, mobility and effective mass

The electron concentration n in 3C-SiC and 6H-SiC has been described to be between 8×10^{15} cm^{-3} and 1×10^{19} cm^{-3} [Po 87], [Ha 95]. For 3C-SiC on Si, the electron mobility from Hall measurements is calculated according to the following formula:

$$\mu_H(n) = 4.82\ 10^9\ (cm^2/Vs).(n.cm^3)^{-0.424} \qquad \text{Eq. 1.4}$$

An improvement of the Hall mobility and electron concentration can be achieved through an optimization of deposition process parameters. The electron mobility also varies with the polytype of SiC. The effective electron mass (m_e*) of various polytypes was measured by different groups, see Tab. 1.5.

Polytype	m_e*	m_t*	m_l*	Method	Reference
3C	0.337	0.24	0.667	Zeeman	[De 77]
3C	0.347	0.25	0.67	electron-cyclotron-resonance	[Ko 93]
6H	0.45	0.25	1.5	Faraday-rotation	[El 67]
6H	0.47	0.25	1.7	IR-reflection	[Me 92]

Tab. 1.5: Effective electron mass of 3C-SiC and 6H-SiC polytypes. (m_t* = transversal effective mass, m_l* = longitudinal effective mass, $m_e^* = (m_t^{*2} m_l^*)^{1/3}$.

Breakdown voltage

Compared to Si, SiC has a high breakdown field (10 times larger), which enables the production of electronic devices with smaller dimensions and thus, possibly higher levels of integration and operation at higher voltages.

Saturation velocity v_{sat}

The high saturation velocity ($2{,}5 \cdot 10^7$ cm/s) of SiC allows electronic devices to perform better at high frequencies than Si.

Dielectric constant ε

In addition, the small dielectric constant of SiC in comparison to Si allows it to be used at high frequencies. For 3C-SiC, the value of the dielectric constant is uniform in every crystal direction. For the hexagonal polytype, the ε values differ for directions parallel or perpendicular to the crystal c-axis [Pa 70].

Thermal conductivity σ_T

The high thermal conductivity, approximately 5 W/cm·K for 3C-SiC, is even larger than that of Cu or Al_2O_3. This makes increased integration and miniaturization of devices possible as the heat is dissipated more efficiently.

Radiation resistance

The high resistance to ionizing radiation (SiC is almost 100 times more resistant than Si) opens application possibilities for the use of SiC-crystal sensors, for example in nuclear physics, X-ray lithography and devices which are used in areas of high radiation levels (nuclear power plants, cosmic space, etc.)

Chemical and mechanical properties

SiC is very stable and chemically inert. Until today there is no chemical substance capable of reacting with SiC at room temperature. Reactions occur only in discharges, at high temperatures and/or pressures ($p \geq 105$ bar, $T \geq 3200°C$) [Gm 86]. Consequently, SiC can be applied in aggressive atmospheres and at high temperatures.

The density of SiC obtained by X-ray diffraction varies with polytype. Tab. 1.6 summarizes the lattice constants [Ad 59, So 83, Ta 60] and densities for the most frequent types.

Polytype	3C	2H	4H	6H
Lattice constant a [Å]	4.3596	3.0763	3.0799	3.0808
Lattice constant c [Å]		5.0480	10.083	15.1174
Density[$g.cm^{-3}$]	3.2143	3.2140	3.2163	3.2160

Tab. 1.6: Lattice constant and density of the main SiC polytypes [Ad 59, So 83, Ta 60].

Polycrystalline SiC has been used as abrasive and sharp material for almost 100 years. The Mohs hardness, HM, of SiC is 9.08 [Sc 80], situated between corundum and diamond. The Vickers and Knoop hardnesses are between 2500 - 3500 $kg \cdot mm^{-2}$ [Sh 65], [Su 95] depending on crystal orientation and crystal preparation.

Besides the hardness, SiC have other desirable mechanical properties, e.g. a high elastic modulus (700 GPa; value for Si: 170 GPa) at temperatures below 800 °C. This property can be used for micromechanics and in pressure and gas sensors [Kr 95], [Sh 95].

1.2 SiC-based Electronic Devices

1.2.1 Oxidation

The gate-insulation for transistors as well as surface passivation is produced by thermal oxidation (for ion-implanted SiC) and dry etching. The wet process is carried out in water (saturated by O_2 at (90 - 98) °C), the dry one at 850 - 1250 °C in air at atmospheric pressure. Several research groups have found different oxidation rates of (0001)Si-face SiC for polytypes with different hexagonality, which differs from (0001)C-face where the oxidation rates are polytype independent [La 81, Ch 89a, Zh 90]. The oxidation temperature and SiC crystal type (doping, electron concentration, surface cleaning, defect density) influence oxidation-rates as well as the oxide film quality.

Wet oxidation results in stoichiometrical SiO_2, with a low degree of crystallite in the SiO_2/Si interface, whereas SiO_2 obtained by the dry process shows an elevated crystallite at the interface at high temperature (1200 °C) and below this temperature, has an amorphous character. Today there is no precise model to describe this process. In general, it is difficult to obtain high quality oxide films on p-doped SiC. Nonetheless, there are differences induced by the mechanisms of wet and dry processes. Thermal oxides of high quality on n-type 3C/6H-SiC have been produced. For n-type 3C-SiC, the SiO_2 film shows a breakdown voltage of $8 \cdot 10^6$ $V \cdot cm^{-1}$ (comparable to SiO_2 on Si), a fixed charge density of 10^{11} cm^{-2} by Si/SiC-interface [Au 86]. For SiC MOS-technology, it is however essential to decrease the number of defects.

SiC has a higher breakdown field compared to Si, consequently an insulating material is sought with a breakdown field higher than that of SiO_2 and compatible with temperatures above 300 °C. First tests show that aluminum oxide and silicon nitride can be used for this purpose [Ch 89b].

1.2.2 Doping

Doping can be done either by adding the doping material during the process of crystal growth or by ion implantation. In contrast to Si, SiC has a low diffusion coefficient at temperatures below 1800 °C. Changes in the electronic properties caused by doping atoms are influenced by the lattice symmetry (cubic and hexagonal). Nitrogen doping for 6H-SiC on cubic lattice has ionization energies 0.123 eV and on hexagonal 0.855 eV. In contrast acceptors are not influenced by lattice symmetry. Nitrogen doping on 3C-SiC on cubic lattice has ionization energies between 0.048 - 0.055 eV.

P-doping is difficult to achieve as is the general case for wide band gap materials. SiC acceptors have high ionization energy and become electronically active only at high temperatures. Tab. 1.7 shows typical doping substances used to dope SiC crystal for different growth techniques.

	Lely-process	LPE	CVD
n-doping	N_2, P	N_2	N_2, NH_3, PH_3, PCl_3
p-doping	Al, B, Ga	Al	$AlCl_3$, $Al(CH_3)_3$ $Al(C_2H_5)_3$, B_2H_6, BBr_3

Tab. 1.7: Doping substances for different SiC production methods.

The SiC crystals usually have a nitrogen doping of around 10^{15} cm^{-3} caused by nitrogen impurities included in the process gases. In the CVD process, the doping concentration can be varied linearly with the partial pressure of the doping substance in the gas phase. High doping (10^{20} cm^{-3}) causes the film to become polycrystalline. The concentration of electrons or holes is normally one order of magnitude smaller for n-doping and almost two orders for p-doping [Ki 86], [Da 91]. Possible causes can be:

-High ionization energy of acceptors (Al: 0.24 eV and B: 0.735 eV).

-Compensation through n-doping (Nitrogen).

-Preferential trapping of doping atoms at crystal defects.

-Trapping of doping atoms at electrically inactive interstitial positions.

1.2.3 Ion Implantation

Different elements (N, P, Al, B and Ga) have been tested and implanted with variable energy 30 - 300 keV at ion doses of 10^{14} - 10^{15} cm^{-2} at 25 °C [Da 91]. The implanted depths are between 0.1 - 0.5 µm. Implantation of Al and B is difficult in crystals, being possible only at 1800 °C, and then causing a high defect density. A problem with high temperature processing is the back-diffusion of boron. Nitrogen implantation at 80 K (10^{14} cm^{-2}, 90 – 200 keV) causes many defects in the crystal. The quality improves with Al and N implantation at temperatures between 350 and 750°C through "in-situ annealing" [Ed 88]. The critical doses that cause the films to amorphize are 10^{16} cm^{-2} for nitrogen, 10^{15} cm^{-2} for phosphorus and $3 \cdot 10^{15}$ cm^{-2} for aluminum.

1.2.4 Contacts

A problem of the SiC technology is the practical handling of good ohmic contacts, which stay chemically inert at high temperatures (above 600°C). Testing of different metal/SiC systems shows that small changes in the SiC/metal interface have a great influence on the electronic properties of the system and each polytype responds to the contact metal in a polytype-specific change of electric properties. The operating temperature of SiC devices is not limited by the SiC crystal quality, but by the quality of the contact. An n- or p-doped 3C-SiC crystal (10^{17} cm^{-3}) will have a contact resistance of 10^{-4} $\Omega \cdot cm^2$ [Sh 94], for n/p doped 3C-SiC (10^{19} cm^{-3}) the contact resistance is about 10^{-6} $\Omega \cdot cm^2$ [Mo 94]. Different elements have been tested as contact materials : Ti, W, Ni, Re, Pt, Al and Cr as well as combinations of these including metal/gold (Cr/Au, Ti/Au, Ta/Au and W/Au) and silicides (WSi_2, $TaSi_2$ and $TiSi_2$).

The contact is made by metal evaporation or by sputtering in an Ar atmosphere and finally annealing at temperatures between 500 - 1250 °C. The interface oxidation of the contact is an additional problem. An option is using alloys with W, Re and Pt that have high melting point, as using different metals combined with gold. However, the gold alloys degrade strongly at temperatures above 500°C. With Ta and strong n-doping the contact resistance of 3C-SiC is below 10^{-6} $\Omega \cdot cm^2$ and at 1000°C is still qualitatively good with $4 \cdot 10^{-6}$ $\Omega \cdot cm^2$. For extremely doped 3C-SiC the contact resistance is 10^{-4} $\Omega \cdot cm^2$ at room temperature; for temperatures above 500 °C, the contact is non ohmic [Ch 95a, Pa 94] Parsons describes a TiC contact produced by a CVD process at 1260 °C from $TiCl_4$ and C_2H_4 with a resistance of $5 \cdot 10^{-6}$ $\Omega \cdot cm^2$ on a strongly n-doped 3C-SiC. This contact is thermally processed at a temperature of 1030 °C and is mechanically stable. Another difficulty is to make contacts to p-doped SiC. Al

contacts, which have been tested, have a high Ohmic resistance and in addition at high temperatures Al can diffuse. A contact with 10^{-6} $\Omega \cdot cm^2$ on SiC capable of operating at temperatures higher than 600 °C has not been developed to date despite the great effort made in that area of technological research.

1.2.5 Etching

The production process of electronic devices usually needs an etching step. SiC can be mechanically abrazed by boron carbide or diamond grazes. However there is no liquid able to etch SiC at room temperature. Only KOH, NaOH, Na_2O_2 and KNO_3 solutions at high temperatures (400 - 900°C) or a $Cl_2 + H_2$ atmosphere at temperatures around 1000 °C are able of etching SiC. These processes produce crystal faults (dislocations, delaminations, APB's, DPB's and point defects). Furthermore, these extreme conditions are not compatible with traditional lithographic technologies.

For the production of SiC electronic devices, the requirements are a lower temperature processes, a high selectivity, a high quality of surface etching and a high anisotropy.

These requirements can be met by plasma etching in vacuum, or by electrochemical etching.

1.2.5.1 Plasma Etching

Different fluorine derivative gases were tested in plasma RIE. Tab. 1.8 shows different gases and processes used. The activated atoms produced by plasma dissociation react chemically with C and Si from the SiC crystal, producing SiF_4, CO and CO_2. Consequently, the C and Si atoms are removed from the reactor as gaseous products.

Etch Gas	Crystal	p [mTorr]	P [$W \cdot cm^{-2}$]	Mask	$r_{etching}$ [$nm \cdot min^{-1}$]	Ref.
$CF_4/67\%O_2$	3C-SiC(100)	180-2000	0.2-0.8	Cr	5-40	[Do 85]
CF_4/O_2	3C-SiC(100)	10-60	0.3-1.9	Cr/Al	23	[Pa 86]
$CH_3/90\%O_2$ $CBrF_3/75\%O_2$ $SF_6/35\%O_2$	poly-3C-SiC	20	0.4	Al	42 37 40	[Pa 90]
CF_4/O_2	3C-SiC(100) poly-3C-SiCa-SiC	40	0.5	-	20-40 20-60 20-120	[Pa 91]
$NF_3/82\%O_2$	6H-SiC	1000	-	Al	220	[Lu 93]
NF_3/CHF_3 CF_4/CHF_3 SF_6/CHF_3	3C-SiC(100)	20	0.4	Al	15 8-14 12	[Yi 95]
SF_6	3C-SiC(100)	70-150	0.27-0.93	Al	80-200	[W 95]

Tab. 1.8: Different plasma RIE gases and processes used.

Etchants including SF_6 produce better results than CF_4 because the carbon frequently remains on the surface, blocking further reactions. The addition of oxygen eliminates this problem, however with excess oxygen, SiO_2 is produced and makes the etching process rate slow [Pa 91].

1.2.5.2 Electrochemical Etching

Compared with plasma etching, electrochemical etching has the advantage of being doping selective and leading to high etching rates. Oxides on the SiC surface like SiO_2, SiO, CO and CO_2, are removed by wet etching in HF solution (2-5 %). Etching rates of 1 µm/min without light can be easily reached for SiC. By using a laser source (77 $W \cdot cm^{-2}$, 257 nm), the etching rate is increased to 100 µm/min [Sh 92]. Solutions with high F^- concentrations and lower pH values HF/NHF_4 produce flat surfaces [Ng 92] making electrochemical etching a good method for polishing of SiC.

1.2.6 Devices

There are many applications for SiC, some of them described in the following.

SiC electronic devices can be used in aggressive conditions (temperature, radioactivity, aggressive chemical substances) [Bh 93], [Ba 95]. They perform well at high voltages, high power and high frequencies. Because of this, the SiC material is highly attractive for modern semiconductor industry. Some calculations show that SiC has leakage currents up to 10^{14} times lower than Si. Unlike GaN/AlN, SiC has high thermal conductivity that allows it to be used in high power applications. More specifically, it can be used in radar systems, communication systems, electricity transmissions, high voltage protections, electric car equipment, radioactive environment systems, the sensor industry and the general automotive industry. Additionally, there are many applications of SiC for aggressive environments and high temperature systems [Ar 93, Ka 95, Hu 95].

Palmour et al. [Pa 88] produced an n-channel MOSFET with a maximum operating temperature of 650°C, the highest temperature ever observed for a transistor. Kelner et al. [Ke 89] described a JFET with almost 56 $cm^2(Vs)^{-1}$ mobility and a transconductance of 20 $mS \cdot mm^{-1}$. Theoretical calculations show that electronic devices with optimized channel distances and charge carrier concentration could reach values such as 100 $mS \cdot mm^{-1}$.

For industry, 6H-SiC electronic devices yield better results than 3C-SiC because of the higher material quality. 6H-SiC MESFETs are the only SiC field-effect transistors applied in the microwaves. Several transistors have been produced with a limit frequency range of 5 GHz [Cl 92]. Calculations of Trew et al. [Tr 91] show that SiC-MESFETs can be still feasible with 65 W at 10 GHz.Xie et al. [Xi 95] described NVRAM structures with 6H-SiC based on bipolar transistors, integrated vertically, and memory capacitors with an extrapolated storage time of more than 100 years at room temperature. SiC semiconductor devices operate in a limited way because the SiC/SiO_2 surface contact interface in MOS structures has a high defect density and thus limits the carrier mobility. In addition, the Ohmic and Schottky contacts are also limiting factors. By improving the contact technology, the performance of the SiC devices would increase dramatically.

Micromechanical SiC devices maintain high quality even at high temperatures. Structures on SiC could be applied as pressure sensors or accelerating gas sensors [Kr 95]. Other applications are: Sensors (MOSIC-Technology), gas sensors [Sa 01], pressure sensors [Za 01], nuclear particle detectors [Le 01].

1.3 Production of SiC

SiC occurs as a mineral only in the USA, Angola and Russia [Gm 86]. The small crystal sizes and impurities make this material useless for semiconductor applications. The techniques used to grow SiC are described in the following.

1.3.1 Acheson Process

SiC is produced by the reduction of quartz-sand (SiO_2), pure C in an electric discharge oven at a temperature of almost 2000 °C [Ac 1892].

$SiO_2 + 3C \rightarrow SiC + 2CO$; $\Delta G° = -162\ kJ \cdot mol^{-1}$

$\Delta G°$ = Free reaction enthalpy

The addition of substances such as Al, NaCl results in a porous SiC. Because of the spontaneous nucleation and difficult process control polycrystalline materials (3C-SiC, 4H, 6H, 15R polytype) are produced. The product is used for sandpapers, abrasive pads and SiC ceramics. It is estimated that approximately 500 000 t of SiC are produced by this process every year.

1.3.2 Van-Arkel Process

Pure polycrystalline SiC can be obtained by the Van Arkel process, which is based on thermal decomposition (pyrolysis) of various Si and C compounds from precursors in gaseous form on hot graphite. Tab. 1.9 shows examples of different precursors used in this process.

CH_3SiCl_3	CH_3SiHCl_2	$(CH_3)_2SiCl_2$	$(CH_3)_3SiCl$
$(CH_3)_4Si$	$C_2H_5SiCl_3$	$(C_2H_5)_2SiCl_2$	$SiCl_4/C_6H_6$
$SiCl_4/C_6H_5H_3$	$SiHCl_3/C_6H_6$	$SiHCl_3/C_6H_5CH_3$	$SiHCl_3/CHCl_2$

Tab. 1.9: Gaseous precursors for Van-Arkel SiC process production

H_2 or Ar is used as carrier gases. At 1400-1600 °C and atmospheric pressure, stoichiometric SiC is obtained with deposition rates of 40 $g \cdot h^{-1}$. Small SiC crystallites with excess Si are obtained at lower temperatures. At higher temperatures, the crystallite size increases. For temperatures higher than 1600 °C, excess C is obtained between the SiC particles. Doped polycrystalline 3C-SiC is obtained, when a doping gas (diborane, trimethylaluminium) is added.

1.3.3 Lely Process

Developed by J. A. Lely [Le 55], this process produces single crystal SiC from the polycrystalline material supplied by Acheson or van-Arkel-processes. The crystal growth takes place in an inert gas filled graphite vessel at a temperature of 2600 °C. The main species (SiC_2, Si_2C and Si) diffuse through the porous graphite wall to the center of the oven where

the reaction takes place. First, a small hexagonal nucleus is formed producing then a mix of SiC-single crystals (6H, 4H, 8H and 15R). The process produces n-doping when the gas and/or graphite include N_2. The doping can be increased by increase of the N_2 pressure, p-doping occurs by addition of acceptors (Al and B). The main problem of this process is the spontaneous nucleation in the system at the beginning of the growth where the polytype control is too difficult [Kn 63, Ka 70]. An alternative to the Lely process is the modified Lely process where a better crystal growth control takes place by using a seed crystal of the required polytype [Ta 78]. The temperature gradient of the sublimation is controlled, and as a result, a single crystal is deposited.

Pure polycrystalline SiC obtained from the van-Arkel-process is used as a source material, which the graphite oven with double wall and four compartments is heated through Tantalum resistive or inductive heating. The typical temperature is 2200 - 2400 °C, growth rates ranges from 1 to 10 $mm \cdot h^{-1}$ [Ta 95]. Different research teams showed single crystals grown by this process, see Tab. 1.10.

Polytype	Thickness [mm]	Length [mm]	Reference
4H/6H/15R	8	8	[Ni 83]
4H/6H	14	18	[Ta 81]
6H	20	24	[Zi 83]
6H	33	14	[Na 89]
6H	50	75	[Ho 94]
6H/4H	50	-	[Ts 95]
6H	75	-	[Br 95]
3C	-	-	[Cl 01]
4H	-	-	[Wa 01]

Tab. 1.10: Dimensions of different SiC single crystals, produced by the modified Lely technique.

The main problem of this process are the so-called micropipes produced in the single crystal growth. Nevertheless, the number of micropipes (1990: 118 $MP \cdot cm^{-2}$, 1995: 3.5 $MP \cdot cm^{-2}$) [Ta 94, Ts 95, Ca 01] has continued to be reduced. Doping by the background of N_2 is an additional problem, which makes this method unsuitable for cubic SiC, though this problem is reduced by the use of tantalum ovens [Mo 92], [Ho 95]. Several parameters influence the growth of the crystal polytype (gas flow speed in the reactor chamber, type of crystal, distances of the source of the gas and the sample in the reactor and the temperature gradient). A reproducible 3C-SiC growth process is still to be developed.

Nowadays this is the standard process of growing 4H-SiC and 6H-SiC with 75 mm diameter and micropipe densities as low as 1.1 cm^{-2} used by Cree Research Inc. [Ca 01], with n- and p-doping and priced at US$ 2200 - 2900 each.

1.3.4 Liquid Phase Epitaxy (LPE)

SiC cannot be synthesized by stoichiometric melt crystallization because its peritectic nature produces only non-stoichiometric SiC [Gm 86]. Brander and Sutton deposited SiC on a cold sample in a pure graphite oven [Br 69] at a temperature of 1650 °C.

P/N-junctions in 6H-SiC as well as the first LED [Mü 78], [Ho 82] were produced successfully with this technique. The solidification of the melting material at the end of the process causes stress damage in the resulting SiC-crystal. Suzuki et al. [Su 75] solved the problem by removal of the crystal before the solidification and subsequently produced blue LEDs [Na 89]. Another problem of LPE is the high impurity diffusion at the high temperatures of the process. Dmitriev [Dm 85] developed a new Container-Free Liquid Phase Epitaxy (CFLPE) process where Si is evaporated by a discharge in a magnetic field, typically with a metallic oven in a He atmosphere.

The typical CFLPE characteristics are:

-Melten surface directly in contact with gaseous reagent.

-Electric and magnetic fields produce intensively mixed vapor.

-Vapor temperature is determined by the combination of volume and gas pressure.

-The carbon source used for the crystal growth is SiC crystals from van Arkel-material, which are introduced in the molten Si.

-6H-SiC and 4H-SiC (Lely-crystal) are used as substrates.

-Temperature 1500-1700 °C.

An alternative technique using lower temperatures (1100-1200 °C) and SiC/Ga melts [Dm 92] results in 6H-SiC p-n-junctions, however the growth rates in the range of 0.1 $\mu m \cdot h^{-1}$ are not economic.The first heteropolytype produced through LPE was in 1993 [Dm 93]. An n-type 3C-SiC film with thickness 30 µm on p-type sample 6H-SiC was produced at a temperature of 1150 °C resulting in a p-n red hetero junction LED (λ_{max} = 600 nm).

1.3.5 Molecular Beam Epitaxy (MBE)

A high quality film can be produced by MBE with gaseous precursors at low pressure (10^{-9}mbar) deposited on a hot substrate [Fi 95]. MBE uses gas sources such as Si_2H_6, C_2H_2 and C_2H_4 at deposition pressures of 10^{-5} -10^{-6} mbar. There are alternative MBE techniques available including continuous gas introduction during the growth process [Yo 90], [Ta 94a].

The typical growth rates for both types of MBE are 0.03 - 0.3 $Å \cdot s^{-1}$ at a substrate temperature of 800 - 1000 °C. Generally 3C-SiC (CVD-material) and 6H-SiC (Acheson-material) on Si are used as substrates. The process advantages are the low process temperature and high purity, the disadvantages are low deposition rates and high cost of the MBE apparatus. Another problem is the lattice damage caused by hydrogen and hydrocarbon incorporation into the deposited film and additionally the strongly gas flow dependency of the polytype. Attempts to produce high quality SiC single crystals thicker than 1 µm by this technique have not been successful.

1.3.6 Chemical Vapor Deposition

The CVD process is a viable single crystal production method with satisfactory doping behavior.The general reaction is described below:

$$aA(g) + bB(g) \Leftrightarrow cC(s) + dD(g)$$

The compounds A and B enter in the reactor at a specific temperature where a chemical reaction occurs at the surface of the sample, producing a single crystal deposit C while the sub products (D) form gases and are pumped away.The following stages occur within the CVD process [Sh 87a]:

-Transport of the gaseous material to the hot surface.

-Adsorption or chemisorption of the material at the surface.

-Heterogeneous surface reactions.

-Desorption of the gaseous reaction product(s).

-Product transport at the surface.

There are several types of CVD reactors, e.g. cold wall reactors, hot wall reactors, metal reactors, quartz reactors, atmospheric CVD, low pressure CVD, thermal and plasma CVD with different heating types (radiative, ohmic and inductive).

A typical reactor for thermal deposition of SiC is a water cooled quartz pipe with a graphite susceptor covered by a SiC layer. The sample is positioned on an inductively heated substrate holder where a mixture of gases are used (SiH_4, C_3H_8 and H_2 or other precursors), see Tab. 1.11.

Precursor	Reference	Precursor	Literature	Precursor	Reference
SiH_4/C_3H_8	[Ni 83], [Ni 87], [St 92a], [ko 95], [Zo 95]	$SiHCl_3/C_3H_8/H_2$	[Fu 88]	CH_3SiH_3	[Go 92], [Oh 95], [Kr 95a]
SiH_4/CH_4	[Mü 96]	$SiCl_4/CCl_4$	[Ca 66]	$Si[CH_3)_4$	[He 93], [Re 95]
SiH_4/C_2H_4	[ko 88], [Nu 87]	$SiCl_4/C_3H_8$	[Ma 75]	$Si_2(CH_3)_6$	[No 95], [Ta 92], [Wu 96]
SiH_4/CH_3Cl	[Ik 91]	$SiCl_4/C_6H_{14}$	[Mü 77]	$C_3H_6SiH_2$	[St 93], [Ku 93]
$SiHCl_3/C_6H_{14}$	[To 69]	CH_3SiC_{l3}	[So 88], [Ch 93]	$(CH_3)_2SiC_2$	[Ja 71]

Tab. 1.11: Precursors used for the CVD of SiC.

Although thick single crystals of cubic SiC have not been produced by CVD so far, this method is an alternative, able to produce undoped and doped 3C-SiC. The SiC crystal can be grown homoepitaxially (SiC on the same SiC polytype substrate) or heteroepitaxially (on a different substrate, e.g. TiC and Si). Both types of growth process are described in the following.

1.3.6.1 Homoepitaxy

First attempts of homoepitaxial growth of 6H-SiC on 6H-SiC substrates prepared by the Acheson process were made at relatively high temperatures (1700-1900 °C) [Fu 88, Mü 76, Ni 78]. By improving the substrate quality (modified Lely-process) the growth temperature was reduced. For example, 6H-SiC grown on 6H-SiC Lely samples and 4H-SiC on 4H-SiC Lely samples, the process required substrate temperatures of 1550°C or 1620°C respectively.

The growth rates of this process are 2 $\mu m \cdot h^{-1}$. The n-type doping is done by N_2, p-doping by trimethylaluminium, with concentrations ranging from $1 \cdot 10^{15}$ to $1 \cdot 10^{19}$ cm^{-3} [No 95]. The Hall measurements of n-doped 6H-SiC show an electron mobility of 104 $cm^2 (Vs)^{-1}$. High quality materials are produced at low temperatures compared to 6H-SiC Lely material which has a smaller electron mobility.

The high temperature CVD 6H-SiC epitaxial process provides deposition rates up to 100 $\mu m \cdot h^{-1}$ [Ja 95], which is relatively high compared with LPE and sublimation processes.Cree Research Inc. offers n- and p-doped 4H-SiC and 6H-SiC material grown epitaxially on Lely-substrates priced from US$ 500 to 2900.

Nishino et al. [Ni 95] describe the 3C-SiC homoepitaxy deposition on 3C-SiC Lely-process samples ($SiH_4/C_3H_8/H_2$) at a temperature of 1560 °C, atmospheric pressure with deposition rates of 2.5 $\mu m \cdot h^{-1}$, with nitrogen doping at a level of $5 \cdot 10^{15}$ cm^{-3}. There are also no significant DPB interface film defects by this method. The main problem in homoepitaxy of SiC is the high production cost and lower quality, while the main advantages of homoepitaxy are the appropriate lattice constants and thermal coefficients.

1.3.6.2 Heteroepitaxy

The advantages of using silicon as a substrate in heteroepitaxy of 3C-SiC are price, quality and polytype control. The equipment used in SiC heteroepitaxy is the same as for homoepitaxy [Sy 94].Other substrates have also been investigated (TiC and Al_2O_3) [Pa 85], [Ba 69], but they are expensive or without adequate quality for SiC semiconductor applications. Films of 3C-SiC on 6H-SiC growth at temperature of 1450 °C with deposition rates of 4 $\mu m \cdot h^{-1}$ and thickness up to 12 µm were described by Powell et al. [Po 90]. Compared with 3C-SiC deposition on Si, these samples exhibited fewer interface defects.

The initial experiment with deposition of SiC on Si [Ja 71, Ni 80, Mo 74, Ma 78] illustrated that differences in both the lattice constant (almost 20 %) and the thermal expansion coefficient (almost 8 %) between SiC and Si produced a high concentration of defects at the SiC/Si interface and consequently crystal growth by this process turned out to be problematic. Nishino et al. [Ni 83] solved this problem by growing films with the so called "Buffer layer" technique where the film is deposited at atmospheric pressure with specific gases ($SiH_4/C_3H_8/H_2$) in a quartz reactor with a graphite susceptor, and an inductive heating system. The Fig. 1.5 shows the deposition process. The growth occurs in 3 stages during which the H_2 flow carrier gas remains constant during the whole process.

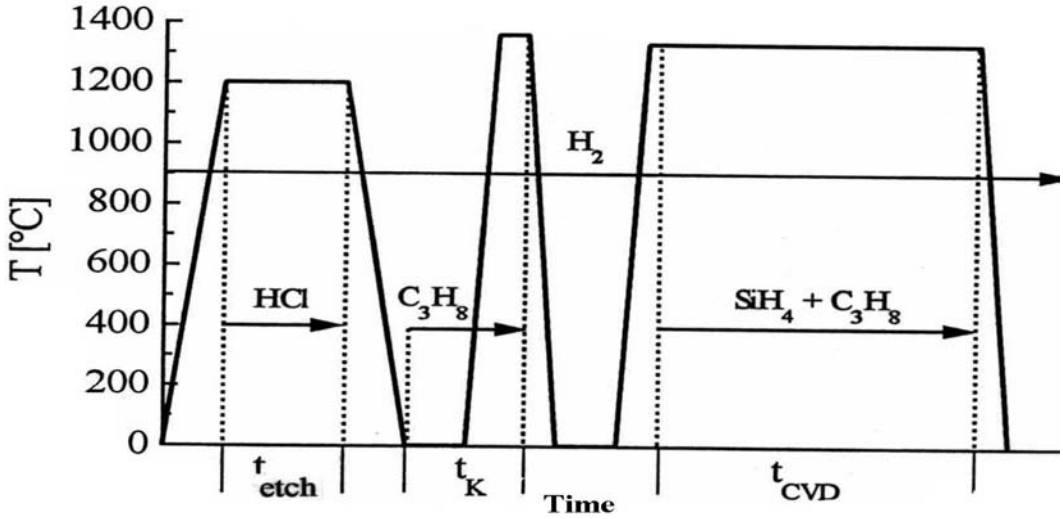

Fig. 1.5: Temperature programs 3C-SiC heteroepitaxy on Si [Ni 83].

Stage 1. Etching. Preparation of the Si-substrate.

The silicon wafer is heated to 1200 °C with a flow of 4 mol% HCl in H_2, then the HCl gas flow is interrupted and the substrate cools down to room temperature.

Stage 2. "Buffer-Layer." This stage produces a thin 3C-SiC crystal only several nm thick [Iw 88]. For this purpose, 0.03 % C_3H_8 in H_2 is introduced into the reactor. The Si substrate is heated from room temperature with a temperature ramp of 10 °C/s up to 1360 °C. After approximately 120 seconds at this temperature the propane gas flow is interrupted and the substrate is cooled down to room temperature.

Stage 3. 3C-SiC crystal growth. The Si-substrate is heated up to 1330 °C and 1 minute later, the gaseous mixture (0.04 mol% SiH_4 and 0.02 mol% C_3H_8 in H_2) is introduced to the reactor. Under these conditions, the 3C-SiC film grows. With a deposition rate of 2.5 $\mu m \cdot h^{-1}$. At the end, the Silane and Propane flows are stopped and the substrate cools down to room temperature. Finally, the H_2 gas flow is stopped.

This process was used by different research groups with some variations for 3C-SiC deposition [Ad 84, Cl 01, Ko 95, No 95, Bo 85, Li 85, Po 87, Sh 87, Ni 87, Ch 90, Ik 91, St 92, St 92a, St 92b, Ta 92, Yu 94, Li 95, Zo 95]. It was also tested with different Si substrates on Si(100)/(111) and different gases. The production of epitaxial films with high quality depends on a number of factors. In particular, the substrate orientation has large influence on the epitaxy process [Sh 86] and it has been shown that for orientations (100) and (111) the best results are achieved. On the other hand, Si (111) substrates frequently show cracks in the film during the cooling process because higher mechanical stresses result for this substrate orientation compared to (100) substrates.

Exhaustive studies show that the deposition rate is connected with the quality of the film, i.e. by using lower deposition rates, the quality is improved. In addition, the proportion of Si and C in the gaseous phase changes the film properties. Many authors use values from 0.4 to 1.0 [Li 85, Po 87, Su 84]. Other factors such as deposition pressure, temperature, carbonization deposition temperature, carbonization duration and gaseous purity influence the 3C-SiC film quality [Li 95, St 92a]. The Buffer-Layer-Process at temperatures higher than 1300 °C results in the formation of several film crystal defects:

-Dislocations and stacking faults at the Si/SiC interface, caused by high mechanical stress due to the different lattice constants and different expansion coefficients (Si: $3.9 \cdot 10^{-6}$ $(°C)^{-1}$, 3C-SiC: $4.9 \cdot 10^{-6}$ $(°C)^{-1}$) between Si and SiC [Nu 87]. The density of these defects decreases progressively with distance from the interface.

-Crystal Twins.

-APB. This defect arises at the Si/SiC interface when a polar SiC film grows on a non polar Si (111) film [Pi 87], where Si and C are occupying different positions [Bo 69]. As a result a wrinkled crystal surface is formed. Using Si (100) substrate [Fu 88] leads to a reduction of this defect [Sh 87].

-Voids in the Si-substrate [Mo 74]. These voids are found directly below SiC films with pyramidal square base formation if Si (100) is used and a triangular base if Si (111) is used [Ca 66, Li 85, Po 87]. The void density depends on the deposition process, approximately 10^5 - 10^7 cm^{-2} voids per cm^2.

New research shows that these voids [Li 95] already begin to grow during the carbonization step. The nucleation through the crystal growth is calculated by the concentration of carbon in the mixture of reactivates gaseous. After the first island formed, the direction of growth is both simultaneously vertical and horizontal. By increasing the nucleation in the beginning of the process via increasing the propane flow, the defect density can be reduced [St 92b].

To produce a high quality SiC/Si heterostructure, the defect density has to be reduced for example by deposition at lower temperatures. Chaudhry and Wright [Ch 90] suggested an alternative CVD process where deposition of 3C-SiC ($SiH_4/C_3H_8/H_2$) occurs at 1150 °C with deposition rates of 1 $\mu m \cdot h^{-1}$. Films of 100 nm were produced by this process and analyzed by TEM and standard X-ray diffraction. Another possibility to decrease the temperature is using "Single Source Precursor" in LPCVD, in general without a carbonization stage. The single molecule precursor contains silicon and carbon at the stoichiometric ratio 1:1. The LPCVD process compared with CVD at atmospheric pressure shows the advantage of producing homogeneous film specially when applied to a large area of deposition [Ti 95].

Furumura et al. [Fu 88] describe 3C-SiC single crystalline deposition on 4 inch off axis Si (111) using $SiHCl_3/C_3H_8/H_2$ with a pressure of 2 mbar and at a temperature of 1000 °C. The resulting deposition rate was 0.6-1.8 $\mu m \cdot h^{-1}$ with a maximum deposited thickness of 400 nm. Golecki et al. [Go 92] describe epitaxial 3C-SiC grown on Si (100) with the CH_3SiCl_3 precursor with deposition rates of 0.1 - 1.0 $\mu m \cdot h^{-1}$ and pressures of 0.13 - 1.30 mbar at 750°C. However, the electronic data for these 3C-SiC films was not reported and the growth of the film has not been reproduced by other groups.

1.3.7 Methyltrichlorosilane (MTS) Deposition

The use of Methyltrichlorosilane to produce SiC has been investigated. The advantage in this case is that MTS is a by product of the silicone industry, relatively cheap, easy to prepare, is also attractive because it has the stoichiometric relationship between Si and C in the molecule.

$$H_2 + CH_3SiCl_3(g) \rightarrow SiC(s) + 3HCl(g)$$

Until six years ago, SiC was grown from MTS on a graphite stem (Van-Arkel-Process) [Po 64, Ca 70] at 1100 °C resulting in polycrystalline 3C-SiC with (111) preferential crystal orientation. By increasing the temperature, a (110) preferential crystal orientation was produced with a typical crystal size of 0.1 µm. Increasing the temperature to 1200 °C increases the seed size up to 1µm. At 1600 °C the seed size obtained was 1500 µm. To avoid deposition of carbon during the film growth it was important to introduce hydrogen as a diluting agent [Ca 70, Ko 75].

The reports of several groups [Mü 78, So 88, Ku 90, Go 94] show that lower temperature deposition or a higher H_2/MTS gas phase ratio results in a rich silicon film formation. On the other hand, high temperature deposition or lower H_2/MTS ratios results in carbon rich film formation. For example, Motojima et al. [Ch 87] used 1100 °C and 1013 mbar to produce a film of 3C-SiC with optimal stoichiometry. Tab. 1.12 summarizes the results of different research groups working with the precursor Methyltrichlorosilane at different parameters.

Reference	Substrate	p [mbar]	T [°C]	H_2/MTS	Deposition rate [Å·s^{-1}]	d [µm]
[Po 64]	graphite	360-886	1400	-	1400	3000
[Ca 70]	graphite	1013	1010-1650	0-6	2800	3000
[Mü 78]	graphite	1013	1400-1600	-	1400	3000
[Ch 87]	graphite	-	1250-1600	50-500	50-500	-
[So 88]	graphite	266-666	1100-1400	50-200	166	30
[Mo 90]	graphite	13-1013	1000-1200	13-70	-	-
[Ku 90]	graphite	50	1200-1500	160	50-150	36
[Go 94]	graphite	2.7-33.3	1380-1470	10-30	33-166	2.5
[Ni 89]	Si (111)	-	1100-1300	-	3.3	0.3
[Ch 93]	Si (100)*	2.4-10.6	1000-1150	10-100	0.2-3	2-5
[Ch 95]	Si (100)*	2.4	1100-1150	100	2	0.15-0.9

Tab. 1.12: Different publications based on the SiC growth process using the Methyltrichlorosilane precursor.

SiC can be doped with diborane and trimethylaluminium. This produces n and p type polycrystals as pure starting material for the sublimation process of SiC. Nishino et al. [Ni 89] describe single crystal deposition of 3C-SiC on Si (111) in a hot wall reactor at 1300 °C where the following stages are used:

-Si substrate etching, 1100 °C, 5 min in HCl.

-Film deposition at temperatures between 1100 - 1300 °C using MTS/H_2, with deposition rates of 3.3 Å·s^{-1}.

Temperatures higher than 1300 °C and lower MTS flow rates resulted in single crystal growth while for temperatures lower a 1300 °C and/or with a high MTS flow rate polycrystalline, 3C-SiC was produced. Deposition of polycrystalline 3C-SiC on Si(100) by LPCVD in a hot wall reactor was described by Chiu et al. [Ch 93]. For growth at 1050 °C resulted a SiC crystal with (111) preferential orientation. However, at temperatures higher than 1050 °C a SiC crystal with (220) preferential orientation was produced [Ch 95]. These authors also describe a 3C-SiC deposition with similar process parameters on a porous Si

(100) substrate at 1000 °C using C_2H_2. To date there are only a few publications [Ku 9, Ue 97] about thick films (~ 5 µm) of 3C-SiC on Si-substrates made with MTS.

Theories for the reaction of the SiC MTS/H2 system [Mü 78, Ca 70] propose that MTS decomposes in the gas phase, but the reactors at the hot substrate surface are not yet fully understood. One theory suggests the following mechanism [Al 93]:

$CH_3SiCl_3 \rightarrow CH_3 + SiCl_3$	(A)
$CH_3SiCl_3 \rightarrow CH_2SiCl_3 + H$	(B)
$CH_3SiCl_3 \rightarrow CH_2SiCl_2 + HCl$	(C)

Experimental results identified the pathway (A) as the main reaction with about 70 % probability and just a 25 % chance of following the reaction (C) pathway [Al 93a]. If hydrogen is replaced by helium the MTS molecule decomposition increases. The methyl radical, the chlorosilane and the hydrogen are important for the decomposition of the MTS gas. The products of MTS decomposition are mainly $SiCl_2$, CH_4, $HSiCl_3$ and HCl. HCl acts to reduce the MTS decomposition rate. Decomposed Si atoms are absorbed and form a strong Si-Cl bond at the surface blocking further SiC depositions [Be 92]. $SiCl_4$ etch the Si-surface causing rough surfaces.

1.3.8 Alternative thin SiC-film Production Technique

There are other alternative techniques for the deposition of thin films at low temperature where the typical process temperature is 1100 °C and the pressure is 10^{-4} mbar [Le 70, Mo 74]. Nishino describes epitaxy of 3C-SiC on Si with Si_2H_6/C_2H_2 by a PECVD process (Plasma Enhanced CVD) at 1150 °C. Polycrystalline or amorphous SiC is frequently deposited using this process [Ya 95, Hi 95].

By using a MBE related technique, MIBE (Molecular and Ion Beam Epitaxy), 3C-SiC is deposited on Si (100) at 800 - 1000 °C, where molecular Si and C+ ions impinge directly on the heated substrate [Mi 84]. This process has deposition rates up to 0.05 $Å \cdot s^{-1}$. Another UHV compatible method for the growth of thin SiC films at low temperatures is the Reactive Magnetron Sputtering technique. The film is sputtered from a Si-target in an Ar/CH_4 plasma onto a hot substrate surface.

Deposition with a total pressure of 4 mbar and a substrate temperature of 850 °C without carbonization of the Si surface produces 3C-SiC epitaxy with deposition rates of 4 $Å \cdot s^{-1}$ and a thickness of up to 10 µm [Wa 93, Wa 94]. Low temperature deposition of 3C-SiC with the RMS technique has potential for development in the future.

2 Preparation of 3C-SiC

2.1 Schematics of the Apparatus for Heteroepitaxy of 3C-SiC (100)

The deposition experiments were carried out using the apparatus shown in. During the course of the experiments the apparatus was continuous improved. The apparatus is shown in its final configuration, see Fig. 2.1.

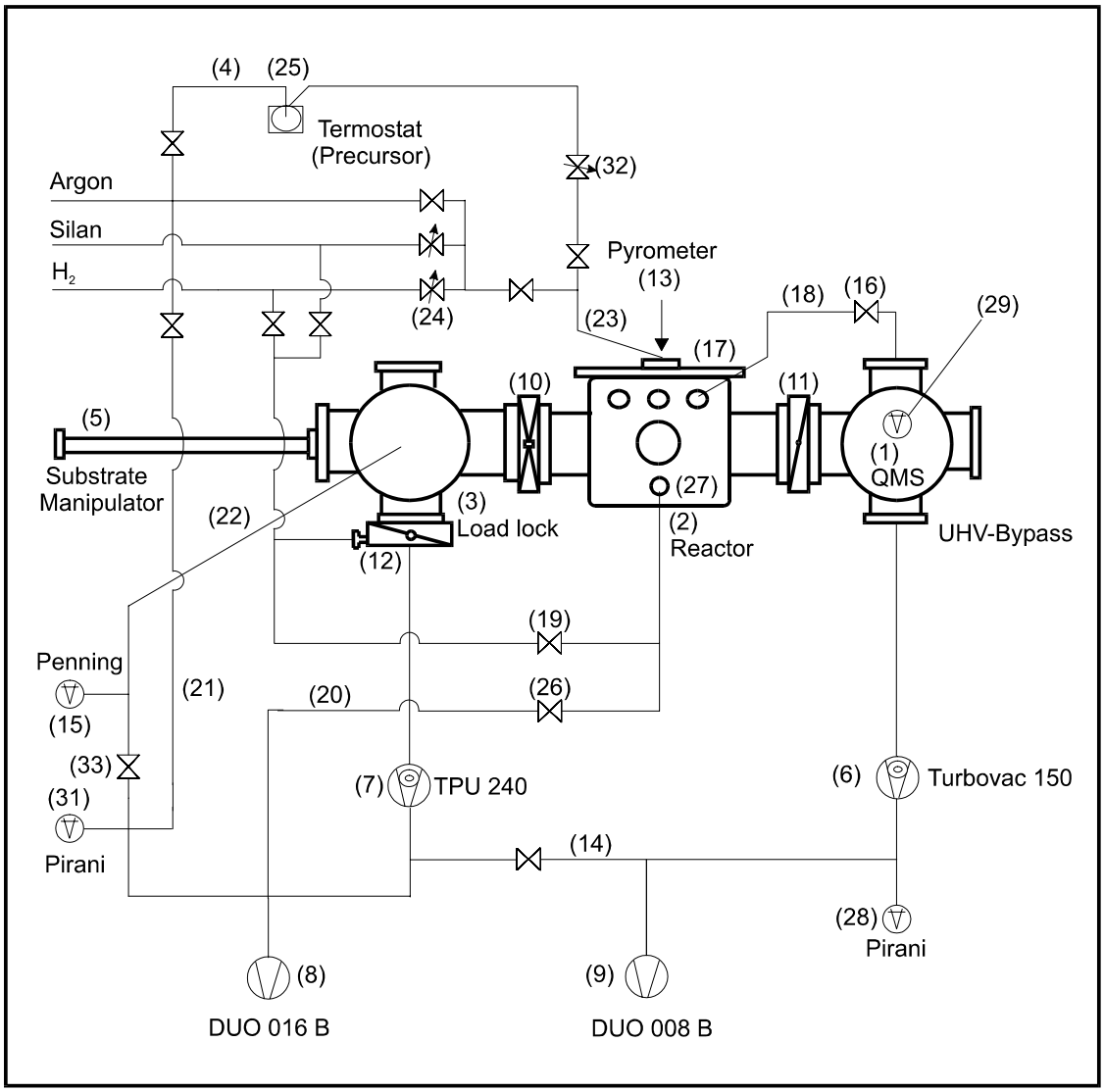

Fig. 2.1: Schematic of the UHV and CVD apparatus used for the deposition of 3C-SiC on Si(100).

The main part of the equipment was the Ultra High Vacuum (UHV) cold-wall reactor constructed in stainless steel (2) and connected on one side to a valve (10) and a load lock (3). For the analysis of the composition of the gas in the reaction chamber the reactor was connected via the second butterfly valve (11) (or alternatively via bypass piping (18) and valve (16)) to the quadrupole mass spectrometer (1) (Balzers, QMG 112A). The mass spectrometer devices include a Quadrupole analyser 125, a cross beam ionic source, a 90° off-axis SEV 217/Faraday plate (DN 63CF) with a range of 0 - 200 amu.

The cross shaped load lock (3) with manipulator (5) is connected via the butterfly valve (12). The pump system includes a turbo-molecular pump (7) (Balzers, TPU 240 with pumping speed 200 $l \cdot s^{-1}$ for N_2) combined with two rotary pumps (8) and (9) (Balzers, DUO 016B with pumping speed 16 $m^3 \cdot h^{-1}$ for N_2 and DUO 008B with pumping speed 8 $m^3 \cdot h^{-1}$ for N_2). To avoid pump contamination and pump reverse diffusion, filters were connected to the inputs of the rotary pumps. The manipulator (5) allows transfer samples from the load lock to the reactor.The load lock was evacuated in the first stage via rotary pump (8) through bypass (22). In the next stage of the process, the system was connected with the turbo pump TPU 240 and rotary pump (9) through bypass (14). After obtaining a pressure of approximately 0.1 mbar, the bypass valve (33) was closed and the load lock was directly pumped through the butterfly valve (12) with the turbo-molecular pump (7). The vacuum was measured with a Penning manometer (15) (Balzers, IKR 020 with a measuring range of $5 \cdot 10^{-3}$ - $5 \cdot 10^{-9}$ mbar) on the UHV side and with a Pirani manometer (31) (Balzers, TPR 010 with measuring range of $8 \cdot 10^{-4}$ - $1 \cdot 10^{3}$ mbar). After approximately 24 hours of heating, the pressure was reduced to $2 \cdot 10^{-8}$ mbar and after 48 hours of cooling down to $6 \cdot 10^{-9}$ mbar. The leak rate in the apparatus was calculated to be $5 \cdot 10^{-8}$ $mbar \cdot l \cdot s^{-1}$.

A pump system consisting of a turbo pump (6) (Leybold, TURBOVAC 150 with pumping speed of 145 $l \cdot s^{-1}$ for N_2) and a rotary pump (9) (Balzers, DUO 008B with pumping speed of 8 $m^3 \cdot h^{-1}$ for N_2) was included to evacuate the quadrupole mass spectrometer (1). The pressure was measured with the Penning manometer (Balzers, IKR 020) (29) and the Pirani manometer (Balzers, TPR 010) (28). The Reactor (2) with a volume of 5.4 l was evacuated via valve (10) through the pump system of the load lock or through valve (11) via the pump system of the MS-chamber. The measuring of ultra high vacuum was carried out using the Penning manometers.

During the deposition, the pressure in the reactor was controlled with a capacitive-meter (27) (Baratron MKS) or with a mechanical manometer (max. 1 bar) (25). Before the deposition, the whole system was heated and vacuum was achieved by use of the turbo and rotary pumps. The load lock was directly pumped to a final pressure of 5 - $6 \cdot 10^{-9}$ mbar. For deposition the valves (11) and (12) were closed, the process gas was injected via valve (19) (Balzers, UHV 016). The turbo molecular pump (7) was connected with the load lock or via valve (26) (Balzers, UHV 016) and the bypass through the rotary pump (8). In both cases, nitrogen gas was used to dilute the exhaust gas and to protect the pumps from corrosion.The gases were injected symmetrically in two opposite parts of the reactor through a steel pipe (23) (length 6 mm, ∅ 1 mm).

Hydrogen 5.0 (99.99%) was used as a carrier gas, methyltrichlorosilanee (MTS) (99.8%) as precursor and argon 5.0 (99.99%) for changing the sample in the load lock. The flow of the hydrogen was controlled by a Flow Controller (24) (Tylan with flow range of 0 - 100 sccm). The precursor was vaporized in a stainless steel bubbler (4) at a constant temperature of 5 °C, which was controlled by a thermostat (25) (Haake D8-GH with a temperature of –25 °C to 150 °C, accuracy ± 0.1 °C). The relatively high vapor pressures of methyltrichlorosilanee were regulated by a stainless steel gas valve (32) (VSE). The substrate temperature was measured with a pyrometer (13) through a glass window (17) on top of the reactor (Land, Cyclops 152A with measuring range of 550 °C to 3000 °C, spectral sensitivity 0.8 - 1.1 µm and measuring area 1.1 mm^2).

2.1.1 Substrate holder and Manipulator System

The substrate (Si (100) wafer p-type or n-type) was heated by resistive heating. This method allowed a variable heating rate of 10 to 20 °C·s^{-1} (600 to 1200 °C·min^{-1}) at temperatures between 600 - 1200 °C. Fig. 2.2 shows the construction of the specific substrate holder.

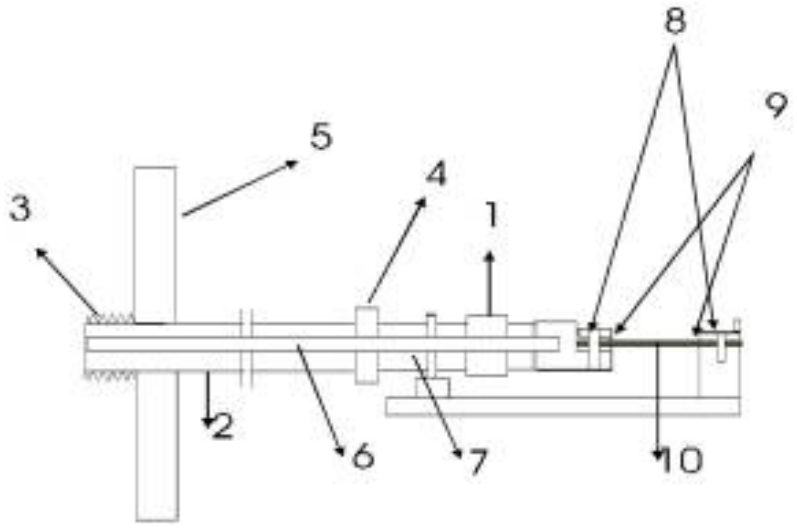

Fig. 2.2: Profile of the substrate holder.

The silicon substrate (10), 30 mm long and 6 mm wide, was fixed at both ends between two Inconnel steel plates (8) and four graphite leaves (9) with a thickness of 0.5 mm, which were used to produce homogeneous heating of the sample. The holder (7) made of copper provided a good heating transport. This assembly generated excellent results. At a high temperature of 1200 °C, the contacts on both sides provide a homogeneous distribution of the heat in the substrate. This system also avoided thermal stresses in the sample through a suitable geometric arrangement. This is illustrated in the Fig. 2.3.

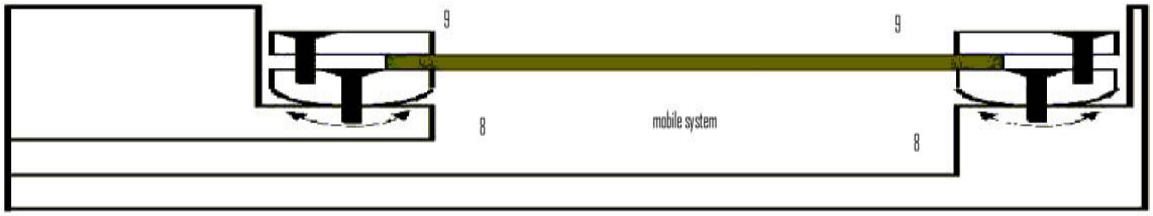

Fig. 2.3: Mobile system sample holder.

The sample was inserted into the reactor with a copper pipe (2) (diameter 6 mm, thickness 1 mm and length 800 mm) and a steel pipe (3) (diameter 16 mm, thickness 1 mm, length 750 mm) Fig. 3.2. The mobility is given by a metallic bellows (1) (VAT, special item) and the pipes electrically isolated to each other with ceramics (6) (Frialit AG). Excessive heating of the substrate holder was avoided through a cooling system regulated by a thermostat. The manipulator and the substrate-holder (see Fig. 2.4) were connected via two lock flanges

DN 16CF (4). The earth cable of the substrate holder was connected with the brass load lock flange (5) that incorporates the electric contact with the load lock.

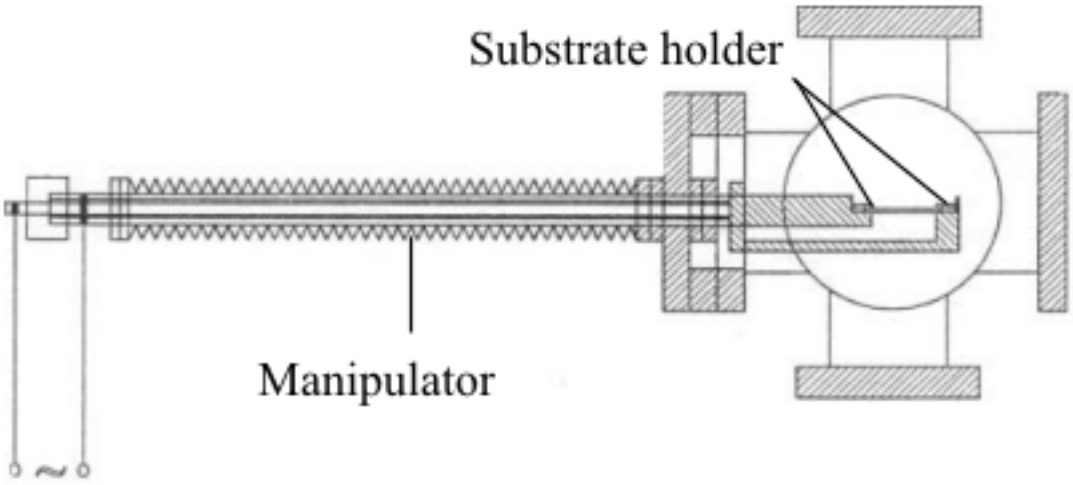

Fig. 2.4: Manipulator and substrate holder positioned for the transfer of the sample in the load lock.

The manipulator's terminal had a cooling system connection and electric-plugs that the metallic bellows was sealed with two viton rings (16 × 2 mm) at the end.

2.1.2 Substrate Temperature Adjustment

To produce high quality films it was necessary to have highly accurate control of the pressure, flow rates, temperature ramping, deposition temperature and the initiation of deposition. Fig. 2.5 below shows a schematic of the electrical system for substrate heating.

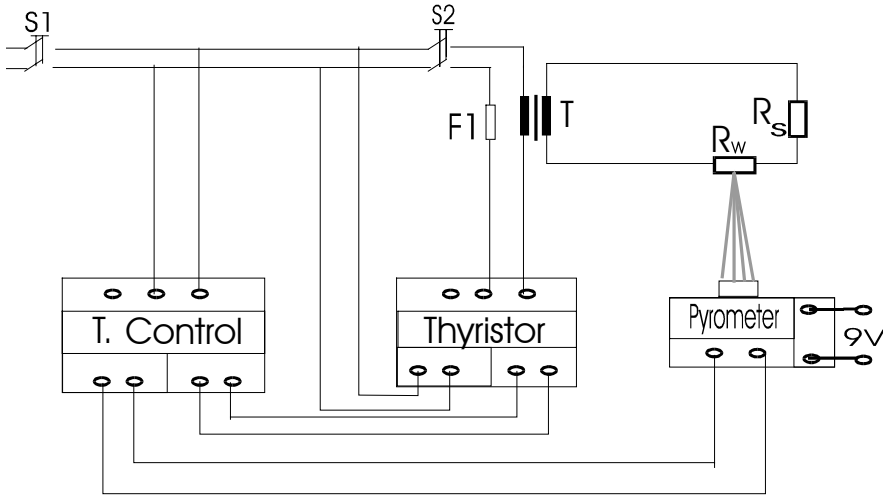

Fig. 2.5: Schematic of substrate heating system. T: transformer (230 V / 60 V, 40 A and 50 Hz), R_s: protective resistance (1.8 Ω), R_w: silicon substrate resistance, F1: Fuse, S1: regulator switch and S2: thyristor switch.

A transformer (230 V/60 V and 40 A) provided the alternating current to the Silicon substrate, which has a constant series resistance R_s (Krawri, 1.8 Ω and 1000 W). Si as a semiconductor shows a negative resistance characteristic as a function of temperature,

$$\rho \propto \exp(E_g/2kT), \qquad \text{Eq. 2.1}$$

ρ: specific resistance (Ω), n: carrier density (cm^{-3}), E_g: energy gap (eV), k: Boltzmann constant and T: temperature (Kelvin). Thus, a constant load resistor is necessary to avoid thermal runaway.

Temperature measurements were achieved using a pyrometer with an output signal of 1m V.°C^{-1} over the temperature range between (550 – 3000) °C. This signal was supplied to a regulator (Eurotherm, 902P). This type of heating system had the advantage of being able to work over a large temperature range of 550 - 1350 °C and with a high temperature ramp of 30 °C·s^{-1}.

2.2 Methyltrichlorosilane (MTS) Precursor

Methyltrichlorosilanee is produced by several companies, for example Merck, Aldrich, Epichem etc. In these experiments, MTS from Epichem was used (Ep 94). This product came generally with a relative high percentage of impurities, usually 2 – 3%, thus the MTS was distilled several times, then cooled and directly introduced into the evacuated stainless steel bubbler. The bubbler with the precursor was installed in a thermostat at a constant temperature of 5 °C.

2.3 Process Sequence

The substrate used was a Si(100) wafer produced by Wacker Siltronic with the Czochralski method and was characterized by the following parameters: thickness 0.68 mm, diameter 14.64 cm, specific resistance 0.01 - 0.03 Ω·cm, n/p doping with one face polished. The substrate was cleaned using an RCA procedure (Ke 70). To remove any organic impurities on the substrate surface, it was first immersed in RCA1 solution (H_2O/H_2O_2 (30 %)/NH_3 (25 %) 6.19:1:1.04) for 20 min with ultrasound vibration at 80 °C. After that, the Si-wafer was rinsed with deionized water (Milli-Q Plus with a specific resistance of 18.2 Ω·cm). Finally, the inorganic impurities on the Si-substrate were removed by immersion in a solution of RCA2 (H_2O/H_2O_2 (30 %)/HCl (25 %) 6:1:1.15) for 20 min with ultrasound vibration at 80°C. The Si-substrate was then rinsed again with deionized water and dried in an ultra centrifuge. The RCA cleaning process resulted in a thin SiO_2 film on the sample surface. Subsequently the sample was weighed with an ultra micro balance (Sartorius XL, precision 10^{-7} g) and mounted on to the substrate holder in the load lock. After that, the load lock was pumped and baked out over night at a temperature between 150 - 200 °C. After 16 hours the UHV-slide valve (10) was opened and the sample was transferred from the load lock to the reactor with the manipulator.

The oxidized Si surface substrate was removed with heating in pure H_2 at a temperature of 1200 °C. At the end of the growth, the valve of the bubbler was closed and the water cooling was interrupted. Then the wafer was cooled down to room temperature and transferred back to the load lock. After that, the gas was evacuated through the load lock by turbo pump TPU 240

with Nitrogen as solvent gas for 2 hours to approximately $2 \cdot 10^{-7}$ mbar. The next stage was to close the UHV-slide valve and to dismount the substrate in the load lock under Argon atmosphere. During this time, the turbo molecular pump evacuated the reactor through the MS-chamber. Finally, the sample was weighed again. From this result, the thickness and deposition rate of the film were calculated.

The following deposition parameters were used:

Substrate temperature (1200 - 1250 °C).

At temperatures below 1200 °C, a slow surface reaction was observed, with the slow surface diffusion resulting in isolated islands of polycrystalline SiC films, also illustrated in the literature [Ch 93, Ch 95]. At temperatures higher than 1250 °C the surface of the Si substrate was etched by chlorine radicals in the gas phase, producing rough surfaces and consequently formation of a polycrystalline 3C-SiC film.

Temperature ramp (dT/dt = 600 - 1200 °C·min^{-1}).

This parameter influences the complex interaction between MTS kinetics, the 3C-SiC nucleation and the Si substrate evaporation. This mechanism was investigated (Ho 98) with LEED (low energy electron diffraction) and AES (Auger electron spectroscopy).

Pressure at deposition (5.25 - 10.5 mbar).

At pressures below 5.25 mbar, many holes with diameters larger than 1 µm where observed in the Silicon substrate. The hole size decreases with an increase of the pressure. At pressures between 5.25 and 10 mbar, no holes appeared in the Si substrate. The nucleation density at the beginning of the growth was smaller for pressures below 5.25 mbar. At these pressures more of the Si substrate area was left uncovered and SiC grow with different orientations, i.e. polycrystalline 3C-SiC. With an increase of the total pressure, the nucleation density also increased. The initial 3C-SiC layer protects the silicon surface also at high temperatures and consequently single crystalline 3C-SiC is formed [Li 95]. For the deposition of 3C-SiC single crystalline films with a very high quality, a precise control of the deposition pressure is necessary.

High quality films of 3C-SiC were grown using the following conditions:

Total pressure	5.25 mbar
Relative partial pressure $p(H_2)/p(MTS)$	(5/0.25) = 20
Substrate temperature	1200 °C
Temperature ramp (dT/dt)	600 °C.min^{-1}

Under these conditions, films different of thickness between 1 and 100 µm were grown with a 2.8 Å·s^{-1} deposition rate.

3 Characterization of 3C-SiC Epitaxial Films

Various analytical techniques used to characterize the SiC films. The characterization techniques and the corresponding results are described in this chapter.

3.1 X-ray Diffraction

X ray diffraction is frequently used to analyze the structure of solids. This method supplies information about crystallographic and preferential orientations, crystal sizes, mechanical stresses, crystal defects, crystal types and crystal aggregations. According to the Bragg relation, Eq. 3.1, a monochromatized X-ray beam is partially reflected on the sample (lattice plane), where the interference of the reflected beam can be constructive in a specific direction.

$$2d \cdot \sin\Theta = n \cdot \lambda \qquad \text{Eq. 3.1}$$

with:

d= Distance between inter-lattice-plain [Å]

Θ= Bragg reflection angle

λ= X-rays wavelength [Å]

n= reflection order

These measurements were performed using the symmetrical Bragg-Brentano-mode (Θ-2Θ-mode) and rocking curve, see Fig. 3.1. The sample was rotated, so that the angle between the sample and the X ray beam, Θ, and the angle between the beam and the detector, 2Θ, resulted in an interference maximum. The Bragg diffraction patterns are determined by the lattice planes parallel to the film surface. Accurate mounting of the sample was necessary for an exact measurement.

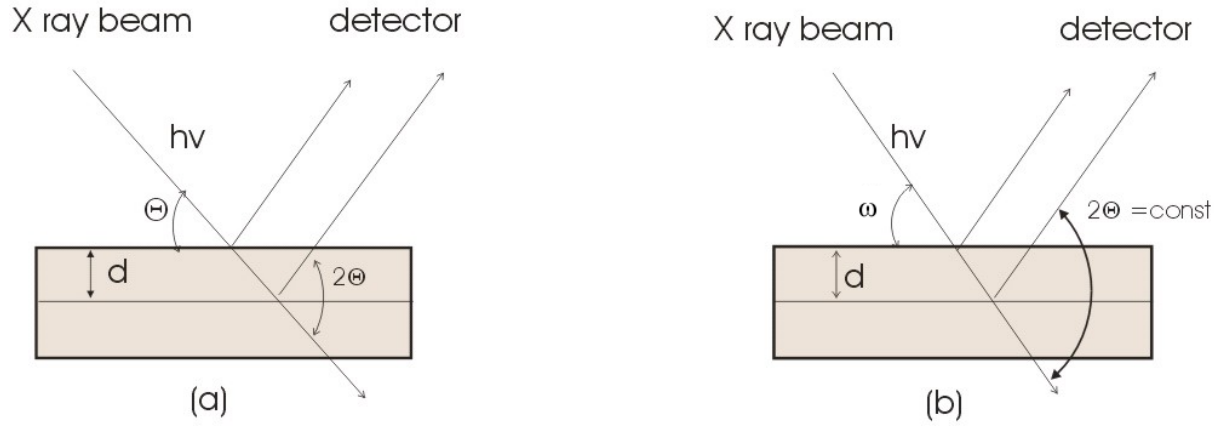

Fig. 3.1: Schematics of X-ray diffraction: (a) symmetric Bragg-Brentano-mode and (b) rocking curve.

The X-Ray diffraction (XRD) patterns were measured with a Siemens Cristalloflex D 5000 diffractometer with a secondary monochromator in Bragg-Brentano geometry. The X ray beam was focused with variable slits before and after the diffraction on the sample. The primary beam was collimated through a 0.05 mm slit. The slits in front of the detector were set as follows: 1 mm spread beam slit, 0.6 mm secondary monochromator slit, 0.6 mm subsequent secondary monochromator slit and 0.1 mm detecting slit. The collimated beam was monochromated on a graphite crystal and detected with a scintillator.

The diffractometer was computer controlled and the data were recorded with the software Diffract ATTN version 2.0.

Fig. 3.2 shows the FWHM values of the 3C-SiC (200) and 3C-SiC (400) reflexes measured in Bragg-Brentano-mode, as a function of film thickness.

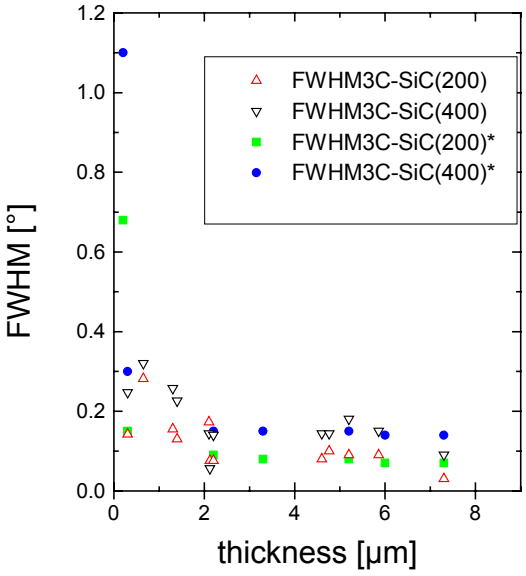

Fig. 3.2: FWHM values of the 3C-SiC (200) and 3C-SiC (400) reflexes compared with literature(*) values [Ku 96] as a function of the thickness of films.

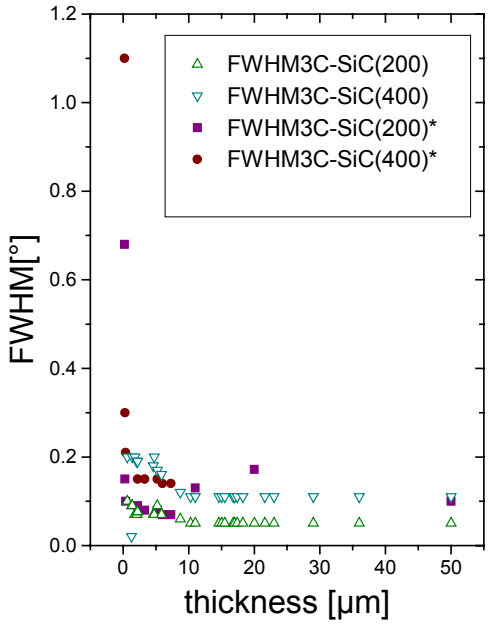

Fig. 3.3: FWHM 3C-SiC (200) and 3C-SiC (400) compared with the literature(*) [Fe 95], measured in Bragg-Brentano-mode as a function of the thickness of films.

Close to the Si/SiC interface, the high FWHM of the 3C-SiC peaks is due to a higher defect concentration in the crystal lattice, caused by the 20 % difference between the lattice constants of Si and 3C-SiC. In the bulk, with increasing distance from the interface, the defect density decreases as indicated by a small FWHM. Fig. 3.3 shows the FWHM of 3C-SiC (200) and 3C-SiC (400) of a series of layers with a thickness between 0.3 µm and 50 µm.

The observed increase of the crystal quality with thickness of the 3C-SiC film, agrees with the literature [Ku 96, Ho 98, Fe 95]. Compared to 3C-SiC films grown via buffer layer technique (1350 °C, with SiH_4 and C_3H_8) the MTS technique shows smaller FWHM values, indicating a faster relaxation of lattice and a higher quality of these films. In the diffractogram of Fig. 3.4, the (200) and (400) reflections of 3C-SiC are shown besides the (200) reflections of the Si substrate. No other peaks were found indicating the absence of other phases of SiC.

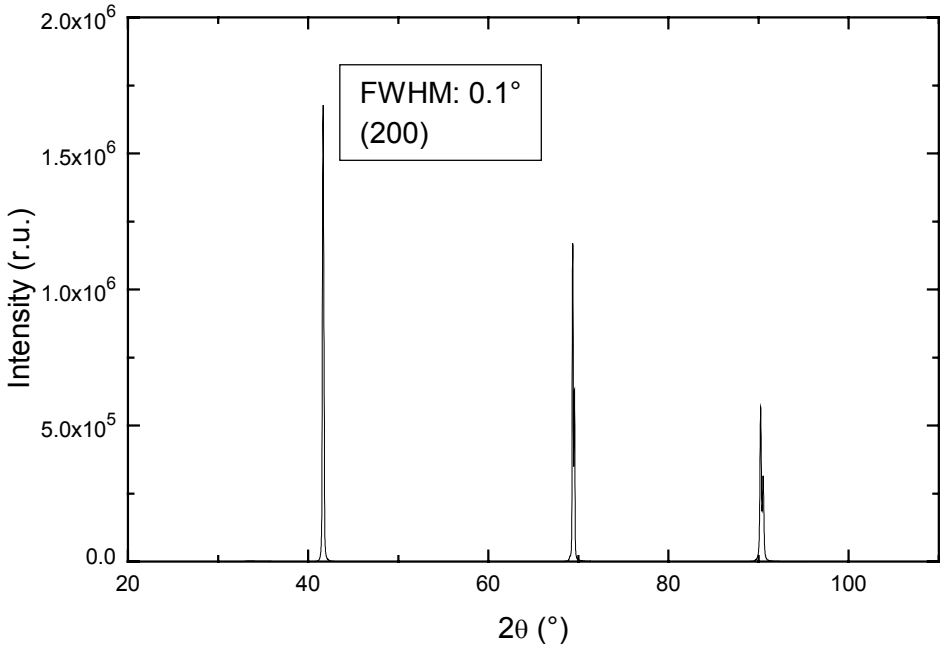

Fig. 3.4: X-ray diffraction of a 6.2 µm 3C-SiC film measured with a conventional Siemens 5000 diffractometer in Bragg Brentano mode.

For thick 3C-SiC films, the FWHM values converge to the instrumental resolution of ± 0.05°. Therefore, an additional analysis of the film quality was obtained with a High Resolution X-Ray Diffractometer (HRXRD). The Triple axes Philips X'pert MRD diffractometer had an accuracy of (10^{-5} -10^{-6})° which is two orders better than the normal diffractometer. Fig. 3.5 shows high resolution X-ray diffractograms for a detailed investigation of the crystal quality.

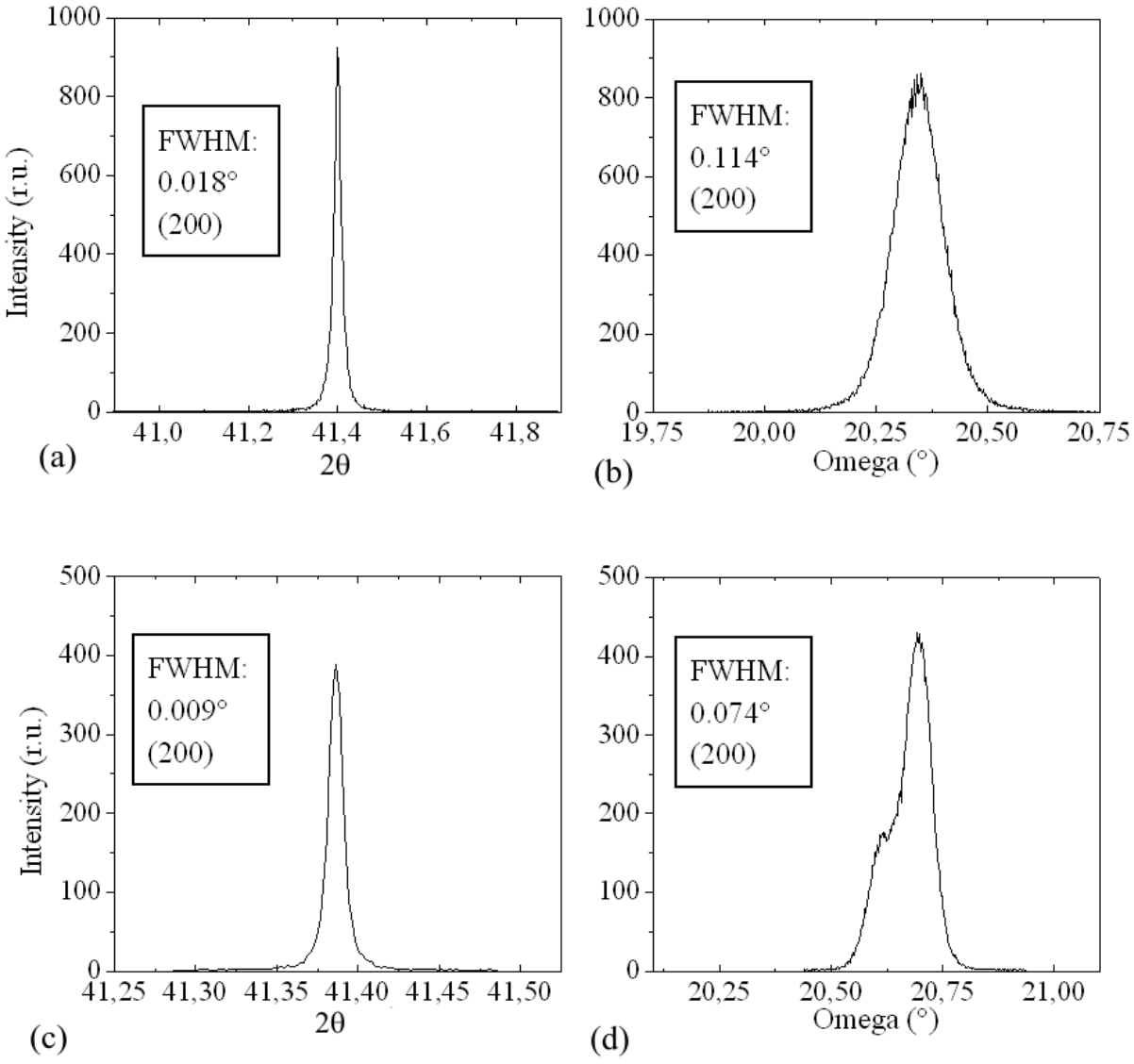

Fig. 3.5: Results of measurements with High Resolution X-ray Diffraction. (a) 6.2 µm, Bragg Brentano mode, (b) 6.2 µm, Rocking Curve, (c) 50 µm, in Bragg Brentano mode, (d) 50 µm, Rocking Curve.

In the high resolution X-Ray diffraction of Fig. 3.5 it is clear to see the improvement of the structural quality of the 3C-SiC by comparing a 6.2 µm to a 50 µm thick film. The rocking curve peak shows for the 8 times thicker 50 µm film a FWHM of 0.074°.

Comparing the rocking curve of the 6.2 µm thick film on Fig. 3.5(b) and the 8 times thicker film on Fig. 3.5(d) one can conclude that the structural quality was improved in the thicker film, but the thinner film is already far from the very defective interface region of Si to SiC.

3.2 Raman Spectroscopy

Raman spectroscopy is frequently used as an analytical method for the vibrational properties of the crystal lattice. The larger part of a laser beam incident on the crystal results in an elastic reflection (Rayleigh-beam). After the interaction with the phonons of the lattice, a small part of the laser beam is reflected inelastically (Raman emission). Two different processes can occur:

A) Stokes process: incident photon produces a crystal phonon.

$$\hbar\omega_s = \hbar\omega_i - \hbar\omega_0$$

$$\hbar\vec{k}_s = \hbar\vec{k}_i - \hbar\vec{k}_0$$

ω_s, $\vec{k}_s$: Frequency, wave vector of scattered photon (Stokes)

ω_i, $\vec{k}_i$: Frequency, wave vector of incident photon

ω_o, $\vec{k}_0$: Frequency, vectorial phonons wave

As a result of this process, the scattered photon will be shifted to lower frequencies.

b) Antistokes process: Photon absorbs a phonon.

$$\hbar\omega_{As} = \hbar\omega_i + \hbar\omega_0$$

$$\hbar\vec{k}_{AS} = \hbar\vec{k}_i + \hbar\vec{k}_0$$

ω_{AS}, $\vec{k}_{AS}$: Frequency, wave vector of scattered photon (Anti-Stokes)

The scattered light is shifted to higher frequencies by this process.

At room temperature, the Stokes-process has higher probability than the Antistokes process. Therefore, only the Stokes process was measured by Raman spectroscopy.

The intensity of the emitted light is described by Eq. 3.2:

$$\mathbf{I_s} \propto \left|e_I \cdot R \cdot e_s\right|^2 \qquad \text{Eq. 3.2}$$

e_I: Polarization of incident beam

e_s: Polarization of scattered beam

R: Raman tensor

The second order Raman Tensor R is symmetrical for nonmagnetic materials (such as semiconductors). Tab. 3.1 shows selection rules for Raman scattering by a crystal lattice of zinkblende crystal type (GaAs/3C-SiC).

Scattering geometry	Transverse optical phonon	Longitudinal optical phonon
x(y,y)(-x); x(z,z)(-x)	0	0
x(y,x)(-x); x(z,y)(-x)	0	$\|d_{LO}\|^2$
x(y',z')(-x); x(z',y')(-x)	0	0
x(y',y')(-x); x(z',z')(-x)	0	$\|d_{LO}\|^2$
y'(x,x)y'(-y')	0	0
y'(z',x)(-y')	$\|d_{TO}\|^2$	0
y'(z',z')(-y')	$\|d_{TO}\|^2$	0
x"(z", z")(-x")	$(2/3)\|d_{TO}\|^2$	$(1/3)\|d_{LO}\|^2$
x"(z", y")(-x")	$(2/3)\|d_{TO}\|^2$	0

Tab. 3.1: Raman emission geometry for crystal lattice of Zinc-blend-type(3C-SiC); d_{TO}, d_{LO} describe the non-vanishing Raman tensor element for TO and LO phonons. The different lattice directions are described as: x:(100), y:(010), z:(001), y':(011), z':(0-11),x": (111), y": (1-10), z": (11-2) [Da 66].

Raman measurements were performed in the following geometry:

(1) for $\vec{k}_I, \vec{k}_S$ //(100) only LO-mode

(2) for $\vec{k}_I, \vec{k}_S$ //(011) only TO-mode

3.2.1 Micro Raman Apparatus

The configuration of the Raman apparatus included an argon laser (Omnichrome, model 532, 20 mW, wavelength = 5145 Å), an optical microscope (Olympus, model BHSM, 3 different magnification (100×, 200× and 500×) and a Raman image detecting system (Renishaw, model 9-RIMS1).

The Tab. 3.2 shows the characteristics of the microscope at which the experiments occurred.

Objective lens	Diameter of measuring area [µm]	Angle [°]
10 X	30	17
20 X	15	27
50 X	5	53

Tab. 3.2: Microscope characteristics

The measurements occured in the backscattering geometry. The resolution of the measurements was limited by the pixel size of the CCD camera (-70 °C, 580 × 380 pixel (19 µm) with 16 dynamic bit) and corresponds to 1.6 cm^{-1} at 900 cm^{-1}. Via the use of ethalons, the resolution increased up to 0.2 cm^{-1}. The system advantages include the short measurement time (approximately 30 seconds for each spectrum) and the simple handling. The Fig. 3.6 shows a schematic view of the Raman apparatus.

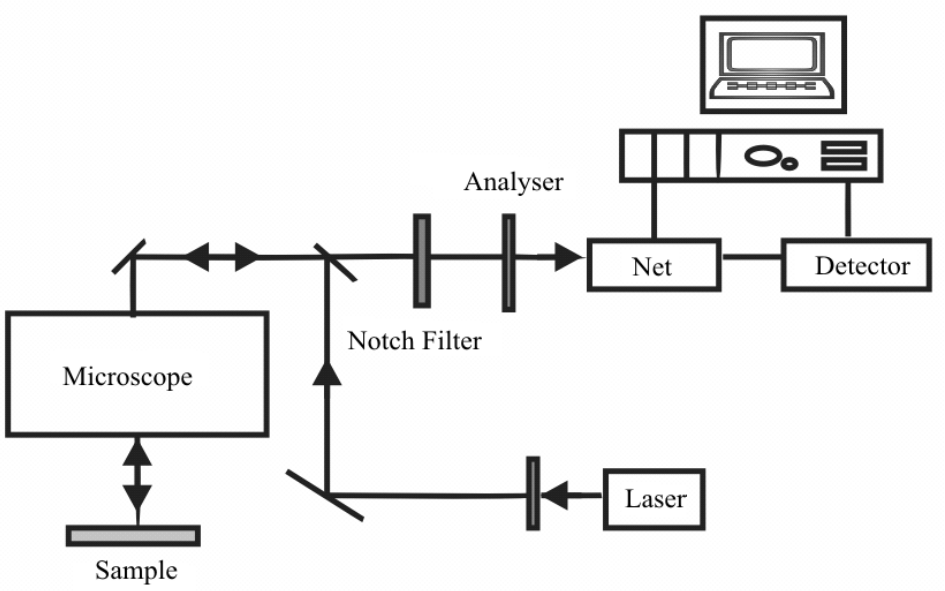

Fig. 3.6: Outline of the micro Raman apparatus indicating the path of the laser beam.

The majority of the measurements were executed with a polarized beam source using a standard configuration. To determine the symmetry of the Raman tensor, measurements were performed. A polarizer between the emitted beam and the detector was used as an analyzer.

3.2.2 3C-SiC Raman Measurement

Raman measurements are frequently applied as an analytic method to characterize SiC thin films. From the position, height and FWHM of the peak in the Raman spectra information about crystal, structure, strain and lattice defects can be deduced. The 3C-SiC polytype shows two characteristic Raman lines, see Tab. 3.3:

Transverse optical (TO) mode at 796.2 cm^{-1}

Longitudinal optical (LO) mode at 972.7 cm^{-1}

Polytype	Modes				Ref.
	TO(2) [cm^{-1}]	TO(1) [cm^{-1}]	LO(2) [cm^{-1}]	LO(1) [cm^{-1}]	
3C-SiC	-	796.0 796.2	- -	972.0 972.7	[Fe 68] [Ol 82]
6H-SiC	788	797.0 796.0	964 967	970.0	[Fe 68] [Ok 87]

Tab. 3.3: TO and LO Raman modes of the 3C-SiC and 6H-SiC polytypes.

The differences between the 3C polytype and other SiC polytypes can be seen by three characteristic Raman peaks:

1. Transverse Acoustic phonons (TA): The α-polytypes of SiC show several peaks in the ranges (140 - 150 cm^{-1}) and (240 - 270 cm^{-1}) while the β-polytype of SiC does not show peaks in these ranges.

2. Transverse Optical phonons (TO): The α-polytypes of SiC show several peaks (760 - 800 cm^{-1}) while the β-polytype of SiC shows only one peak at 796.2 cm^{-1}.

3. Longitudinal Optical phonons (LO): The α-polytypes of SiC show peaks the range 965 - 975 cm^{-1}, for example, the 6H-SiC shows a peak at 967 cm^{-1}. The β-polytype shows a peak at 972.7 cm^{-1}[Ok 87].

For standard geometry with $\vec{k}_I$, $\vec{k}_S$ //(100), only the 3C-SiC LO-mode should be observed (see Tab. 3.1). The LO mode is shifted to smaller wavenumbers by 2 cm^{-1}, compared to bulk material [Fe 88, Fe 95]. This shift is caused by the biaxial stress of SiC film grown on Si, due to the different lattice constants and thermal expansion coefficients. Measurements of optical phonons in the 3C-SiC Lely bulk material [Ol 82, Ol 82a] have also shown the presence of stress [Fe 88a] in the produced film. Raman measurements of the polycrystalline SiC film should show both, the TO and the LO mode [Fe 95].

The absorption coefficient α of SiC is 25 cm^{-1} measured at 514,5 nm at room temperature. The penetration of this laser line in SiC is about 400 μm. Our experiments showed that a sample of at least 2 μm is needed for an accurate Raman spectra. Besides the TO and LO modes of 3C-SiC, there are typically two peaks of the Si substrate that can be seen on the spectra (at 969 – 1000 cm^{-1}). The forbidden TO mode may be present due to imperfect geometry in the backscattering measuring mode. Using a magnification lens of 50x the solid angle in backscattering geometry is bigger in comparison to the solid angle of a 10x magnification lens. Consequently, for a flat monocristalline SiC film, the unexpected TO mode disappears by measuring with a 10x magnification lens.

The forbidden TO-mode can also be observed due to the following reasons:

1. The intensity of the TO-mode of a polycrystalline crystal overlaps the LO-mode.

2. A sample with a rough surface showed a smaller I_{LO}/I_{TO} mode ratio compared to a flat sample. This is caused by a strong scattering on the surface preventing a perfect back scattering geometry.

3. Single crystals with high defect density also showed smaller I_{LO}/I_{TO}.

A criterion for the film quality is the ratio between the allowed (LO) and forbidden (TO) mode, I_{LO}/I_{TO}.

The Fig. 3.7 is possible to see the Raman scattered geometry for significant measurements whereas the position of the sample determines the crystal lattice orientation.

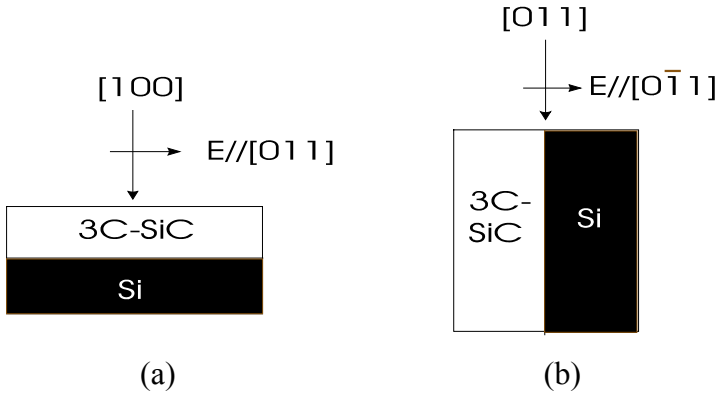

Fig. 3.7: Main Raman scattering geometries with ((a): x(y',y')(-x); (b): y'(z', z')(-y')

The 3C-SiC located far from the Si/SiC interface had a high ratio indicating a higher quality of the 3C-SiC crystal, see Fig. 3.8.

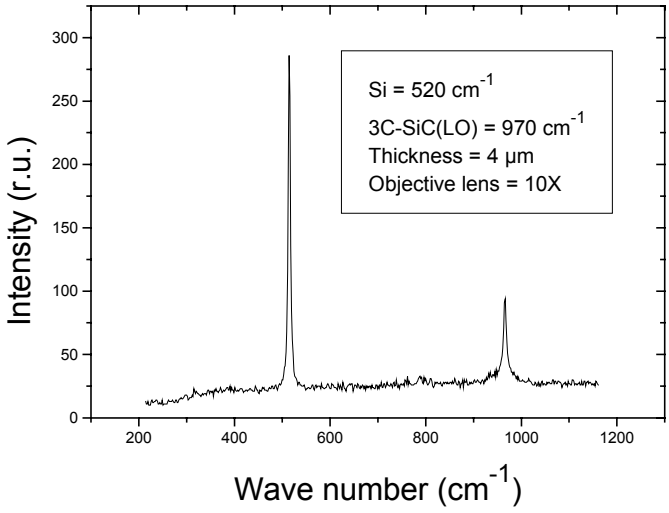

Fig. 3.8: Raman spectrum of 4.0 µm thick 3C-SiC film on Si(100), measured with a scattering geometry of x (y', y')–x and I_{LO}/I_{TO}=12.61.

The Si/SiC surface interface presents small values of 1/n according to a higher concentration of crystal defects (see Fig. 3.9).

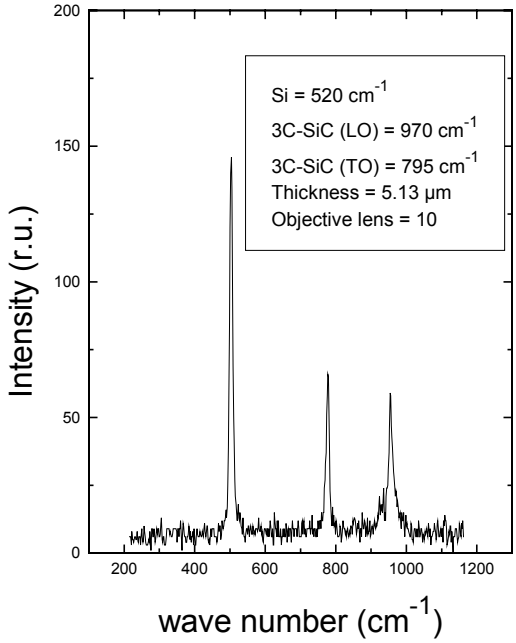

Fig. 3.9: Raman spectrum of 5.2 µm thick 3C-SiC polycrystalline on Si (100), measured with a scattering geometry x (y', y')-x and I_{LO}/I_{TO} = 0.80.

The correlation between thickness, FWHM and the crystal perfection (I_{LO}/I_{TO}) is shown in Fig. 3.10. With increasing film thickness, the crystal quality improves considerably.

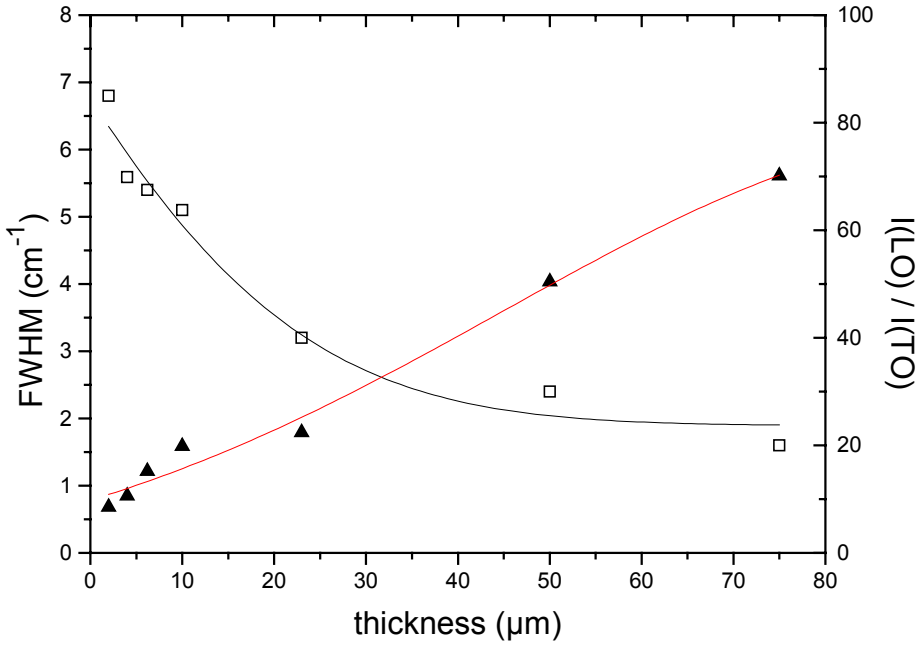

Fig. 3.10: FWHM of the 3C-SiC LO mode and mode ratio I_{LO}/I_{TO} as a function of thickness (10 X magnification, $\vec{k}_I$, $\vec{k}_S$ // 100), deposition parameters: p_{tot}= 5.25 mbar, p(H2)/p(MTS)= 20, T_{dep}= 1200 °C, dT/dt= 600 °C·min^{-1}, r_{dep}= 2.8 Å·s^{-1}.

3.3 XPS

Information about the Si and C stoichiometry of the 3C-SiC film was obtained with X-ray photoelectron spectroscopy (XPS). The XPS spectra of the sample surfaces were measured with a Leybold-Heraeus LHS-10 spectrometer with a hemispherical electron energy analyzer EA-10. An Al anode was used to produce a non-monochromatized X-ray beam. The angle between sample surface and analyzer entrance was 90°. Fig. 3.11 illustrates overview spectra (0-1000 eV binding energy), recorded before and after cleaning by Ar^+ ion sputtering (3 keV, 15 min).

The composition of the SiC film was subsequently calculated by the normal sensitivity factor method used for XPS. The calculation was performed by using the total area of the C1s peak and Si 2p peak as measured experimentally.

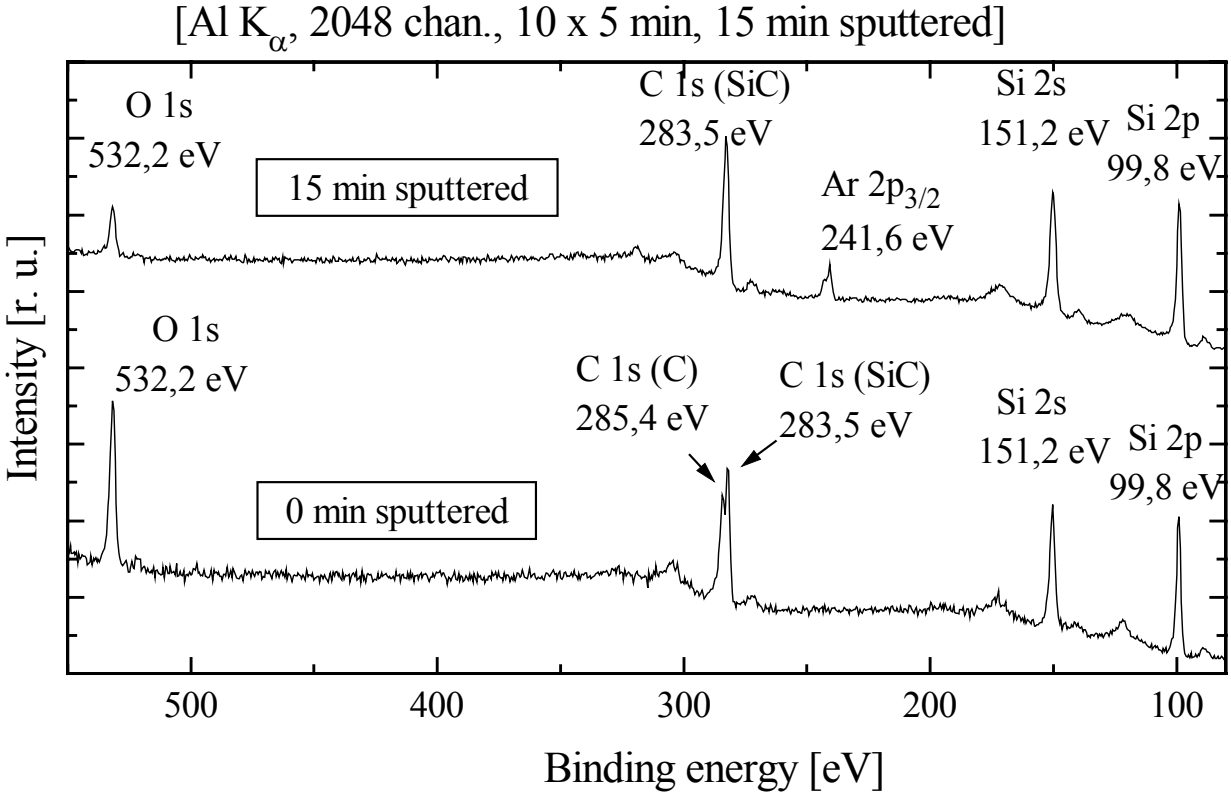

Fig. 3.11: XPS spectra of a SiC film before and after Ar^+ sputtering.

Fig. 3.11 shows that the composition of the SiC was close to [Si]:[C] 1:1. Sputtering with Ar^+ reduced the contamination due to C (CO_2) and O_2 from the air.

3.4 Scanning Electron Microscopy (SEM)

The sample surface was analyzed with a Scanning Electron Microscope (Jeol JSM-35C). In the high resolution SEM mode, the thickness was measured. With a high resolution (5 nm) and a deep penetration (some μm), the SEM could be used for topographical analyzes. For the samples with reduced electric conductivity, the sample surface was sputtered with Gold with a thickness of 100 - 150 Å. Fig. 3.12 shows 3C-SiC topographical surfaces structures. Fig. 3.12 shows a single crystalline 3C-SiC and Fig. 3.12b shows a polycrystalline 3C-SiC sample.

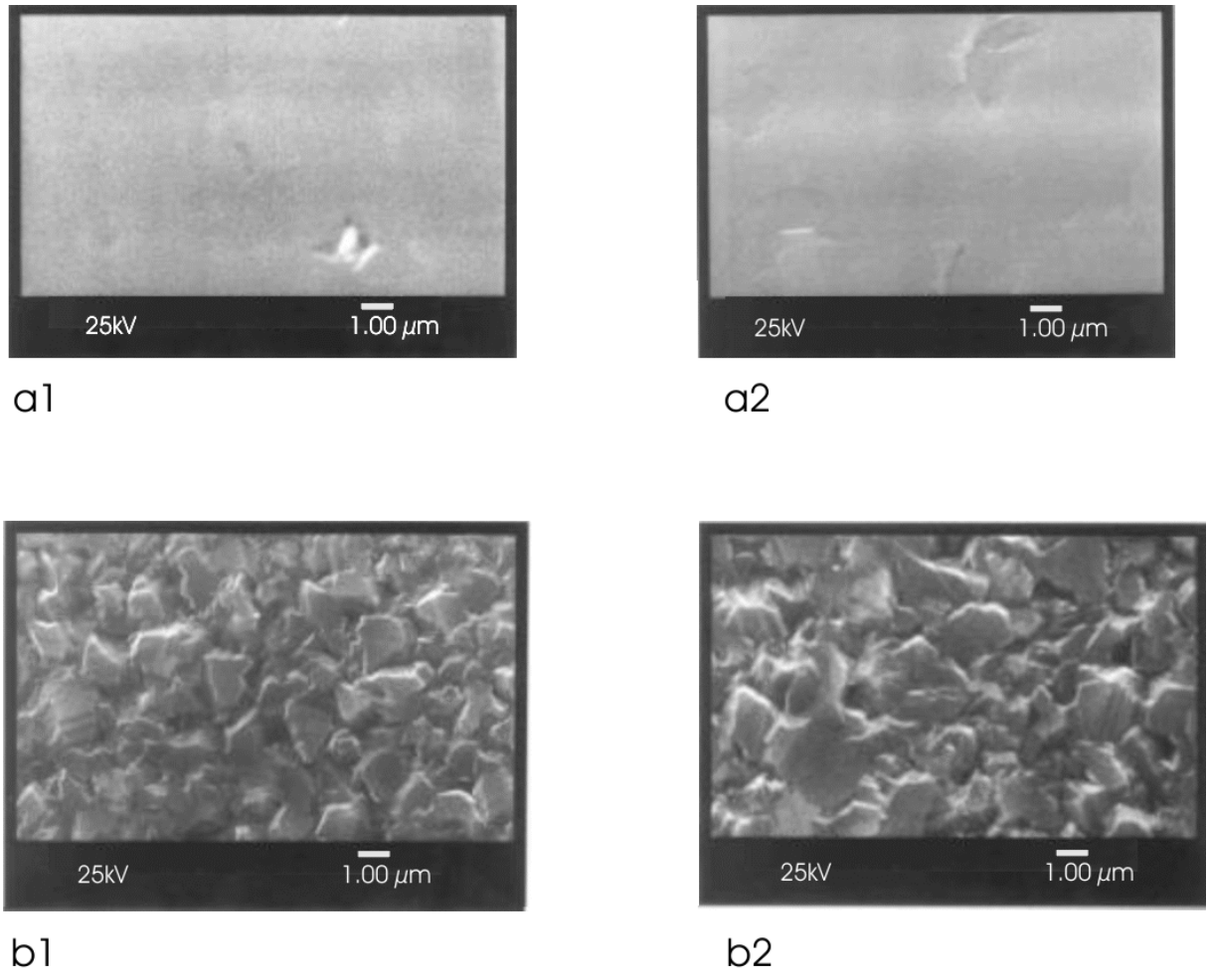

Fig. 3.12: 3C-SiC SEM images (a1) and (a2) single crystal and (b1) and (b2) polycrystalline.

The smooth surface of the first two pictures (a1, a2) proves the excellent quality of these films compared to the lower two pictures (b1, b2).

3.5 X-ray Diffraction Measurements

The X-ray Small Angle diffraction pattern was also used to determine the crystal orientation of the sample and the epitaxial quality of the 3C-SiC film. Fig. 3.13a shows the diffraction pattern of a single crystalline film of 3C-SiC, where the collinear arrangement of the diffraction peaks indicates the orientation of the 3C-SiC and Si crystals. Fig. 3.13b. shows the diffraction patterns from a polycrystalline film of 3C-SiC.

(a) 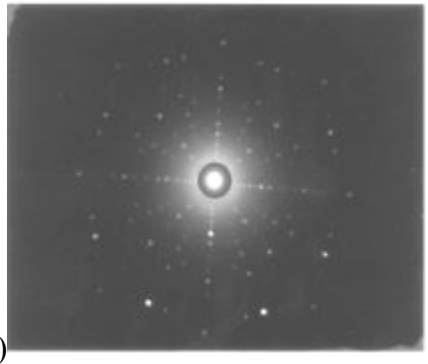 (b) 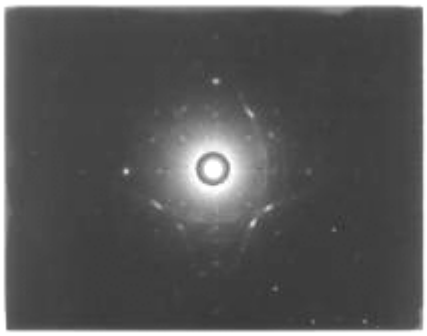

Fig. 3.13: (a) Single crystal and (b) SiC polycrystalline.

3.6 UV Spectroscopy

The estimates of the film thickness were obtained with a gravimeter and confirmed by interference patterns. The samples were weighed before and after deposition with an ultramicro-balance (Sartorius XL, accuracy 10^{-7}g) and with an interferometer (UV Spectrometer Perkin-Elmer, type 1760X). From the reflection spectrum of 3C-SiC membrane, the thickness was calculated with the following formula:

$$d = 1/2.n.(k_1-k_2) \qquad \text{Eq. 3.4}$$

d: film thickness (cm)

n: 3C-SIC index of refraction (2.6265 for 691 nm [Sc 69])

k_1, k_2: Wave number according to the interference maximal/minima (cm^{-1})

The Fig. 3.14 shows reflection spectra of 3C-SiC, where for these two examples of the 3C-SiC films. The oscillation frequency is directly proportional to the thickness of the film. The spectra in Fig 3.14a and Fig.3.14b resulted from samples with 1.2 µm and 4.2µm of thickness, respectively.

a)

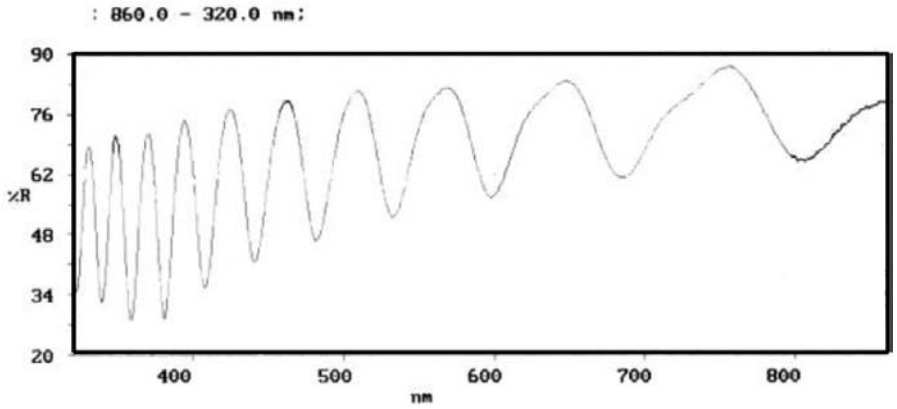

nm	%R
329.6	68.684
348.0	71.141
369.6	71.880
393.6	74.647
424.0	77.491
461.6	79.186
508.0	81.491
568.0	82.342
648.0	83.834
756.0	87.343

b)

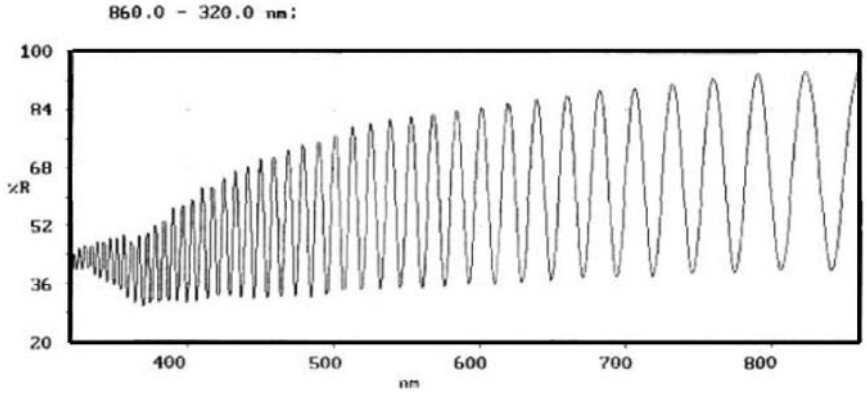

nm	%R
321.6	44.717
324.8	46.163
328.8	47.287
332.8	48.061
336.8	48.481
341.6	49.490
345.6	49.126
350.4	49.308
355.2	49.787
360.8	49.318
365.6	50.241
371.2	52.212
376.8	53.899
382.4	55.404

Fig. 3.14: Reflectivity spectra of (a) a 1.2 µm and (b) a 4.2 µm thick 3C-SiC film.

3.7 Conductivity and Hall Effect Measurements

The carrier type, the density of electrons or holes, the mobility, the conductivity, and the Hall effect, were measured by using the van der Pauw geometry [Pa 58]. In the method a square sample is contacted at its corners, where the smaller the contacts are in relation to the sample sizes, the higher is the accuracy of the measured parameters. Using the Vander Paul configuration Hall and conductivity measurements can be performed. A modulated magnetic field is applied to minimizing the potential misalignments due to contacts and or sample inhomogeneities. For a n-type semiconductor the carrier density, n, can be calculated with Eq. 3.5:

$$n = \frac{r_n}{|e| \cdot |R_H|} \qquad \text{Eq. 3.5}$$

n: carrier density

r_n: Hall scattering factor for electrons ($r_n \approx 1$)

e: elementary charge (C)

R_H: Hall coefficient ($m^3 \cdot C^{-1}$)

The Hall coefficient is defined as following:

$$R_H = \frac{U_H \cdot d}{I \cdot B} \qquad \text{Eq. 3.6}$$

U_H: Hall voltage (V)

d: Thickness of the sample (m)

I: current (A)

B: magnetic Induction (T)

The Hall mobility μ_n (cm^2/Vs) of electrons is given by:

$$\mu_n = |R_H| \, \sigma \qquad \text{Eq. 3.7}$$

σ: conductivity ($1/\Omega.m$)

The formula above is applicable for electronic conductivity and a small magnetic induction ($\mu \cdot B << 1$). The conductivity measurement was performed without magnetic field with two adjacent contact points by a constant current and on the opposite corners the voltage was measured where the resistance is defined by $R_1 = U_1/I_1$. Finally, the contact points were repeated in the opposite positions, resulting a resistance $R_2=U_2/I_2$. The conductivity values were calculated with the Eq. 3.8.

$$\sigma = \frac{\ln 2}{\Pi \cdot d} \cdot \frac{2}{R_1 + R_2} \cdot \frac{1}{f} \qquad \text{Eq. 3.8}$$

d : thickness (m)

f: correction factor (dependent on the ratio between R_1/R_2).

The magnetic field used was 0.7 T (Magnet: Physic AG, B-E22 and C3). The substrate had a high conductivity (0.01 Ω·cm) it was necessary to prepare the sample in the following way:

-The 3C-SiC membrane (5×5 mm^2) was separated from the substrate with a $HF/HNO_3/CH_3COOH$ solution. Membranes thicker than 10 µm were mechanically stable and could be used in the following process. Firstly, with a 0.5 mm steel mask, ohmic contacts were produced by sputtering of Cr/Au on the four corner points. Then, the contact was heated up to 1250 °C in an argon atmosphere, the SiC membrane was fixed to a Quartz plate and set on the sample holder in the Hall measurement apparatus. Under these conditions films with different thickness, 10 to 100 µm were analyzed.

The results of the Hall measurement for a 75µm 3C-SiC membrane agree fully with the literature (Tab. 3.4) and (Tab. 3.5): Our best result was achieved with a 75 µm thick sample.

-carrier density $n = 5.3\ 10^{16}\ cm^{-3}$,

-specific resistance $\rho = 0.5\ \Omega \cdot cm$

-electron mobility $\mu = 324\ cm^2/Vs$.

The value of the electron mobility oscillated in the measurements by a factor of 2, due to the high influence of the contact geometry [Pa 58].

Carrier Density [n] [cm^{-3}]	Electron Mobility [μ] [$cm^2 \cdot (Vs)^{-1}$]	Film thickness [d] [μm]	Reference
$3.9 - 7.4 \cdot 10^{16}$	250 – 380	max. 28	[Ni 83]
$1.6 \cdot 10^{17}$	245 – 310	4.6 – 16.9	[Se 86]
$3.0 \cdot 10^{16}$	510	max. 10	[Su 86]
$4 \cdot 10^{16} - 2 \cdot 10^{17}$	200 – 520	max. 40	[Po 87]
$6 \cdot 10^{16}$ 10^{17}	240 340	5 16	[Fe 88]
$10^{16} - 10^{17}$	200 – 400	12	[Ko 88]
$10^{16} - 3 \cdot 10^{17}$ $5 \cdot 10^{16} - 10^{17}$	200 - 600 100 – 230	max. 20 (on-axis) max. 20 (off-axis)	[Ta 90]
$3.3 \cdot 10^{16}$	395	100	[To 94]

Tab. 3.4: Published values of carrier density and Electronic Mobility from Hall effect measurement of n-3C-SiC film on Si-substrate.

Carrier Density [n] [cm^{-3}]	Electron Mobility [μ] [$cm^2 \cdot (Vs)^{-1}$]	Film thickness [d] [μm]
5.10^{16}	265	15
7.10^{16}	290	26
2.10^{16}	310	55
5.10^{16}	324	75

Tab. 3.5: Values of carrier density and Electronic Mobility from Hall effect measurement of n-3C-SiC film on Si-substrate produced with MTS precursor in this work.

From our electrical characterization measurements, a significant variation of Hall carrier density and electron mobility was not observed in function of the film thickness. The maximum in the improvement of the electrical properties seems to be reached for film at least thicker than 15 μm.

3.8 Transmission Electron Microscopy (TEM)

The TEM analysis was performed at the Institute for Material science of the University Erlangen-Nürnberg with a Philips CM 300 ultra twin primary electron energy microscope. The resulting images illustrate the defects in the 3C-SiC lattice interface and the crystal quality. Fig. 3.15 shows the pattern of the electron diffraction shows the 3C-SiC and Si crystal orientation.

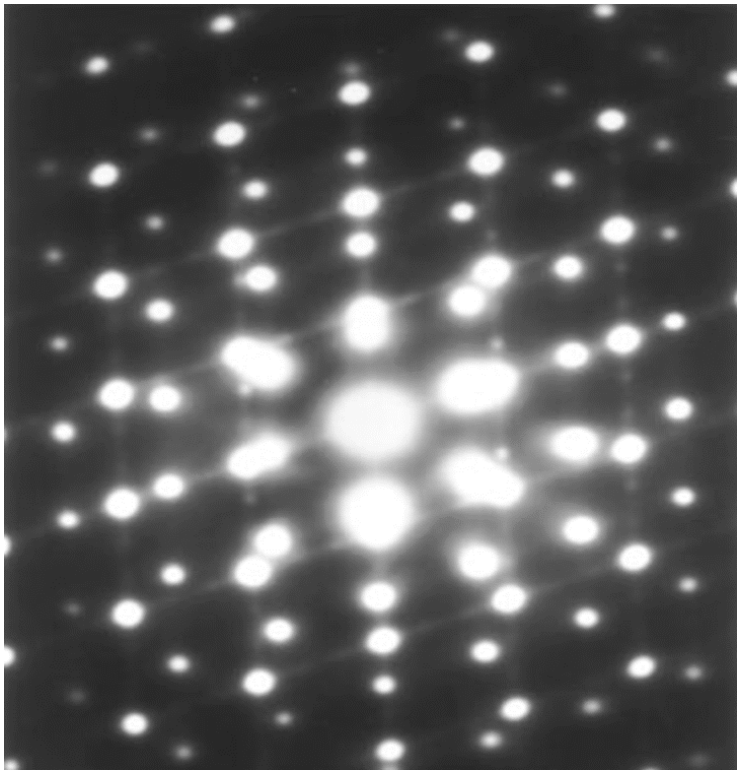

Fig. 3.15: Diffraction pattern of a 3C-SiC film measured with a 200 kV electron beam in (110) direction. The process parameters were p_{tot}= 5.25 mbar, p (H_2)/p(MTS)= 20, T_{dep}= 1200 °C, r = 2.8 Å/s, d= 5.4 µm.

According to Fig. 3.15, the diffraction points are exactly collinear, i.e., both crystals (3C-SiC and Si) have the same parallel orientation. The measurements of the distance between SiC and Si diffraction points are in precise agreement with the inverse of both lattice constants $1/(d_{SiC}/d_{Si})$.Eq. 3.9 describes the ratio between the lattice constants of 3C-SiC and Si, whereas the values A and B are measured from the diffraction pattern shown in Fig. 3.16.

$$\frac{A}{B} = 1.25 = \frac{d_{Si}}{d_{SiC}} \qquad \text{Eq. 3.9}$$

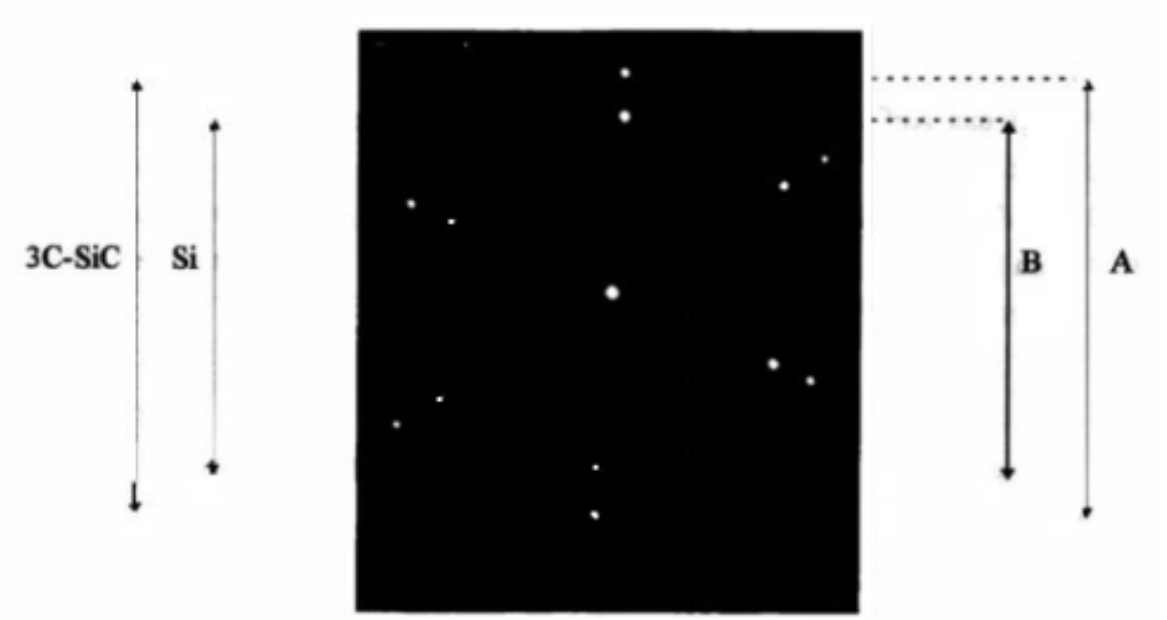

Fig. 3.16: Diffraction pattern of Si/SiC interface. Process parameters: p_{tot}= 5.25 mbar, p (H_2)/p(MTS)= 20, T_{dep}= 1200 °C, r = 2.8 Å/s, d= 5.4 µm

Fig. 3.17 shows a TEM interface image of a single crystal 3C-SiC with stacking faults and dislocations. The defects decrease with increasing thickness.

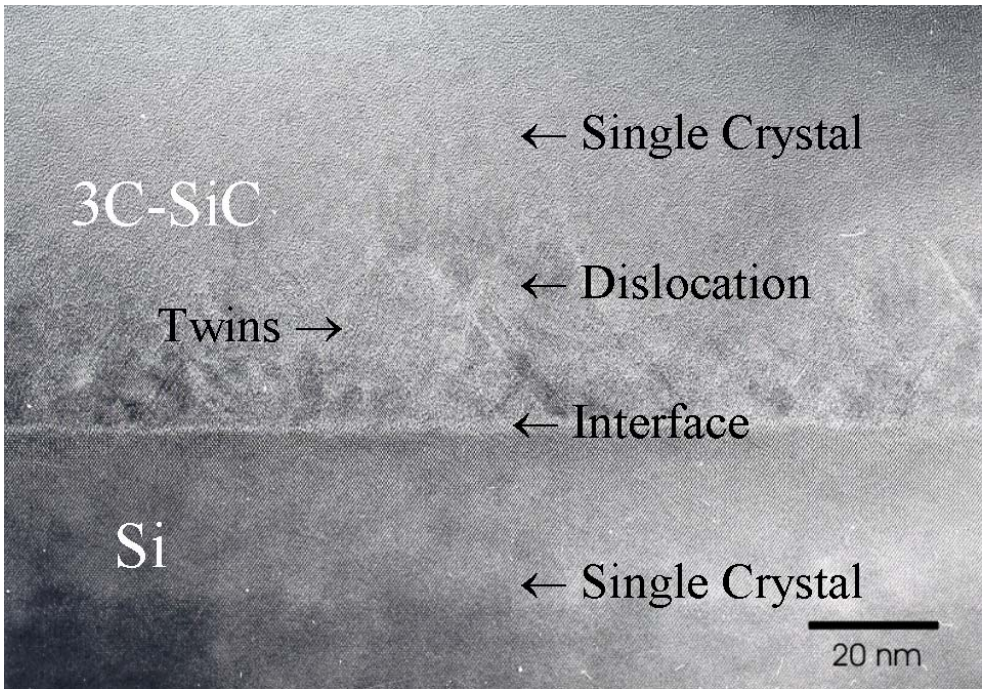

Fig. 3.17: TEM picture of a 3C-SiC/Si interface, magnification 66.000. The process parameters: p_{tot}= 5.25 mbar, p (H_2)/p(MTS)= 20, T_{dep}= 1200 °C, r= 2.8 Å/s, d= 5.4 µm.

3.9 Photoluminescence (PL)

PL was used to identify the quality and the defects of the crystals. Through light excitation electrons and holes are excited across the forbidden gap (Eg). Due to localized defects, recombination of electrons and holes generates a characteristic radiation. From a specific signal, it is possible to recognize the type of the impurity present. The excitonic recombination was measured at 5K. The excitation source was the 351nm emission line of an argon laser. The photoluminescent light was dispersed using a double grating spectrometer with focal length of 500 mm and detected by a photomultiplier. With this setup the resolution in photon energy is better than 0.5 meV.

The specific photoluminescence of 3C-SiC is described as follows:

The low temperature PL spectrum of 3C-SiC (Lely-material) has five characteristic lines [Ch 64]. The Zero Phonon Line (ZPL) 11 meV below the energy gap Eg= 2.390 eV and 4 phonon replicas TO, LO, TA, LA, see Fig 3.18. The five characteristic lines of 3C-SiC PL-spectra came from the recombination of excitons bound to a neutral nitrogen donor, (N substitutes C in SiC lattice), as confirmed by a comparison of the PL of the SiC (6H and 15R) doped with N [Ch 62,Pa 63] and with Electron Spin Resonance (ESR) of 3C-SiC doped with N [Al 71, Ch 87,Ok 88]. The ionization energy of N in 3C-SiC was reported by Zeemann as 53.6±0.5 meV [De 77] and from high Resolution IR Transmission measurements in 3C-SiC bulk as 54.2 meV [Mo 93].

Causes for the energy shift and broadening of the peaks were impurities, structural lattice defects and biaxial stress at the Si/SiC interface. The energy shift of a few meV can be mainly explained through the direct observation via PL measurements of the energy gaps caused by stress. In comparison, the energy shift corresponding to the PL stress is only 0.12-0.25 meV.

There are additional signals in the PL spectra at low energies:

-D_1 peak at 1.972 eV (628 nm): Mainly due to point defects, such as caused by ion implantation. The position of this line is almost the same in all samples and does not depend from the crystal quality.

-G-band at 1.9 eV (652 nm): The line is related to dislocation defects in the lattice. In this work, it is shifted by about 10 meV, in comparison to literature values [Ch 88], and depends on the film thickness.

The low temperature PL spectrum is shown in Fig. 3.18. The measurements were performed for a 7.5 μm thick 3C-SiC film on Si(100). Near the ZPL line the phonon replicas TA (X), LA(X), LO(X), TO(X) are observed.

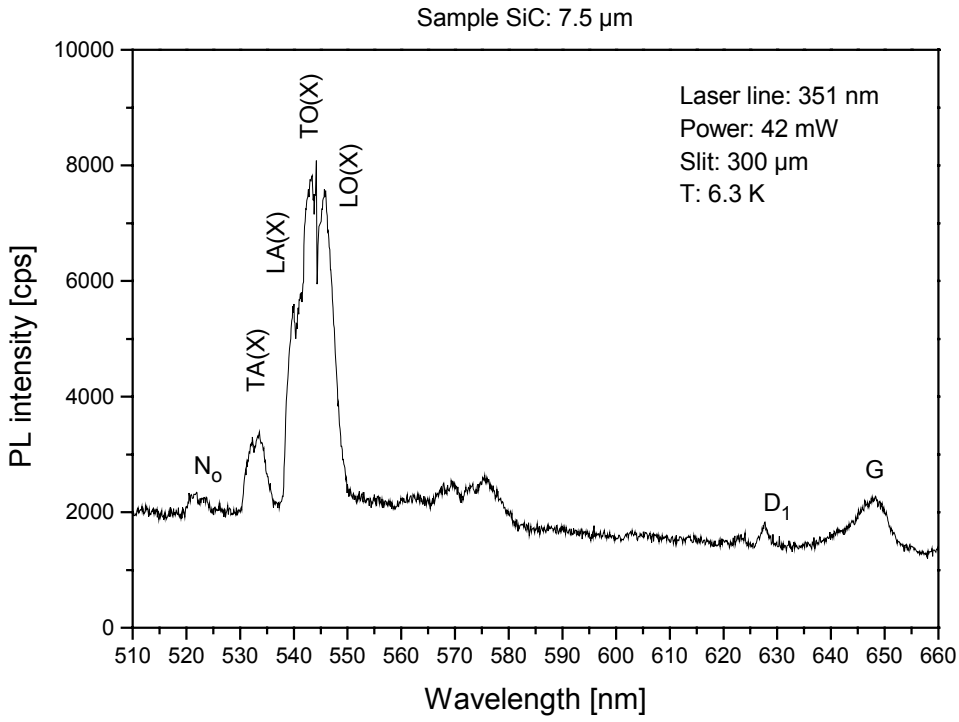

Fig. 3.18: PL spectra of a 7.5 µm 3C-SiC film on Si(100). The measurement was performed at 5K with an excitation line of 351 nm. The process parameters were p_{tot}= 5.25 mbar, $p(H_2)/p(MTS)$=20, T_{dep}= 1200 °C, r = 2.8 Å/s.

The energy positions of the five PL are shown in Tab. 3.6, and compared to literature values.

N_o [eV]	TA [eV]	LA [eV]	TO [eV]	LO [eV]	Crystal	Reference
2.379	2.3327	2.2995	2.2846	2.2762	3C-SiC Lely crystal	[Ch 64]
2.378	2.332	2.298	2.283	2.275	10µm 3C-SiC on 3C-SiC	[Ni 95]
2.3727	2.3256	2.2928	2.2779	2.2703	25µm 3C-SiC on Si(100)	[Ch 88]
2.3779	2.3316	2.2986	2.2836	2.2751	15µm 3C-SiC on Si(100)	[Ch 88]
2.3789	2.3326	2.2985	2.2843	2.2751	7.5 µm 3C-SiC on Si(100)	This work
2.3784	2.3317	2.2990	2.2851	2.2754	50 µm 3C-SiC on Si(100)	This work

Tab. 3.6: Published values of five main PL lines of 3C-SiC on Si-substrate from different sources. These values are in good agreement with those of the (7.5 and 50) µm 3C-SiC film of this work.

Fig. 3.19 shows the energy shift of the TO(X) line as function of the film thickness. The energy shift of the TO(X) line in the 3C-SiC film produced with LPCVD (1200°C with MTS/H_2) correspond almost to stress free systems, especially if compared to the Buffer layer technique (1350°C with SiH_4/C_3H_8, [Ch 88]). The relaxation of the lattice with distance from the interface is proved through the 50µm thick film (1.4 meV).

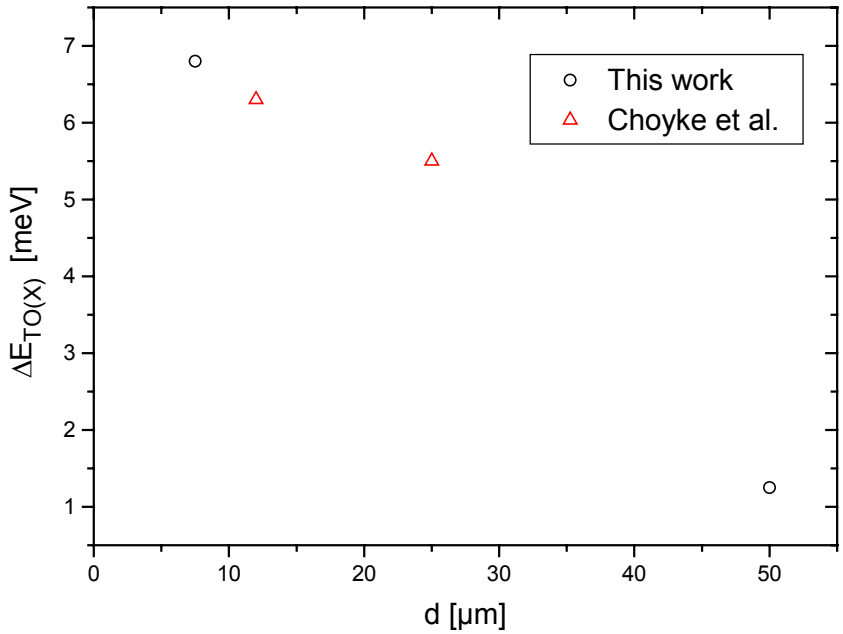

Fig. 3.19: Energy shift of the TO(X) line, as function of film thickness in comparison with data from Choyke et al. [Ch 88]

For the several thicknesses of 3C-SiC films on Si(100), it was possible to calculate the biaxial stress in the 3C-SiC film from the small energy shift of the position of ZPL line and the values of the multiple phonons from the 3C-SiC single crystal (Fig. 3.19).

The phonons of the 50µm 3C-SiC film were excited with an Ar laser beam, wavelength of 351 nm, and show only a low energy shift as observed in the D_Γ and G_Γ.

The influence of the Si/SiC interface to the PL spectra decreases with the increase of the film thickness as shown for the 50µm 3C-SiC (Fig. 3.20).

The FWHM of the TO line is almost 4 meV for 7.5µm film and 1.6-1.8 meV for 50µm film and therefore confirms the better quality of thick films.

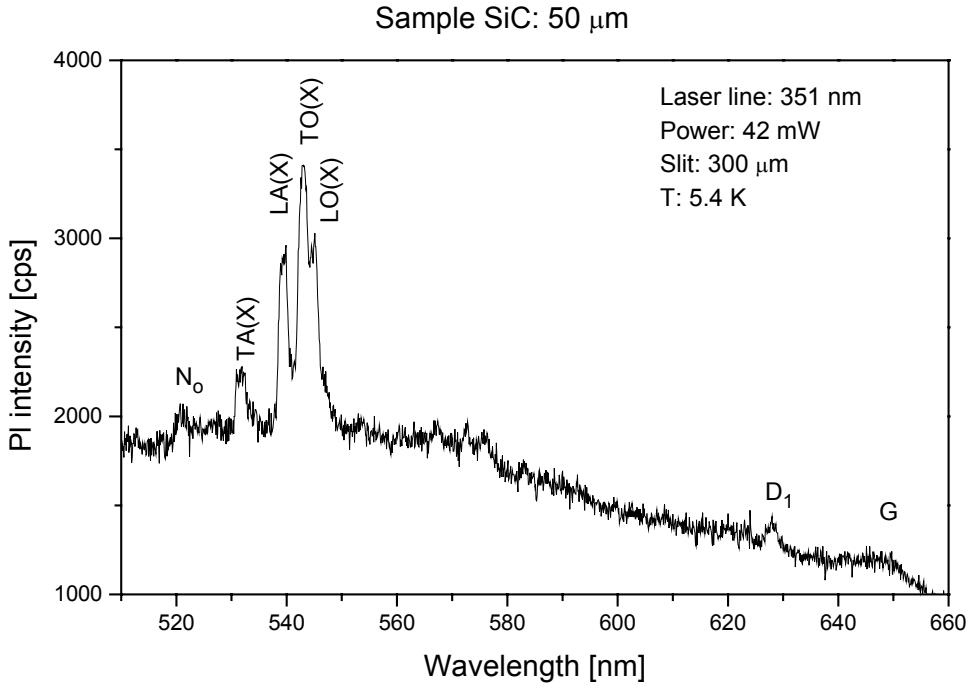

Fig. 3.20: Photoluminescence spectrum of a 50 μm thick 3C-SiC film on Si(100). The process parameters were p_{tot}= 5.25 mbar, p (H_2)/p(MTS)= 20, T_{dep}= 1200 °C, r= 2.8 Å/s, d= 50 μm.

With increasing film thickness, the intensity of D_I and G bands decrease. A formula that can describe the crystal quality is the relationship between the intensity of the G band and the intensity of the strong PL line TO(X) [Ch 88].

$$\rho = \frac{I(G)}{I(TO)} \qquad \text{Eq. 3.10}$$

with

ρ = quality of the crystal

I(G) = intensity of the G-defect band

I(TO) = intensity of the TO PL line

The Fig. 3.18 and Fig. 3.20 show a ρ values of 0.024 for the 7.5 μm thick film and ρ of 0.01 for the 50 μm thick film. Comparatively, Choyke [Ch 88] describes values for ρ of 0.25 (13 μm 3C-SiC on Si(100)) and 0.07 (15 μm 3C-SiC membrane).

4 CONCLUSION OF PART I

This research focused on the crystal growth of 3C-SiC on Si(100) substrate with MTS precursor via LPCVD ($5.25 \cdot 10^{-3}$ mbar) at a temperature of 1200°C. Different from the APCVD technique, the LPCVD method produced homogeneous films on a large area. This process used a stoichiometrical precursor by a single molecule from the MTS precursor, which differs from the Buffer layer process with silicon and carbon originating from different molecules (C_3H_8 and SiH_4).

The investigations of 3C-SiC heteroepitaxy on silicon showed the structural characterization of the films. The best procedure for the 3C-SiC growth by deposition of the precursor is to start at 600°C, whereas a direct start at 1200°C will create polycrystalline SiC. During this ramp from 600°C to 1200°C the Si substrate is completely covered by 3C-SiC avoiding Si evaporation and, consequently, voids on the surface. The best 3C-SiC films were obtained at a total pressure of 5.25 mbar, an H_2 flux of 100 sccm, a precursor/hydrogen ration of 1:20, a temperature ramp of 5 °C/sec, starting at 600 °C, and finally a constant temperature of 1200 °C. To optimize the smoothness of the surface, the total pressure was decreased slowly at the end of the procedure.

Using these parameters and commercial distillated MTS and H_2, 3C-SiC epitaxial films were produced with a thickness between 0.1 and 100 µm on Si(100). Compared to APCVD, LPCVD allowed a deposition temperature 150-200 °C lower, generating good quality of the 3C-SiC films with less lattice defects. Experiments using high-pressure depositions (266 mbar) with a deposition rate of 4 Å/s were made and resulted in a 3C-SiC polycrystalline film. A pre-nucleation of the precursor occurred in the gas phase resulting in the formation of a polycrystalline film on the Si substrate.

The effect of the surface reaction of Si and C species on the growth mechanism showed that the film became epitaxial by suppressing the gas phase reaction between Si and C species while the film was polycrystalline in the case that Si species reacted freely. From the structural, optical and the electrical characterization follows that by growing thicker samples up to 100 µm some optimization of the crystal quality could be achieved, but 10 µm are in fact sufficient for high quality of the 3C-SiC samples with the growth system and at the growth condition adopted for this work.

For future work, a promising perspective is to reduce the deposition temperature to reduce even more the crystal defect density. This could be achieved by using precursors with weaker bonds between halogen, Si and C as in the case of MTS.

Part II

Silicon crystal growth by OMCVD

5 Introduction to Silicon Deposition

CVD has been developed rapidly in recent years as a method to produce metal films for a variety of applications in the microelectronics and coatings industries [Ko 94]. Accordingly the exact arrangement of a CVD apparatus can vary widely depending on the particular application [Hi 93].

OMCVD is an attractive method for semiconductor technology because it offers good step coverage. The metal-bearing vapor can reach around asperities and into crevices to give a fully conformal surface coverage over a wide range of topographical profiles. It is simple to handle and has a relatively low cost, compared to physical vapor deposition systems, which also suffer from the effects of delaminating and poor step coverage.

OMCVD is a well-developed technique to fabricate thin films used for semiconductors and micromechanics. An organometallic (OM) molecule can be volatilized at a specific temperature and thereby be delivered to the surface of the sample through a vapor phase at relatively low pressure. When the OM molecule reaches the sample surface, which is held at an elevated temperature, the molecule decomposes thermally, allowing its organic sub-products back into the vapor phase, where they are pumped away, leaving the metal atom from the molecule in the sample.

In the case of the OMCVD, a gaseous species is used and the methallorganic precursor element reacts to form a compound.

Based on the more recent OMCVD applications to develop a metallization layer on a silicon substrate, Prof. Robert West, Department of Chemistry, at the University of Wisconsin, Madison, USA, produced the first stable silylene precursor. They were used in this work. These materials are offering extremely exciting possibilities as precursors to produce thin layers of silicon in an alternative way.

The study of these silylene is interesting since the devices are usually made by several metallization steps and the selective growth from Si via silylene means to reduce steps of lithography and etching in the metallization process.

The selective deposition of silylene on silicon is similar to the deposition of germylene. In the new silylene molecule, a Si atom replaces the Ge atom of the original germylene molecule and thus, should make a selective deposition of the molecule possible.

A non-selective deposition of silicon via CVD is well known with Silane; nevertheless, Silane is explosive and toxic.

The aim of this second part was the investigation of these new precursors to produce a thin layer of silicon using the OMCVD technique and new deposition procedures. Furthermore, the saturated vapor pressures from these precursors were compared with OM precursor of germanium [Gl 93], [Pr 95], [Ve 96].

This requires mainly a very precise control of the temperature, pressure and reactor shape. The investigation was performed when the precursor was exposed to a heated Si surface at a relatively low pressure (specified in chapter 6). One of the first steps for the comprehension of the molecule activities is to understand their adsorption and desorption characteristics. Regarding the strength of the adsorbate-surface bond, the state of the OM adsorption and the viability of intact molecular thermal desorption were integrated into this work.

Investigations with Scanning Electron Microscopy, X-Ray Photoelectron Spectroscopy, X-ray diffractometry and Energy Dispersive X-Ray Spectroscopy were made to characterize the reaction products and to elucidate the dissociation as a function of thermal energy.

OMCVD has been used for deposition of metallic structures at relatively lower temperatures and pressures. Nevertheless, the application toward the fabrication of compound semiconductors from single source precursors is both new and significant.

In Tab. 5.1 the 3 precursors used in the second part of this thesis are summarized:

IUPAC name	Accepted name
1,3-di-2-methyl-2-propyl-1,3-diaza-2-silatert-butyl	Z-diaminodisilyldisilene (tetramer)
2-diazido-1,3-di-tert-butyl-1,3-diaza-2sila-olidine	silylene diazide
1,3-di-tert-butyl-1,3,2-diazasilolidine	silylene dihydride

Tab. 5.1: The IUPAC and accepted names of the precursors used in the second part of this Thesis.

The stable structure for the Z-diaminodisilyldisilene is the "disilyldiaminodisilene" (solid powder) [We 96]. See Fig. 5.1.

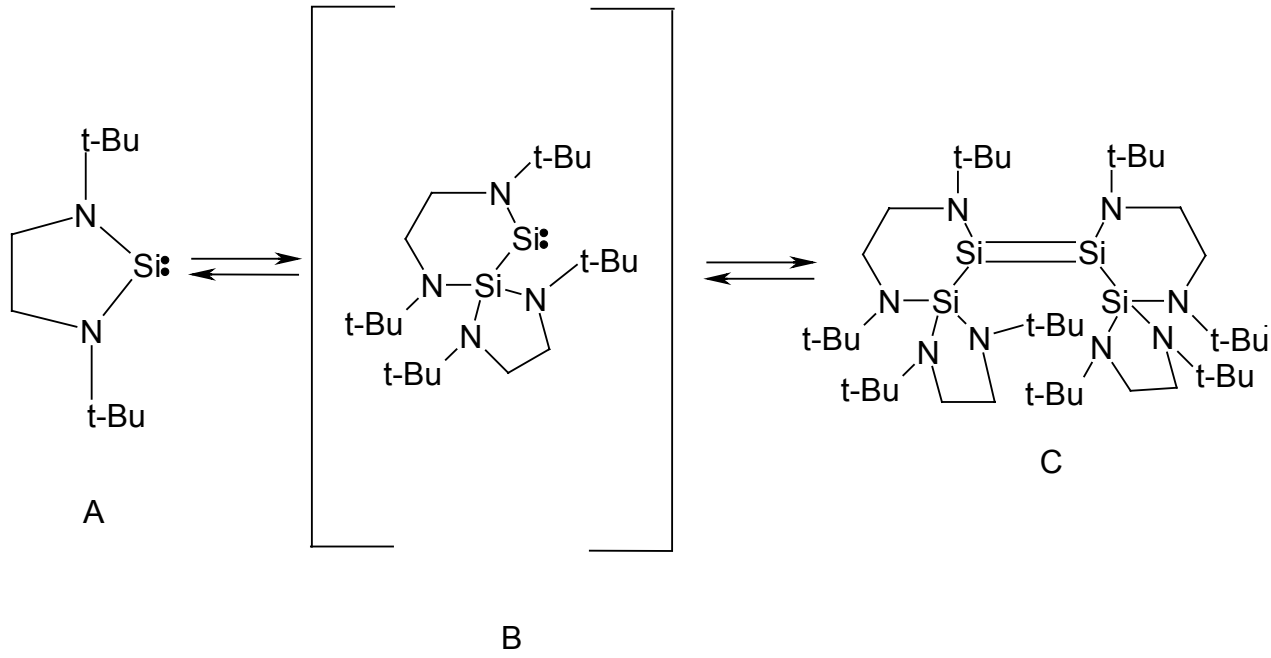

Fig. 5.1: Z-diaminodisilyldisilene with its particular structures: Silylene (A), diaminosilylene (B), disilyldiaminodisilene (C).

The stable structure for the silylene diazide, illustrated in Fig. 5.2, is the "silylene diazide" (liquid solution).

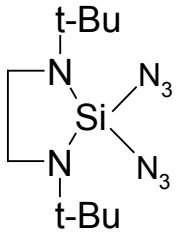

Fig. 5.2: Molecular structure of the silylene diazide"2-diazido-1,3-di-tert-butyl-1,3-diaza-2sila-olidine"

The stable structure of silylene dihydride, shown in Fig. 5.3, is the " silylene dihydride" (liquid solution).

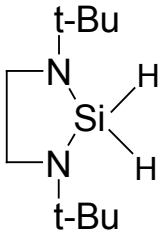

Fig. 5.3: Molecular structure of Silylene dihydride 1,3-di-tert-butyl-1,3,2-diazasilolidine

The precursors were stored under either vacuum or pure argon. Exposure to water provokes hydrolysis.

6 OMCVD Apparatus

6.1 Reactors

The growth of Si thin films was executed in two apparatus where the principal differences were the size of the reactor and the system of heating.

In the case of the reactor 1 (small reactor), the required amount of precursors was smaller than for the large reactor. The sample was positioned 6 cm from the sample temperature was limited by 450°C. The reactor 2 (large reactor) had a resistive heating system that could produce a sample temperature up to 650°C. A larger amount of precursors was required in this case and the sample was placed at a distance of 60 cm from the gas-inlet.

6.1.1 Reactor 1 (Small Reactor)

In a first series of experiments, the Z-diaminodisilyldisilene and silylene diazide were tested in the small reactor. The apparatus shown in Fig. 6.1 consists of a T form Pyrex glass tube manufactured with the following geometry: length of 28 cm, internal diameter of 1.5 cm and volume 78.5 cm^3, plus a bottle for the precursor with volume of 34.56 cm^3. The substrate holder (3) was a quartz glass cylinder positioned in the center of the reactor chamber (1), located 6 cm from the bottle with precursor (2). The bottle was equipped with a Teflon edge valve and was filled with the precursor under 99.99 vol % of pure argon.

The substrate holder was heated with an electrical cable heater, controlled with a thermocouple and a temperature controller device.

A MKS Baratron measured the pressure during the deposition.

A Teflon edge valve controlled the pressure in the reactor and the gas flow rate. The sample was positioned in the middle of the reactor parallel to the gas flow.

The Fig. 6.1 shows the small Pyrex glass reactor with the valves and the bottle with the precursor.

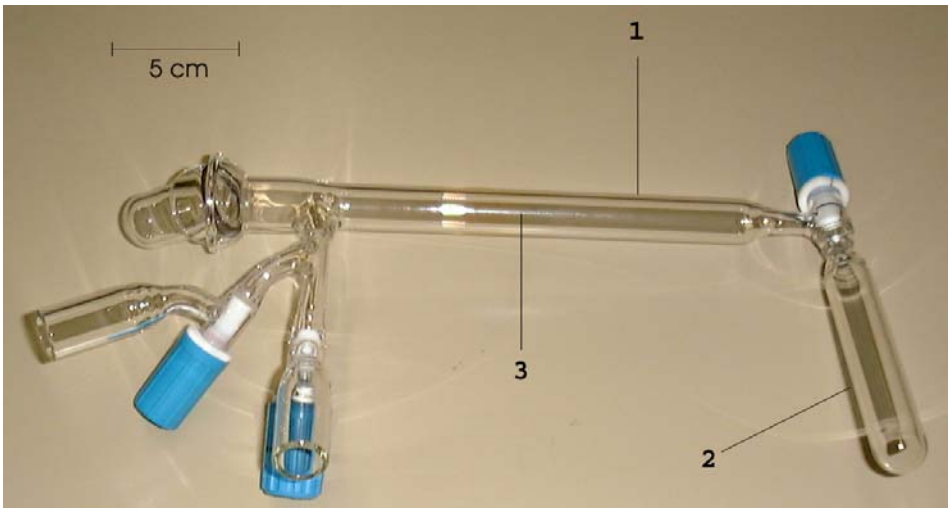

Fig. 6.1: Picture of the small reactor apparatus used for the OMCVD deposition with the reactor chamber (1), the precursor reservoir (2) and the substrate holder (3).

6.1.2 Reactor 2 (Large Reactor)

Reactor 2 is shown in Fig. 6.2. The apparatus consists of a T form Pyrex tube reactor (I), manufactured with a diameter of 4.6 cm and terminated by two metal flanges with a length of 6.6 cm. The substrate holder has a diameter of 3 cm (II) and was electrically heated to reach stable temperatures of 600°C.

The bottle with stainless steal contained the precursors and was equipped with flanges filled under 99.99 vol % of pure argon.

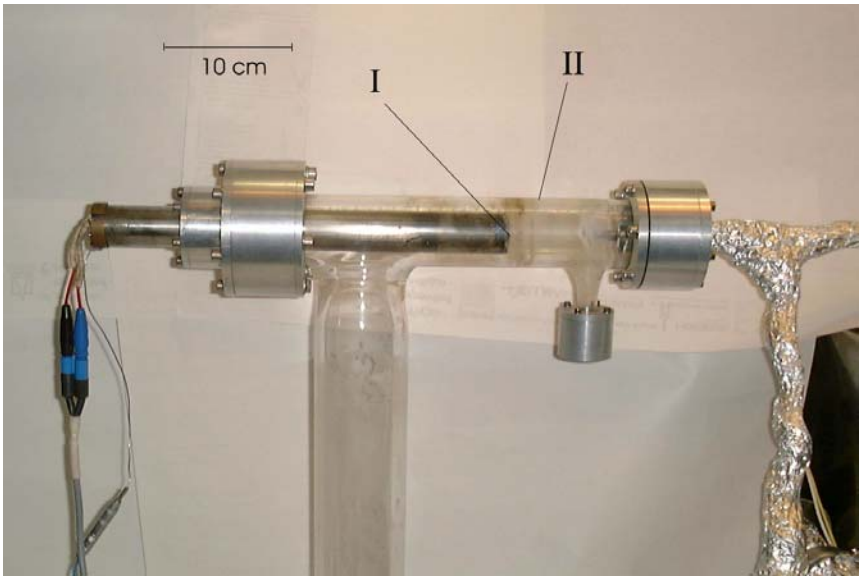

Fig. 6.2: Picture of the larger reactor apparatus used for the OMCVD deposition studies. The picture shows the sample holder (I) and the glass reactor (II).

The sample holder of the larger reactor was positioned perpendicular to the gas flow. A picture of the sample holder is shown in Fig. 6.3.

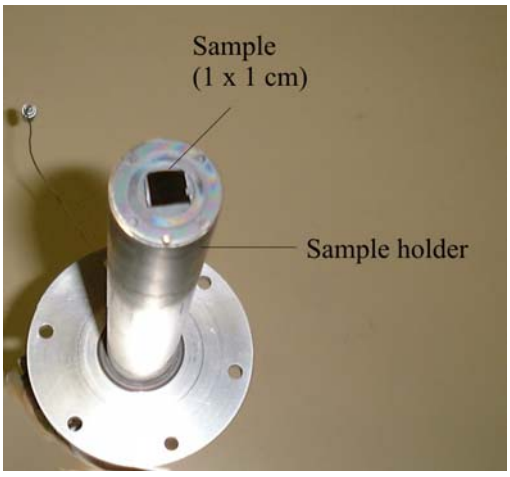

Fig. 6.3: Picture of the sample holder for the larger reactor apparatus used for the OMCVD deposition.

Fig. 6.4 shows a picture of the thermostat used to regulate the specific temperature of the precursor to an accuracy of ± 0.1 °C.

Fig. 6.4: Thermostat used to regulate the temperature of the precursor. The precursor bottle was located inside the tank with pure distillated water.

The growth of the silicon film takes place directly via the reaction between the precursor from the bottle and the hot surface of the silicon wafer substrate.

Fig. 6.5 shows a detailed view of the OMCVD apparatus with its reactor, pump and pipe system.

The pressure in the reactor and the gas flow rate were controlled by stainless steel leak valve (9) and a throttle valve (10).

Penning (6) and Pirani (7) vacuum gauges connected to the system allowed the process control. All flanges were made of aluminum and Viton O-ring gaskets. The large reactor with its glass cylinder (4) and the sample holder (5) and the small reactor with its reactor chamber (1), the bottle with precursor (2) and the substrate holder (3) are the central parts of the apparatus. These were evacuated by a turbomolecular drag pump (12) (170 l/s) in series with a two stage rotary pump (14) (8 m^3/h). A Roots pump (13) with a pumping rate of 70 l/s was also used at a high gas-flow instead of the turbopump. The pressure during the deposition was measured by a heated MKS Baratron (11). A bottle with a thermostat (8) and the thermocouple with the temperature controller (15) are also shown.

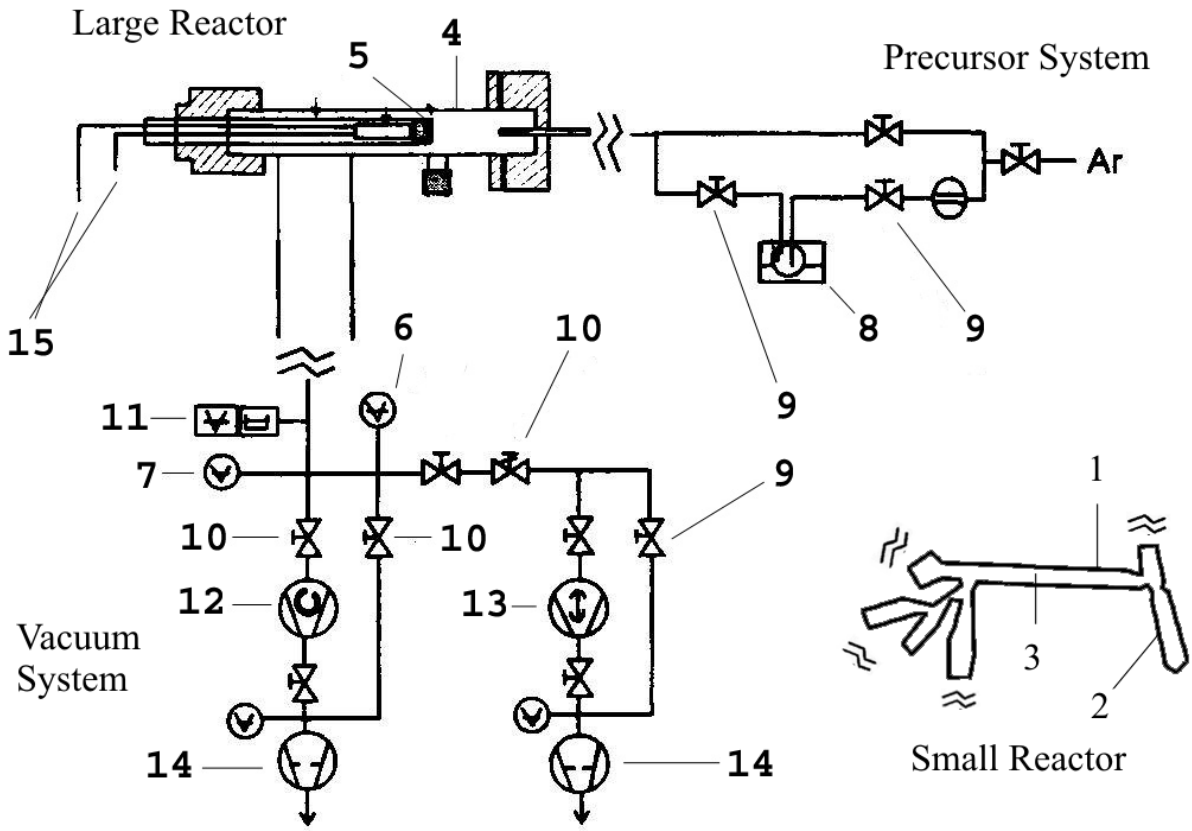

Fig. 6.5: Schematic diagram of the OMCVD apparatus with the reactor, pumps and pipe system.

6.2 Optimization of Deposition Parameters

6.2.1 Control of the Pressure, Temperature and Vacuum System

To increase the reproducibility of the experiments, the vacuum system was checked every day and the leak rate determined frequently. The typical background pressure and leak rate were about $1.0 \cdot 10^{-5}$ mbar and $3.2 \cdot 10^{-5}$ mbar.l/s, respectively.

A digital self-adjusting controller, with an accuracy of 0.5 °C was used for regulation of the temperature. A capacitive vacuum gauge (Baratron) with an accuracy of 0.025 mbar was used for measuring the pressure.

6.2.2 Silicon Surface Cleaning

The Silicon wafer (100) of thickness 0.68 mm was cut in small square segments of 0.5 cm^2 for reactor 1 and square segments of 1.68 cm^2 for reactor 2.

Two techniques were used to clean the surface of the samples for the experiments.

As the first technique, the sample was immersed in a solution of 5 % HF for 30 seconds at room temperature and then dried in a pure Ar atmosphere before placing it in the reactor chamber.

For the second technique, a RCA cleaning procedure was used. A description of this method has been given in chapter 2.

After the cleaning step, the sample was free of impurities.

7 Z-diaminodisilyldisilene

7.1 Saturated Vapor Pressure

The saturated vapor pressure was measured at specific temperatures with a heated Baratron attached to the bubbler. In Fig. 7.1, the saturated vapor pressure is plotted as a function of the temperature as a linear increase of the temperature results in an increase of the saturated vapor pressure.

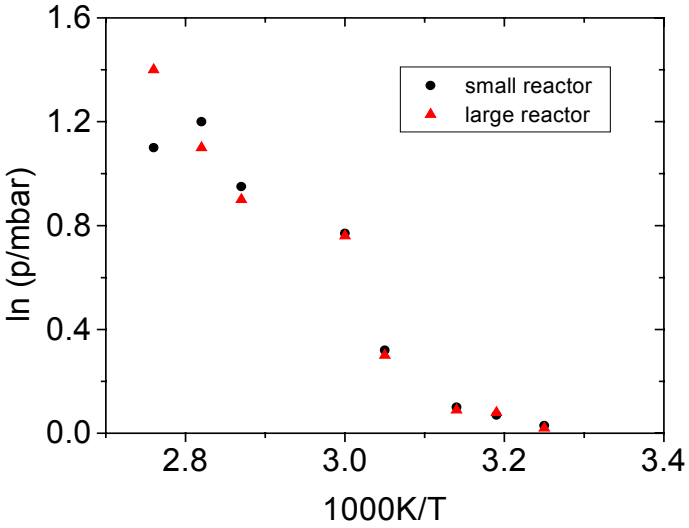

Fig. 7.1: Saturated vapor pressure of Z-diaminodisilyldisilene

7.2 Concentration of Volatile Molecules in the Bubbler

The molecular concentration at a specific temperature in the bubbler was an important parameter used to estimate the precursor concentration in the reactor. The correlation between the number of molecules of Z-diaminodisilyldisilene versus the temperature is shown in Fig. 7.2.

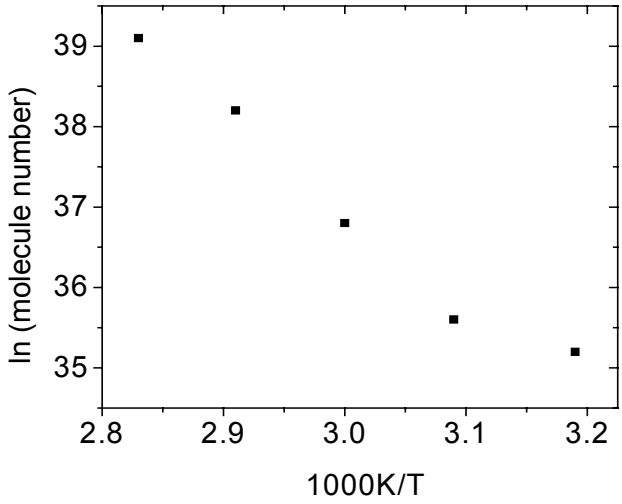

Fig. 7.2: Number of molecules in the bubbler versus temperature.

The number of molecule increased exponentially with temperature. The method to determine the number of molecules was obtained from the ideal gas Eq. 7.1

$$pV=NkT \qquad \text{Eq. 7.1}$$

with N/V as the concentration of molecules, k is the Boltzmann constant and T the absolute temperature of the bubbler.

The following formulated Eq. 7.2 was used to calculate the evaporation coefficient.

$$\phi = \alpha.n.v_{th}.A \qquad \text{Eq. 7.2}$$

with

α = evaporation coefficient

n = molar concentration

v_{th} = thermal velocity

A = area

ϕ = evaporation flow

$$v_{th} = \sqrt{\frac{3kT}{m}} \qquad \text{Eq. 7.3}$$

with

k = Boltzman constant

T = Absolute temperature

m = mass

from Eq. 7.1,

resulting for Z-diaminodisilyldisilene: $\alpha = 4.8 \cdot 10^{-5}$

The Fig. 7.3 shows the vapor coefficient of the Z-diaminodisilyldisilene versus the reciprocal absolute temperature.

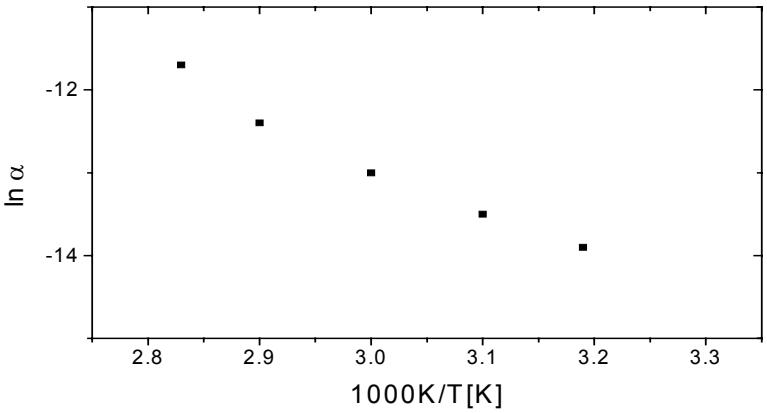

Fig. 7.3: Z- diaminodisilyldisilene vapor coefficient versus the reciprocal absolute temperature

In Fig. 7.2, the highest temperature of 80 °C corresponds to a total of $1.0 \cdot 10^{17}$ molecules in the bubbler. This number of molecules should have been enough to produce a coating after a short time of deposition, however, a film could not be observed on the substrate.

The Z- diaminodisilyldisilene precursor was tested in the monomeric form with THF stabilizing solvent and in its polymeric form.

Due to its vapour pressure the precursor in monomeric form has to heated in the bubbler to 80°C.

At this temperature a reasonable flow of gas can be transferred to the growth reactor. Nevertheless, the high instability of the monomeric form causes its polymerization before reaching the Si substrate. In the polymeric form, no Si film could be deposited, disqualifying this precursor for Si deposition.

8 Silylene Diazide.

8.1 Saturated Vapor Pressure in the Bubbler

The saturated vapor pressure of silylene diazide was smaller than the saturated pressure of Z-diaminodisilyldisilene. For example, at a temperature of 60°C, Z-diaminodisilyldisilene presented a saturated vapor pressure of 0.51 mbar whereas for the silylene diazide, the saturated vapor pressure was 0.11 mbar. However, due to the higher temperature of the substrate, the experiments with silylene diazide resulted in deposition of a silicon film. Fig. 8.1 shows the saturated vapor pressure for Silylene diazide.

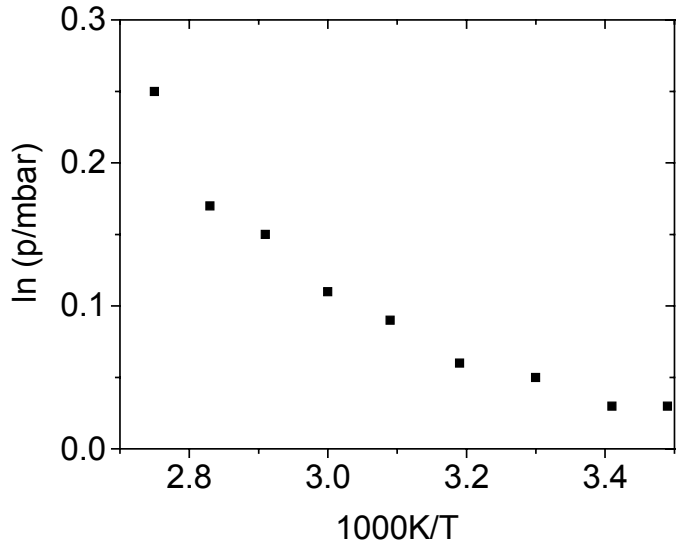

Fig. 8.1: Silylene diazide vapor pressure versus temperature

As for Z-diaminodisilyldisilene, the experiments with silylene diazide show that the vapor pressure increases exponentially with a linear increase of the temperature.

8.2 Concentration of Volatile Silylene Diazide Molecules

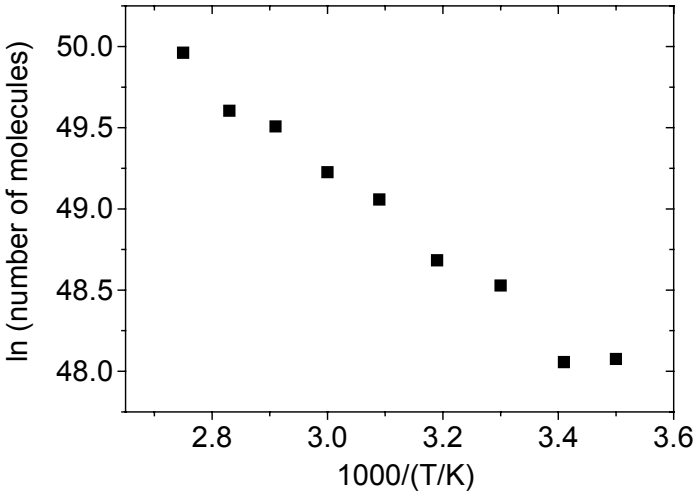

Fig. 8.2: Number of Silylene diazide molecules versus temperature

8.3 Table of Deposition Parameters

A summary of the series of experiments using silylene diazide is shown in Tab. 8.1.

The pressures, temperature of the bubbler, temperature of the substrate and deposition time were varied to determine the conditions for deposition.

Pressure (mbar)	Temperature of the Bubbler (°C)	Substrate Temperature (°C)	Time (minutes)	Deposition
1-5 (2)	50	150-350	60	no
1-5 (3)	80	400	60	no
1-5 (3)	90	450-500	60	no
1 (4)	90	550	60	yes(1)
1 (4)	95	600	60	no
1 (4)	95	650	240	yes
1000	-	Flame	0,017-0.083	yes

Tab. 8.1: Correlation between temperature, deposition pressure, temperature of the bubbler, temperature of the reactor and time process for silylene diazide deposition. (1) The film is thinner than 0.1 μm., (2) Small reactor, (3) Small and large reactor, (4) Larger reactor.

A systematic variation of the parameters leaded to the identification of the temperature as the dominant factor for a successful deposition. The reaction with silylene diazide started only at temperature of 550°C (1).

Additional experiments were also carried out to test the reproducibility of the experiments performed by the group of Prof. R. West, where a glass ampoule was used. The experimental results from these tests of Prof. West were not conclusive, though they gave important additional information. For this experiment, a glass ampoule with diameter of 3 and 15 mm was evacuated, cleaned and filled with argon. 1.0 ml of silylene diazide was put inside in the ampoule and a series of tests was executed.

The ampoule and precursor were heated with a flame for 5, 60, 120, 180, 240 and 300 seconds. The result was a film deposited on the glass from the decomposition of the precursor, which indicated the possibility of a successful reaction occurring at a relatively high temperature. This experiment motivated the construction of a sample holder with a higher maximal temperature, successfully experiments were completed in larger reactor at a temperature of 650 °C.

The growth rate was determined by the difference of the weight before and after the deposition, with an accuracy of the measurements of ± 0.1 μg (corresponding to 1 Å).

8.4 Scanning Electron Microscopy Pictures of the Silicon Film

Fig. 8.3 shows the morphology of the silicon film produced by using silylene diazide. The picture shows a polycrystalline film with several nucleation sites, silicon islands with diameter of 0.2 μm.

The Scanning Electron Micrograph was recorded with an electron beam corresponding to the voltage of 10 kV.

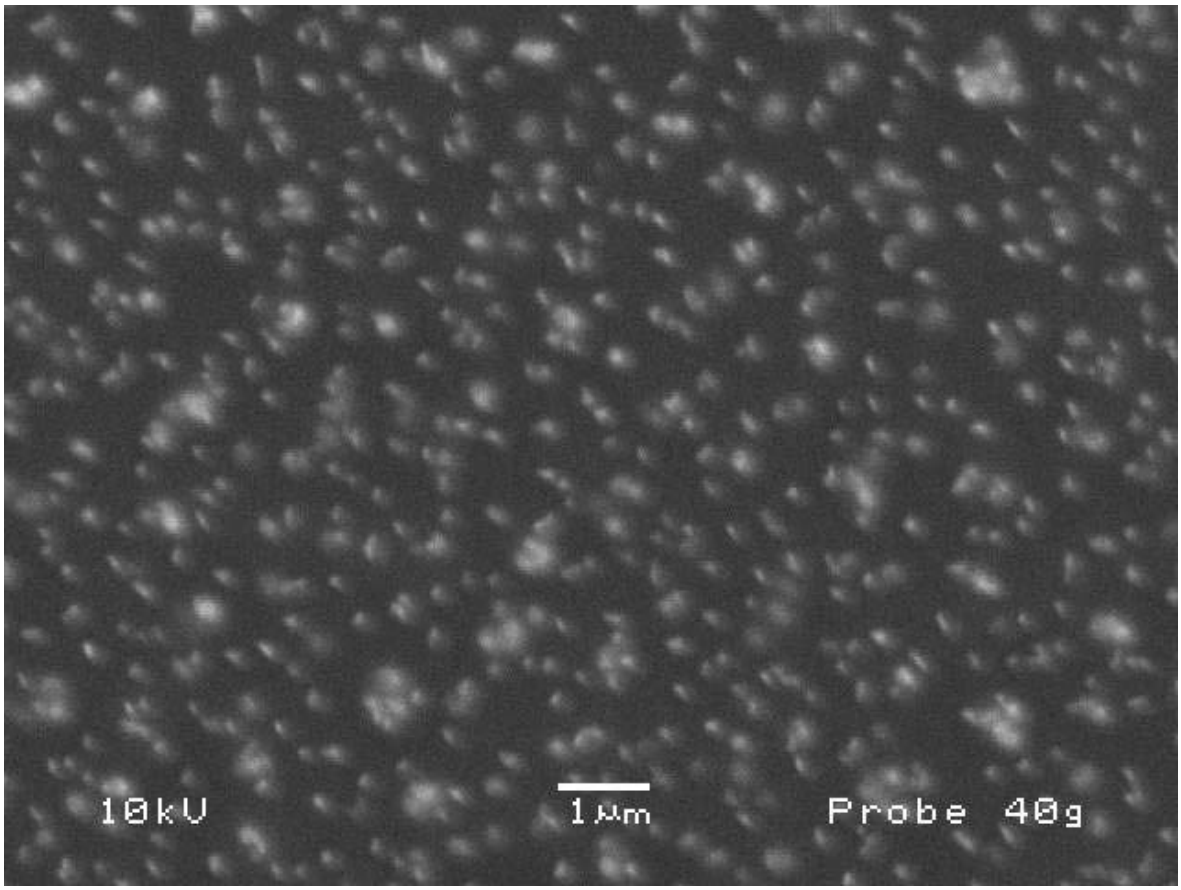

Fig. 8.3: Scanning Electron Micrograph (magnification 10000) of a Si film deposited on (100) Si surface. Growth conditions: T: 650°C, P: 1 mbar, deposition rate: 0.27 Å/s, thickness: 0.39 Å

8.5 X-ray Photoelectron Spectroscopy of the Silicon Film

The XPS used here, was described in the section 1.

The XPS spectrum of the film deposited using silylene diazide is shown in Fig. 8.4 prior to 30 minutes of argon sputtering. The characteristic peaks corresponding to the elements nitrogen, oxygen, hydrogen, silicon and carbon are marked.

The oxygen (1s) peak shows an intensity of 10000 r.u.

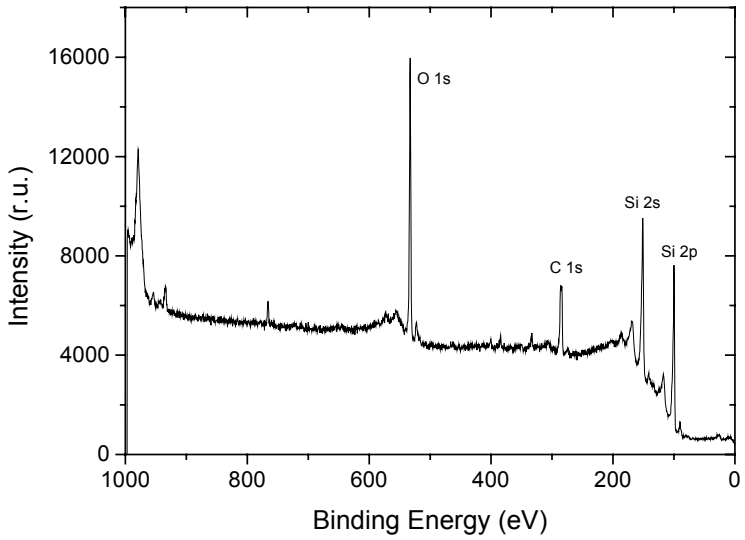

Fig. 8.4: XPS spectrum of a silicon film deposited from silylene diazide before argon sputtering.

The Fig. 8.5 shows a spectrum of the same film after 30 minutes of argon sputtering.

The argon sputtering eliminated part of the oxide film. The peak of oxygen (1s) has lower intensity, decreasing from 10000 r.u. to 3000 r.u.

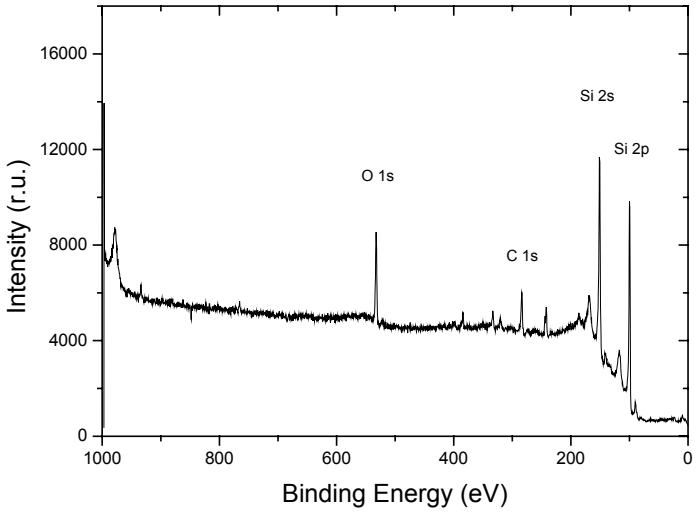

Fig. 8.5: XPS spectra of the silicon film deposited with silylene diazide after 30 minutes sputtering with argon.

A high resolution spectrum of the Si 2p peak around 100 eV is shown in Fig. 8.6. The broadening on the left side of the peak is characteristic for SiO_2.

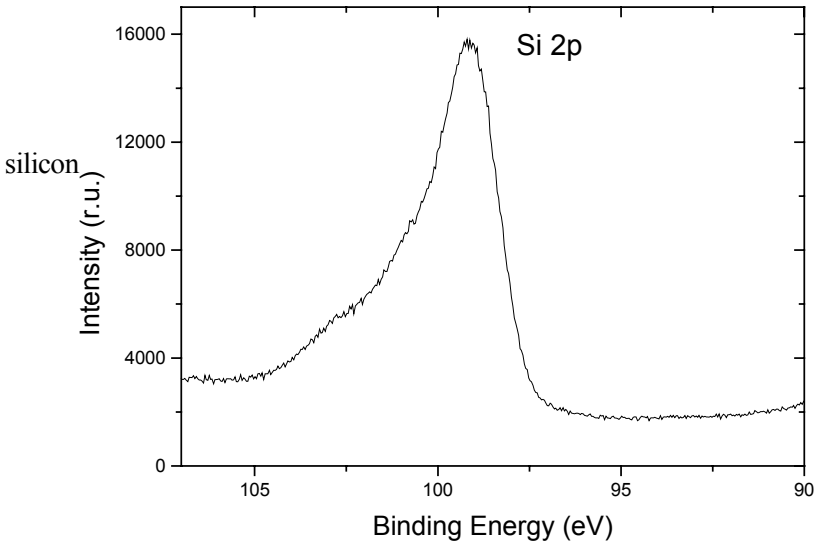

Fig. 8.6: XPS spectrum of the film growth with silylene diazide showing the Si 2p peak and the high energy SiO_x – satellites.

As shown in Fig. 8.7, the SiO_x satellites are removed after Ar sputtering.

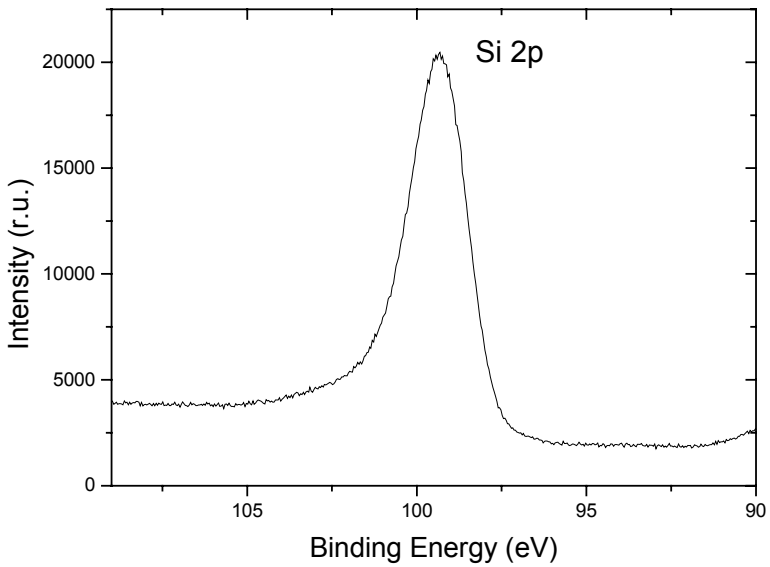

Fig. 8.7: XPS spectrum of Si 2p peak after 30 minute Ar sputtering.

Fig. 8.8 shows C 1s range of a film grown with silylene diazide before sputtering with argon. The spectrum shows characteristic peaks at 285 eV and at 283.3 eV.

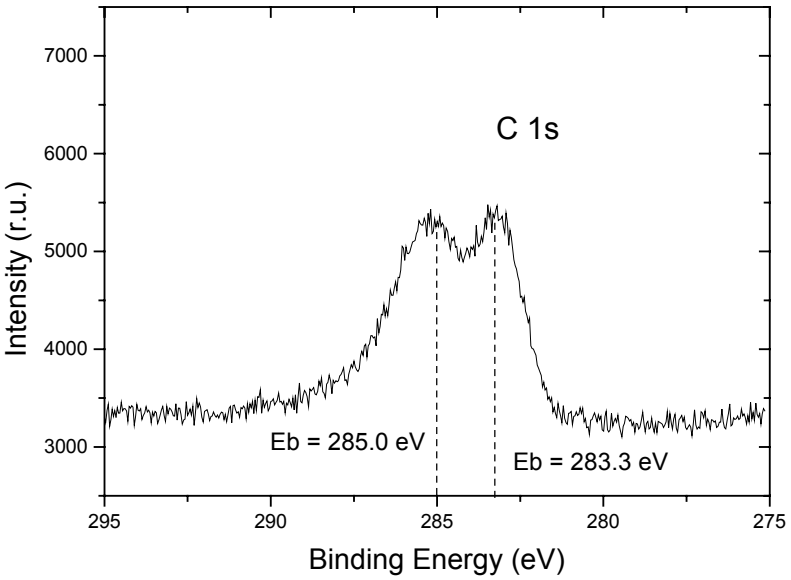

Fig. 8.8: XPS spectrum of a silicon film deposited showing two C 1s peak (285, 283.3) eV.

After sputtering with argon, the peak, at 285 eV disappeared indicating that traces of precursor became chemisorbed at the hot silicon sample. The energy of 283.3 eV represents a bond between carbon and silicon.

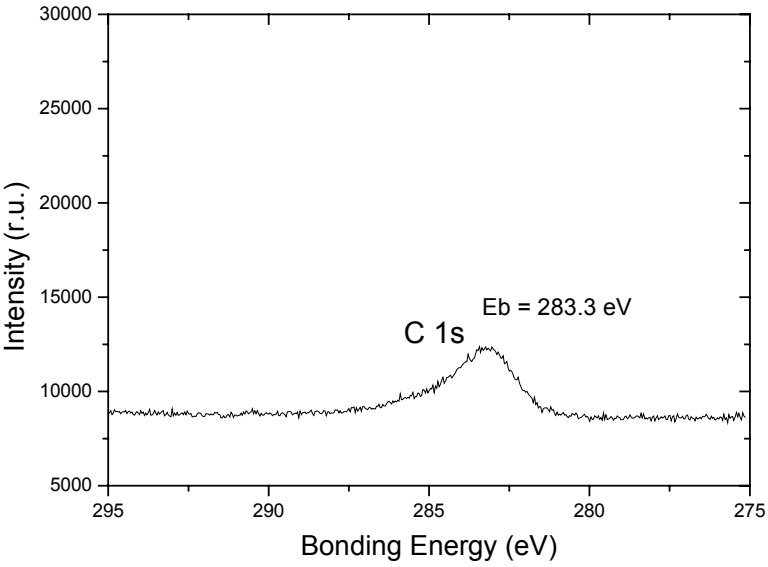

Fig. 8.9: XPS spectrum of a silicon film deposited showing the C 1s peak after 30 minute Ar sputtering.

8.6 X-ray Diffraction

The X-ray diffraction of the silicon layer grown using silylene diazide shows a mix of polycrystalline and amorphous phase. The diffractogram is shown in Fig. 8.10.

X-ray measurements were made using the detector scan mode to minimize the influence of the small sample thickness (0.39 µm).

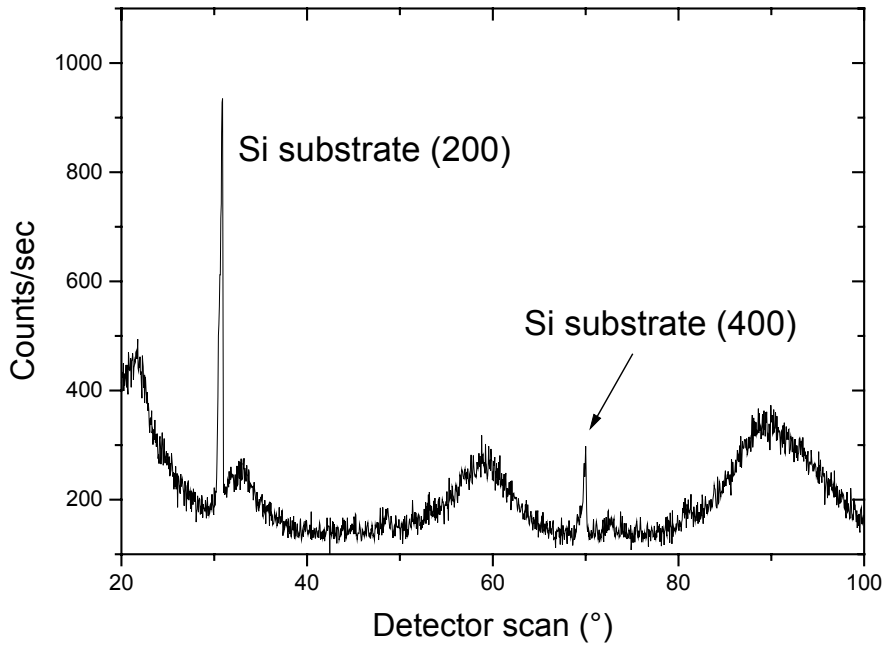

Fig. 8.10: X-ray diffractogram of the silicon film deposited with silylene diazide measured in the detector scan mode. The crystal orientation and amorphous phase are characterized by their typical peak positions.

The characteristics peaks and their corresponding crystalline orientation are shown in the According to this table, the peaks seen in Tab. 8.2 correspond to (111) and (400) orientation.

Crystalline orientation	Angle of Peak (°)
Si (111)	28.4
Si (200)	33.0
Si (311)	56.1
Si (400)	69.1
Si (422)	88.0
Si (511)	94.9

Tab. 8.2: Characteristic X-ray peaks of silicon.

8.7 EDX of the Silicon Film Deposited by Silylene Diazide

This technique gives information about the chemical composition of the film. The obtained spectrum is shown in Fig. 8.11. The resulting composition is:

99.63% silicon

0.28% carbon

0.09% oxygen.

This results are excellent and demonstrated the suitably of the silylene diazide precursor.

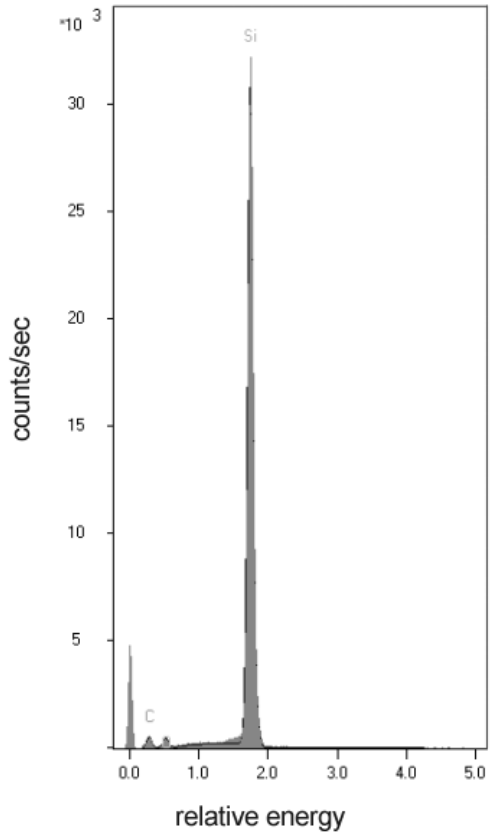

Fig. 8.11: EDX spectrum of the Si film deposited by silylene diazide.

9 Silylene Dihydride

9.1 Saturated Vapor Pressure

Between the three precursors investigated in this thesis, silylene dihydride has the highest saturated vapor pressure. For example, at a bubble temperature of 60°C, silylene diazide has a saturated vapor pressure of 0.11 mbar, whereas silylene dihydride at the same temperature, the vapor pressure is 2 mbar. The complete vapor pressure versus temperature profile is shown in Fig. 9.1.

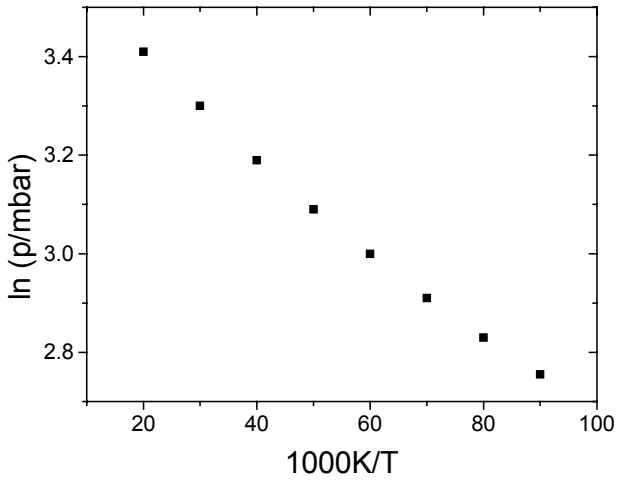

Fig. 9.1: Silylene dihydride vapor pressure versus temperature

As for the Z-diaminodisilyldisilene and silylene diazide, the vapor pressure increases exponentially temperature.

9.2 Concentration of Volatile Molecules in the Bubbler

Because of the higher concentration of molecules at lower temperatures with this precursor, deposition was successful. Fig. 9.2 shows the number of molecules of silylene dihydride in the gas phase as function of the temperature.

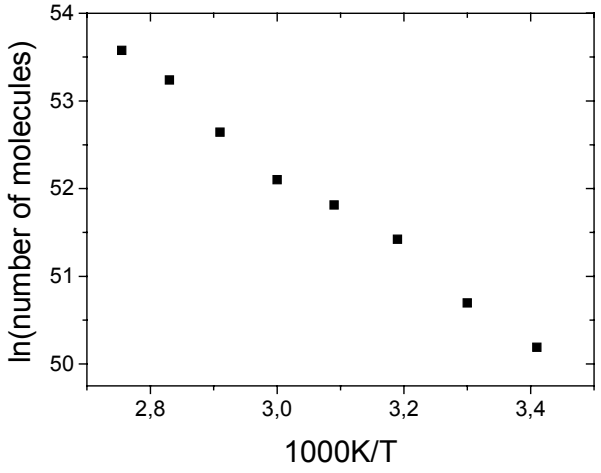

Fig. 9.2: Number of Silylene dihydride molecules versus temperature

The observed deposition rate as a function of substrate temperature is shown as on Arrhenius plot in Fig. 9.3.

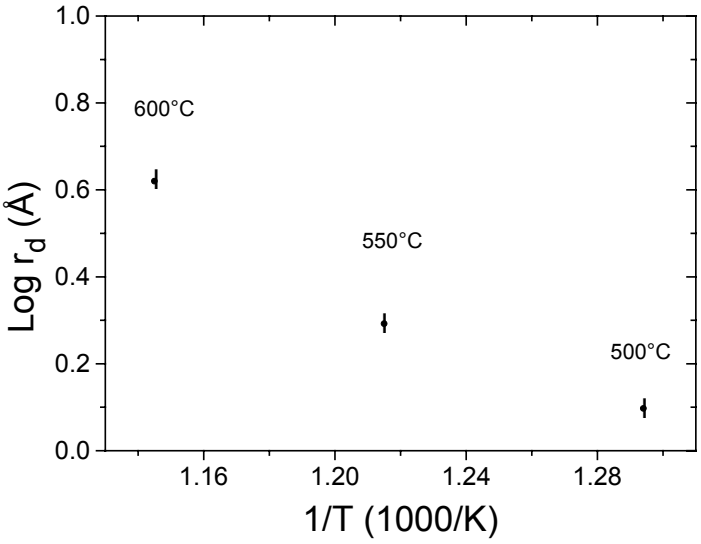

Fig. 9.3: Arrhenius Plot of the deposition rate versus the reciprocal substrate temperature.

Tab. 9.1 summarizes the pressure in the reactor, temperature of the bubbler, temperature of deposition in the reactor and deposition rate for the series of experiments.

Pressure (mbar)	Bubbler Temperature (°C)	Reactor Temperature (°C)	Deposition rate (Å/s)
1	90	500	0.93
2	90	500	1.39
5	90	500	0.80
1	90	550	1.11
2	90	550	1.39
5	90	550	1.96
1	90	600	1.88
2	90	600	1.94
5	90	600	2.06
10	90	600	2.55
10	90	650	2.90

Tab. 9.1: Deposition pressure, temperature of the bubbler, temperature of the reactor, and deposition rate for films deposited with silylene dihydride.

Growth starts at a temperature of 500°C. Experiments with a lower temperature confirmed the lack of deposition for all pressures concentrations of the precursor.

9.3 X-ray Photoelectron Spectroscopy of the Silicon Film

The peaks for Si 2s (151.2 eV), Si 2p (99.8 eV) and carbon C 1s (283.3 eV) are shown in the following Figures.

Fig. 9.4 shows a XPS spectrum of a silicon film produced with silylene dihydride and prior to argon sputtering. A gold reference was used to verify the position of the peaks and to calibrate the spectra. The peak of oxygen 1s has intensity 8000 r.u. before argon sputtering.

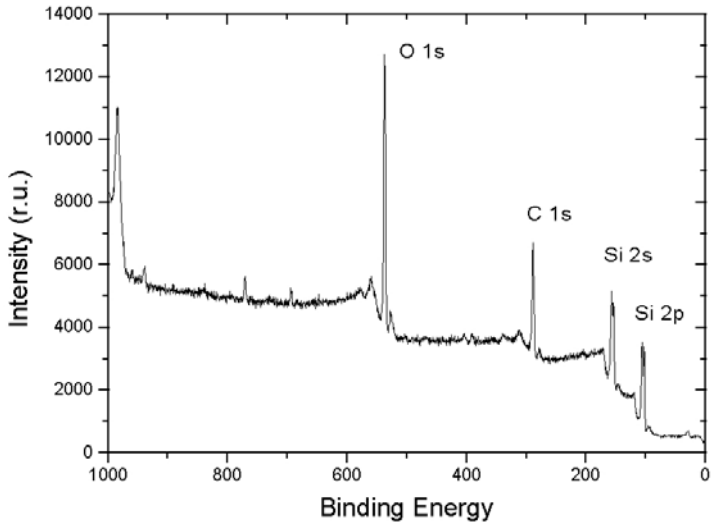

Fig. 9.4: XPS of the film deposited with silylene dihydride before argon sputtering.

Fig. 9.5 shows a spectrum of the same film after 30 minutes of argon sputtering. The silicon peak shows only carbon originated from the precursor. The peak of oxygen (1s) has lower intensity (5000 r.u.) and the silicon peaks have no oxide component.

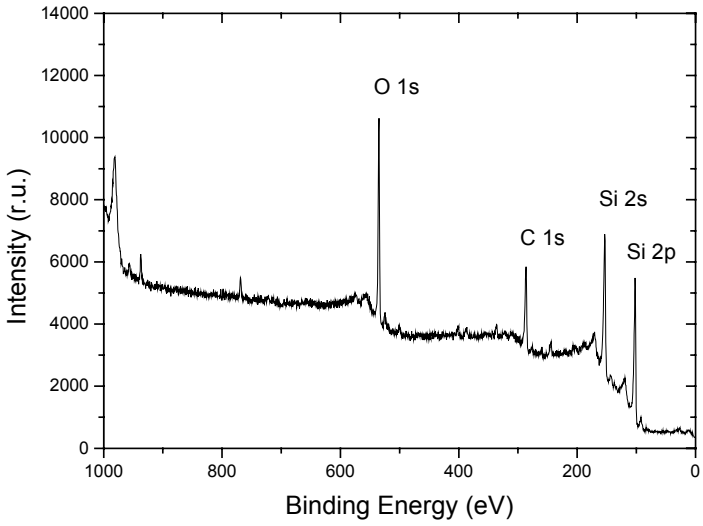

Fig. 9.5: XPS of the film deposited with Silylene dihydride after 30 minutes of argon sputtering

A high resolution spectrum of the Si 2p peak around 100 eV is show in Fig. 9.6. The second peak around 102 eV represents the native oxide.

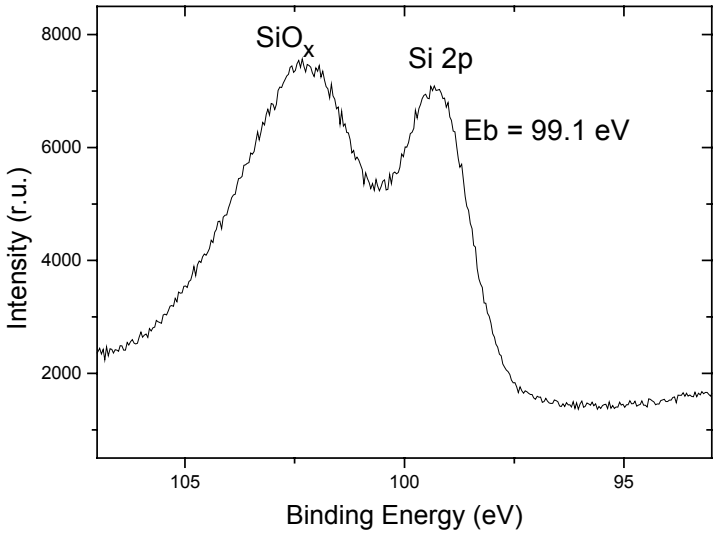

Fig. 9.6: XPS spectrum of the silicon film growth with silylene dihydride showing the Si 2p peak and the high energy SiO_x.

Silicon film grown with Silylene dihydride is similar as silicon film grown with silylene diazide, the high resolution spectrum of the Si 2p peak around 100 eV is shown in Fig. 9.9 with broadening on the left side of the peak characteristic for SiO_2.

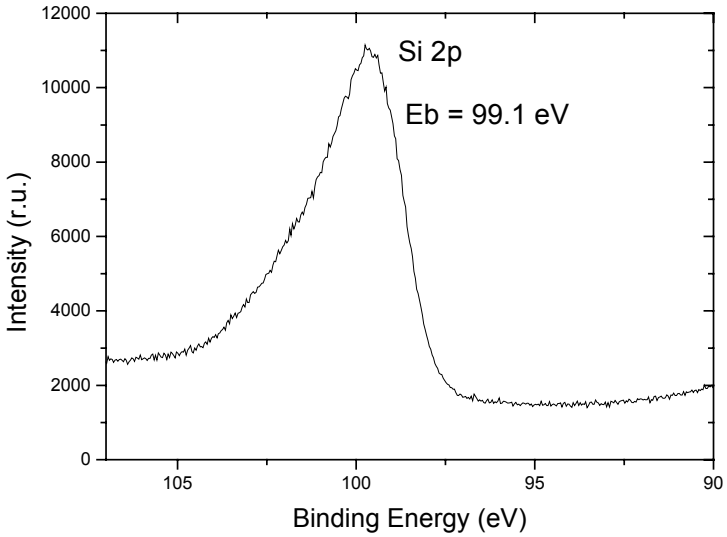

Fig. 9.7: XPS spectrum of the silicon film showing the Si 2p peak and the SiO_x satellites.

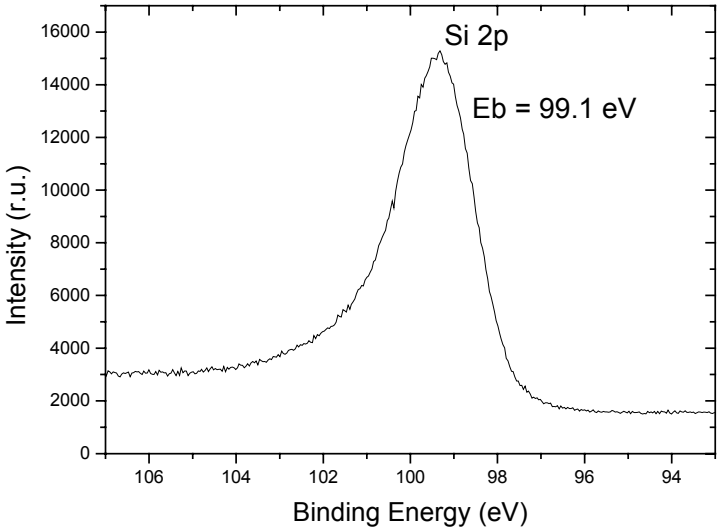

Fig. 9.8: XPS spectrum of Si 2p peak after 90 minute Ar sputtering.

The SiO_x are removed after Ar sputtering.

Fig. 9.9 shows C 1s range of a film grown with silylene dihydride. The peak corresponds to the characteristic energy of a carbon bonding (285 eV).

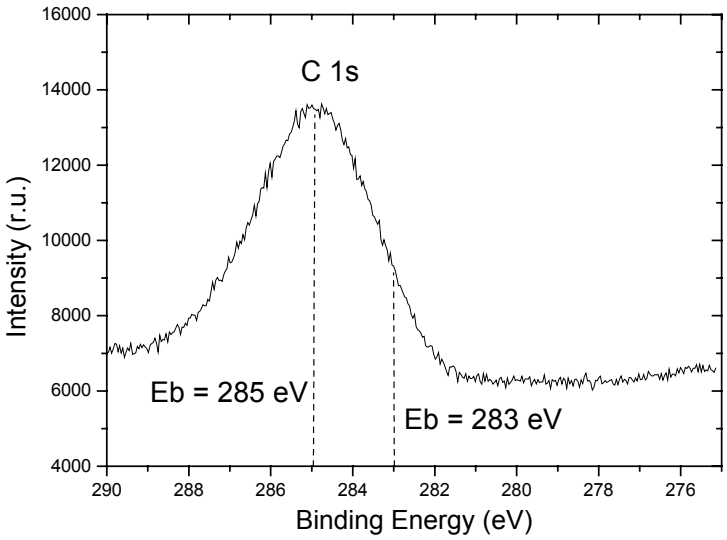

Fig. 9.9: XPS of a silicon film showing the C 1s characteristic peak with native oxide.

After sputtering with argon, the peak, at 285 eV disappeared indicating that became chemisorbed at the hot silicon sample. Process similar occurred in the silicon film deposited with silylene diazide, the silicon film deposited with silylene dihydride shows the same position for C1s. Fig. 9.10 shows the carbon component after 30 minutes of argon sputtering.

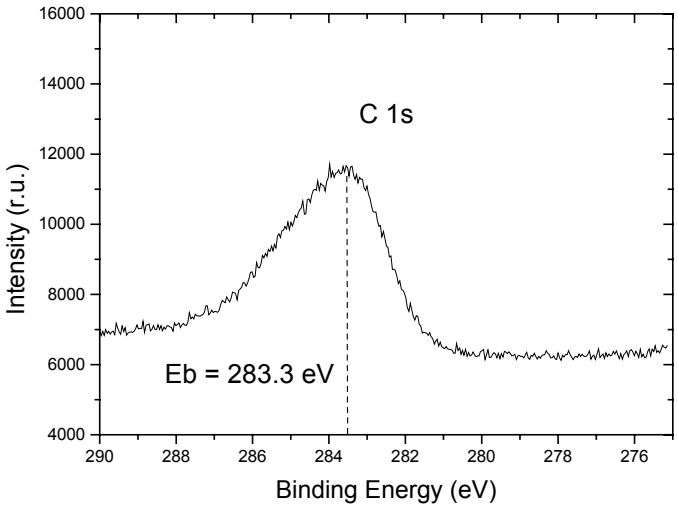

Fig. 9.10: XPS spectrum of a C 1s peak after 30 minutes argon sputtering.

Fig. 9.11 shows the C1s peak after 90 minutes argon sputtering.

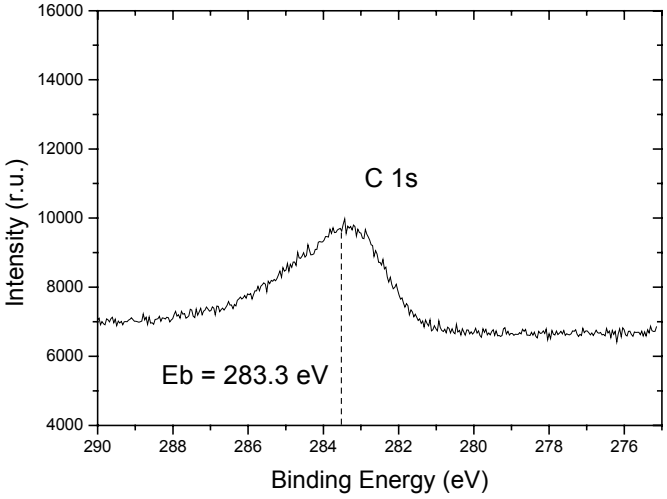

Fig. 9.11: XPS spectrum of a silicon film of the C 1s peak after 90 minute Ar sputtering.

9.4 Scanning Electron Microscopy

Fig. 9.12 shows the topography of the silicon film deposited from silylene dihydride. The picture illustrates a homogeneous and regular structure of the silicon film as the surface morphology acquired by SEM.

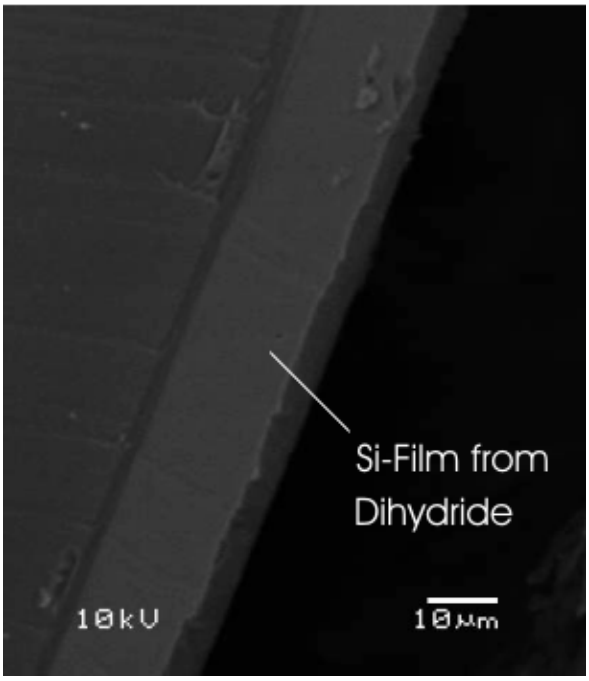

Fig. 9.12: Scanning Electron Micrograph of a silicon film deposited on silicon (100). (Magnification 1000, deposited under the following conditions: Temperature: 650°C, Pressure: 10 mbar, deposition rate: 2.90 Å/s, thickness: 15 µm.

Fig. 9.13 shows a cross-section of the silicon film. The homogeneity of the film and the good conformal coverage on the substrate surface show the high quality of this film.

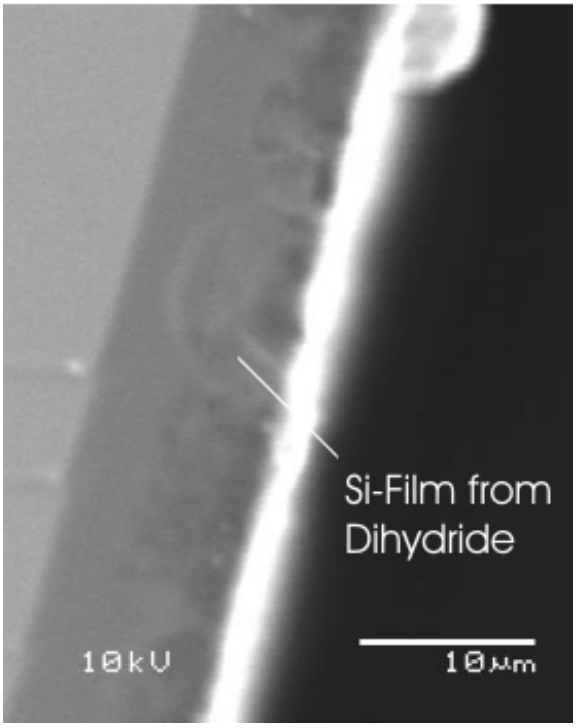

Fig. 9.13: Scanning Electron Micrograph of a silicon film deposited on silicon (100), magnification 1000, deposited under the following conditions: Temperature: 600°C, Pressure: 10 mbar, deposition rate: 2.55 Å/s, thickness: 14.7 µm

9.5 X-ray Diffractogram of Films from Silylene Dihydride

From X-ray diffraction of the layer deposited by using silylene dihydride, the results obtained indicated a predominantly polycrystalline film with some amorphous characteristics, similar to the silicon film deposited from silylene diazide and shown in Fig. 9.14.

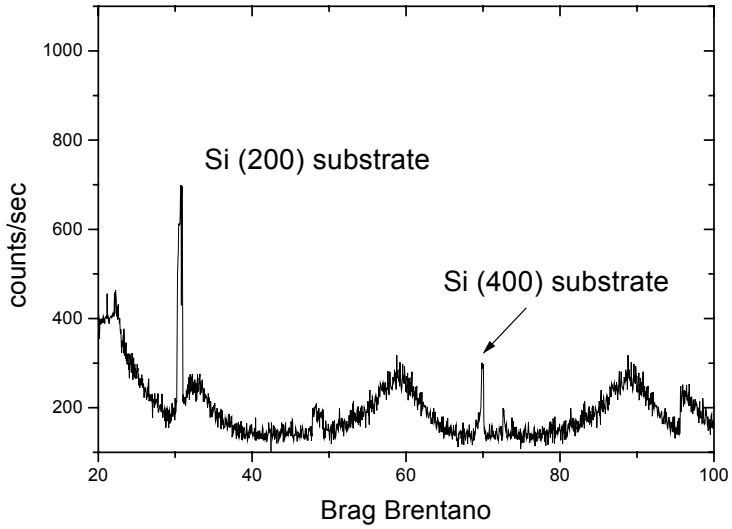

Fig. 9.14: X-ray Diffractogram of the silicon film grown with silylene dihydride measured in the Brag Brentano mode. The crystal orientation are characterized by their typical peak positions and was similar the Si film grown with silylene diazide.

9.6 EDX of the Silicon Film Deposited by Silylene Dihydride

The chemical composition of the film shown in Fig. 9.15 shown:

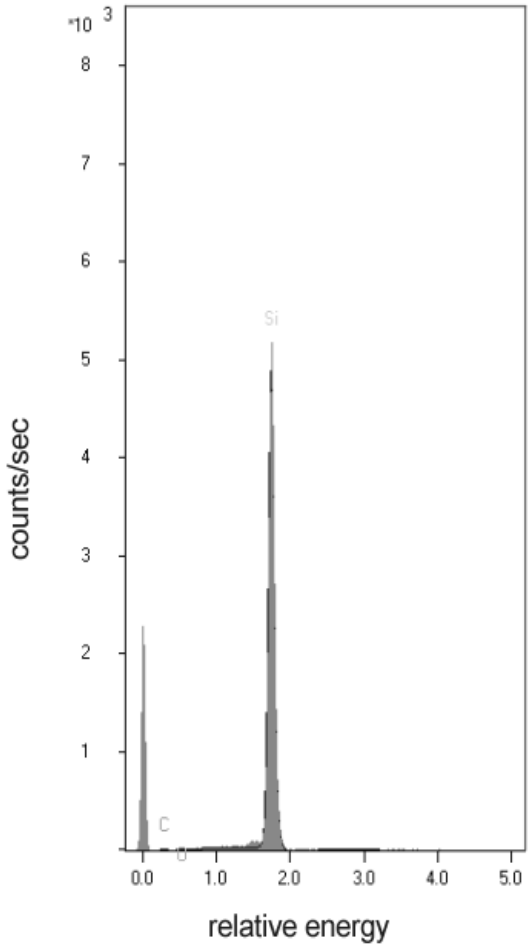

99.85% silicon

0.08% carbon

0.07% oxygen.

Fig. 9.15: EDX spectrum of a silicon film deposited with silylene dihydride

10 Discussion and Conclusion of Part II

In this work the silicon growth on a silicon wafer via OMCVD with silylene diazide and silylene dihydride was realized with success. Furthermore, no film deposition was observed on quartz, metals and oxides showing that these precursors have the big advantage of growth selectivity on Si.

The silylene diazide contains the elements Si, C, N and H in the proportions of 1:10:8:22. The possible reaction mechanism of the silylene diazide is shown in Fig. 10.1 predicted from the stability of the products.

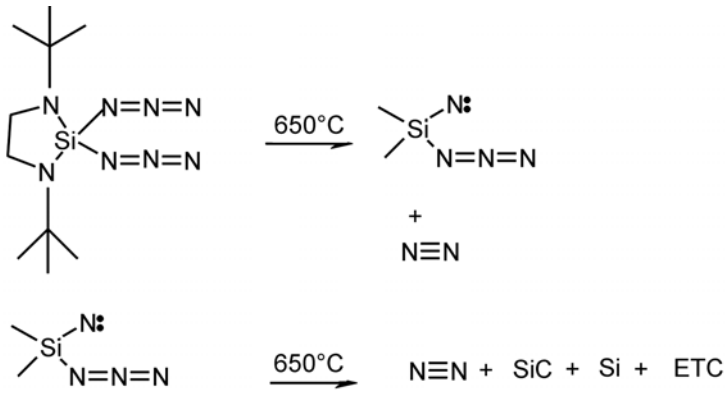

Fig. 10.1: Possible mechanism for silylene diazide.

The silylene dihydride contains the elements Si, C, N and H in the proportions of 1:10:2:24. The possible reaction of the silylene dihydride is shown in Fig. 10.2.

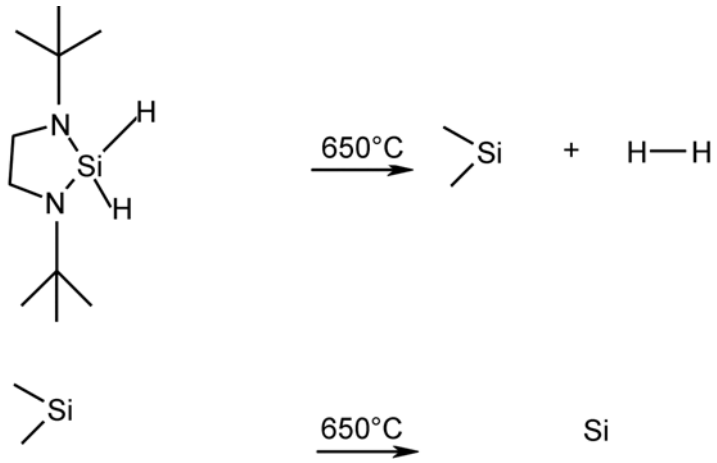

Fig. 10.2: Possible reaction mechanism for silylene dihydride, showing the rupture from the azide group followed by decomposition.

Comparing the single source precursors, the deposition rate of silylene dihydride of 2.55 Å/s at 600 °C is much higher than the deposition rate of silylene diazide of 0.27 Å/s. The saturated vapor pressure at a specific bubbler temperature increases in the following sequence: $p_{\text{Silylene diazide}} < p_{\text{Z-diaminodisilyldisilene}} < p_{\text{silylene dihydride}}$. So, the temperature needed for the evaporation process is the lowest for silylene dihydride. The thermal decomposition of these new precursors in a long time scale has still to be investigated.

The activation energy in Tab. 10.1 was calculated and confirms the properties of the precursors as discussed above. The silylene diazide presents the highest activation energy value followed by the z-diaminodisilyldisilene and the silylene dihydride, consecutively.

Precursor	Activation Energy (KJ/mol)
Z-diaminodisilyldisilene	11.1 (theoretical)
Silylene Diazide	22.5 (experimental)
Silylene Dihydride	6.2 (experimental)

Tab. 10.1: Activation energies of the silylene-based precursors

The reaction of the precursor Z-diaminodisilyldisilene with the Si substrate was experimented in both used reactors. Also with a high flux of diaminodisilyldisilene no reaction occurred at the Si substrate in the temperature range from 100° C to 650° C. The monomeric form of Z-diaminodisilyldisilene recognized by its transparent color is very instable and it turns back to the red polymeric form inside the reactor before reaching the Si substrate.

More successful was the growth with the silylene precursors. The preferential orientations of the Si crystals obtained were investigated by X-ray diffraction. Using the precursor silylene diazide, the preferential orientations of the Si crystals were Si(200), Si(311) and Si(422); using the precursor silylene dihydride, the preferential orientations were Si(200), Si(311), Si(422) and Si(511).

The analysis of the film morphology using scanning electron microscopy shows silicon islands after the deposition with both silylene precursors. These characteristic islands were also observed in the case of germanium growth on Si with an analogue precursor: germylene [Ve 96]. The main difference between precursors with Ge and Si is the activation energy, which is higher for silicon than for germanium [Gl 93], [Pr 95]. The germylene molecule has the same structure of the silylene with a Ge atom in place of the Si atom. Germylene is also surface selective and grows not on SiO_2. The analysis with SEM shows Si islands with diameter of 0.2 µm (Fig. 8.3). Nucleation starts at relatively few sites on the Si surface and only upon further growth a compact film is formed. The experiments showed that the presence of native oxides on the Si surface prevents the crystal nucleation.

To grow Si, the optimal substrate temperature with silylene diazide was 650 °C and with silylene dihydride 500 °C. These temperatures are higher than using precursors based on Ge. No nucleation of Si sites with silylene precursors were observed by SEM at temperatures between 100 °C and 400 °C (pressures: 0.5 – 1.0 mbar, growth time: 30 - 240 minutes, two different types of reactors). The composition of the film surfaces grown with both silylene precursors was analyzed by XPS and predominantly showed the presence of Si, but also amounts of oxygen, as an oxidation product of the Si, and C, residual from the precursor was

measured. Sputtering the surface with argon reduced the amount of O and C drastically, showing that mainly the surface of the films was contaminated. Examining the films by EDX a Si concentration of 99 % and a low quantity of C (about 0.3 %) were found. Even present in the precursors, nitrogen was not detected in the films indicating that our growth conditions prevent the formation of SiN and similar compounds. N cracked from the silylene molecules is just pumped out of the growth system.

Future research has to be done with these new precursors to better characterize its chemical and physical properties. This would be required for the possible application of these selective and safe precursors in the Si-devices industry. The growth on already structured surfaces is also an interesting approach for further investigation.

11 Figure index

12 Table index

13 References

[Ac 1892] E.G. Achson, Brit. Pat. 17 (1892) 911.

[Ad 59] R.F. Adamski, K.M. Merz, Kristallografiya 111 (1959) 350.

[Ad 84] A. Addamiano, J.A. Sprague, Appl. Phys. Lett. 44 (1984) 525.

[Al 71] Yu.M. Altaiskii, I.M. Zaritskii, V.Ya. Zevin, A.A. Konchits, Sov.Phys.Solid State 12(1971)2453.

[Al 93] M.D. Allendorf, C.F. Mellius, J. Phys. Chem. 97 [1993] 720.

[Al 93a] M.D. Allendorf, T.H. Osterheld, C.F. Melius, Sandia Report SAND94-8524.UC-361 (1993).

[Ar 93] A. Arbab, A. Spetz, Q. Wahab, M. Wilander, I. Sundstrom, Sensors and Materials 4(1993)173.

[Ba 69] R.B. Bartlett, R.A. Mueller, Mat. Res. Bull. 4 (1969)341.

[Ba 95] B.J. Baliga, Inst.Phys.Conf.Ser.No. 142, Proceedings of the Sixth International Conference on Silicon Carbide and Related Materials (1995), Kyoto, Japan, edited by S. Nakashima, H. Matsunami, S. Yoshida, H. Harima, 1.

[Be 92] T.M. Besmann, B.W. Sheldon, T.S. Moss, M.D. Kaster, J.Am.Ceram. Soc. 75(1992) 2899.[Be 92a] V.M. Bermudez, Surf.Sci. 276(1992)59.

[Bh 93] M. Bhatnagar, B.J. Baliga, IEEE Trans. Electron Devices 40(1993)645.

[Bo 69] D.H. Bolt, J. Phys. Chem. Solids 30 (1969) 1297.

[Bo 85] F. Boszo, J.T. Yates, W.J. Choyke, L. Muelhof, J. Appl. Phys. 57 (1985) 2771.

[Br 69] R.W. Brander, R.P. Sutton, Br.J. Appl. Phys. 2 (1969) 309.

[Br 95] C.D. Brandt, A.K. Agarwal, G. Augustine, R.R. Baron, A.A. Burk Jr., R.C. Clarke, R.C. Glass, H.M. Hobgood, A.W. Morse, L.B. Rowland, S. Seshadri, R.R. Siergij, T.J. Smith, S. Sriram, M.C. Driver, R.H. Hopkins, Inst. Phys. Conf. Ser. No.142, Proceedings of the Sixth International Conference on Silicon Carbide and Related Materials (1995), Kyoto, Japan, edited by S. Nakashima, H. Matsunami, S. Yoshida, H. Harina, 659.

[Ca 66] R.B. Campbell, T.C. Chu, J. Electrochem. Soc. 113 (1966) 825.

[Ca 70] B.S. Cartwright, P. Popper, Science of Ceramics (1970) 473.

[Ca 01] C.H. Carter Jr., R. Glass, M. Brady, D. Malta, D. Henshall, S. Müller, V. Tsvetkov, D. Hobgood and A. Powell. Material Science Forum Vols. 353-356(2001) pp. 3-6.

[Ch 62] W.J. Choyke, L. Patrick, Phys.Rev. 127(1962)1868.

[Ch 64] W.J. Choyke, D.R. Hamilton, L. Patrick, Phys. Rev A 133(1964) 1163.

[Ch 87] D.J. Cheng, W.J. Shyy, D.H. Kuo, M.H. Hon, J. Electrochem. Soc. 134 (1987) 3145.

[Ch 87b] C. Cheng, R.J. Needs, V. Heine, N. Churcher, Europhys.Lett. 3(1987)475.

[Ch 88] C. Cheng, R.J. Needs, V. Heine, J. Phys. Chem. 21(1988) 1049.

[Ch 88a] W.J. Choyke, Z.C. Feng, J.A. Powell, J.Appl.Phys. 64(1988)3163.

[Ch 89] M.I. Chaudhry, J.Mater.Res. 4(1989)404.

[Ch 89a] M.I. Chaudhry, W.B. Berry, J.Mater.Res. 4(1989)1491.

[Ch 90] M.I. Chaudhry, R.L. Wright, J. Mater. Res. 5 (1990) 1595.

[Ch 90] L.Chen, T. Goto, T. Hirai, Jornal of Materials Science 25, 4273. Institute for Materials Research, Tohoku University, Sendai 980, Japan (1990)

[Ch 93] C.C. Chiu, S.B. Desu, C.Y. Tsai, J. Mat. Res. 8 (1993) 2617.

[Ch 95] C.C. Chiu, S.B. Desu, G. Chen, C.Y. Tsai, W.T. Reynolds, J.Mat. Res. 5(1995) 1099.

[Ch 95a] J.S. Chen, A. Bächli, M.A. Nicholet, L. Baud, C. Jaussaud, R. Madar, Mat.Science Engineering B29(1995)185.

[Cl 92] R.C. Clarke, T.W. O'Keefe. P.G. McMullin, T.J. Smith, S. Sriram, D.L. Barett, 50th Annual Device Research Conf., Cambridge, MA, USA, 22-24 Juni 1992, Abstract VA-5.

[Cl 01] T. Cloitre, N. Moreaud, P. Vicente, M.L. Sadowsk and R.L. Aulombard, Material Science Forum Vols. 353-356(2001) pp. 159-162.

[Da 65] R. Dalven, J. Phys. Chem. Solids 26(1965) 439.

[Da 66] T.C. Damen, S.P.S. Porto, B. Tell, Phys.Rev. 142(1966)570.

[Da 91] R.F. Davis, G. Kelner, M. Shur, J.W. Palmour, J.A. Edmond, Proc.IEEE 79(1991)677.

[Da 92] R.F. Davis, Physica B 185 (1992) 1.

[Da 01] Ö. Danielsson, U. Forsberg, A. Henry and E. Janzen, Materials Science Forum Vols. 353-356 (2001) pp. 99-102

[De 77] P.J. Dean, W.J. Choyke, L.Patrick, J.Lumin. 15(1977) 299.

[Dm 85] V.A. Dmitriev, P.A. Ivanov, I.V. Korkin, Ya.V. Morozenko, I.V. Popov, T.A. Sidorova, A.M. Strel'chuck, V.E. Chelnokov, Soviet Tech. Phys. Lett. 11 (1985) 98.

[Dm 92] V.A. Dmitriev, L.B. Elfimov, N.D. Il'inskaya, S.V. Redakova, Springer Proc. Phys. 56(1992)307.

[Dm 93] V.A. Dmitriev, V.E. Chelnokov, J. Cryst. Growth 128(1993)343.

[Do 85] S.Dohmae, K. Shibahara, S. Nishino, H. Matsunami, Jpn.J.Appl.Phys. 24(1985)L873.

[Ed 88] J.A. Edmond, K. Das, R.F. Davis, J.Appl.Phys. 63(1988)922.

[El 67] B. Ellis, T.S. Moss, Proc. R. Soc. Lond. A[UK] 299(1967) 383.

[Ep 94] Epichem Limited, Power Road, Bromborough Wirral, Merseyside L62 3QF, United Kington (1994).

[Fe 68] D.W. Feldman, J.H. Parker Jr., W.J. Choyke, L. Patrick, Phys.Rev. 173(1968)787.

[Fe 88] Z.C. Feng, A.J. Mascarenhas, W.J. Choyke, J.A. Powell, J.Appl.Phys. 64(6)(1988)3176.

[Fe 88a] Z.C. Feng, W.J. Choyke, J.A. Powell, J.Appl.Phys. 64(12)(1988)6827.

[Fe 95] Z.C. Feng, C.C. Tin, R. Hu, J. Willians, Thin Solid Films 266(1995)1.

[Fi 95] A. Fissel, B. Schröter, W. Richter, Appl.Phys.Lett.66(1995)3182.

[Fr 51] F.C. Frank, Phil. Mag. 42 (1951) 1014.

[Fu 88] Y. Furumura, M. Doki, F. Mieno, T. Eshita, T. Suzuki, M. Maeda, J. Electrochem.Soc. 135(1988)1255.

[Gl 93] F. Glatz, Dissertation, Technical University of Munich, (1993).

[Gm 86] Gmhlin, Handbook of Inorganic Chemistry, Si Supplement B3 SiC Part 2 8th Edition, Springer Verlag Berlin, Heidelberg, New York, Tokio (1986).

[Go 92] I. Golecki, F. Reidinger, J. Marti, Appl. Phys. Lett. 60 (1992) 1703.

[Go 94] J.S. Golea, L.E. Burns, R.L. Taylor, Appl. Phys. Lett. 64(1994) 131.

[Ha 95] G.L. Harris, H.S. Henry, A. Jackson, Properties of Silicon Carbide, edited by G.L. Harris, EMIS Datareviews Series No. 13(1995) 63.

[He 91] V. Heine, C. Cheng, R.J. Needs, J. Am. Ceram. Soc. 74(1991) 2630.

[He 93] F. Henry, P. Marti, Y. Casaux, C. Combescure, A. Figueras, V. Madigou, R. Rodriguez-Clemente, A. Mazel, J. Sevely, B. Armas, Journal De Physique IV 3(1993) 329.

[Hi 93] M.L.Hitchman, K.F. Jensen, Chemical Vapor Deposition, Principles and Applications, (1993).

[Hi 95] M. Hirai, M. Miyatake, M. Kusuka, M. Iwami, Inst. Phys.Conf.Ser.No.142, Proceedings of the Sixth International Conference on Silicon Carbide and Related Materials (1995), Kyoto, Japan, edited by S. Nakashima, H. Matsunami, S. Yoshida, H. Harima, 1043.

[Ho 82] L. Hoffman, D. Ziegler, D. Theis, C. Weyrich, J. Appl. Phys. 53 (1982) 6962.

[Ho 94] H.M. Hobgood, D.L. Barett, J.P. McHugh, R.C. Clarke, S. Siram, A.A. Burk, J. Greggi, C.D. Brandt, R.H. Hopkins, W.J. Choyke, J. Cryst. Growth 137 (1994) 181.

[Ho 95] D. Hofmann, S. Yu. Karpov, Yu. N. Makarov, E.N. Morkhov, M.G. Ramm, M.S. Ramm, A.D. Roenkov, Yu.A. Vodakov Inst. Phys. Conf. Ser. No. 142, Proceedings of the Sixth International Conference on Silicon Carbide and Related Materials (1995), Kyoto, Japan, edited by S. Nakashima, H. Matsunami, S. Yoshida, H. Harima, 29.

[Ho 98] J. Hofmann, Dissertation, Technische Universität München, (1998).

[Hu 95] G.W. Hunter, P.G. Neudeck, L. Chen, D. Knight, C.C. Liu, Q.H. Wu, Inst.Phys.Conf.Ser.No. 142, Proceedings of the Sixth International Conference on Silicon Carbide and Related Materials (1995), Kyoto, Japan, edited by S. Nakashima, H. Matsunami, S. Yoshida, H. Harima, 817.

[Ik 91] K. Ikoma, M. Yamanaka, H. Yamaguchi, Y. Shichi, J. Electrochem. Soc. 138 (1991) 3028.

[Iw 88] M. Iwami, M. Kusaka, M. Hirai, H. Nakamura, K. Shibahara, H. Matsunami, Surf. Sci. 199 (1988) 467.

[Ja 54] H. Jagodzinski, N.J. Min. Monatsh 3(1954) 209.

[Ja 71] K.A. Jacobson, J. Electrochem. Soc. 118 (1971) 127.

[Ja 95] E. Janzen, O. Kordina, Inst. Phys. Conf. Ser. No. 142, Proceedings of the Sixth International Conference on Silicon Carbide and Related Materials (1995), Kyoto, Japan, edited by S. Nakashima, H. Matsunami, S. Yoshida, H. Harima, 653.

[Je 83] N.W. Jeeps, T.F. Page, Prog. Cryst. Growth Charact. 7(1983) 259.

[Ji 93] X. Jiang, Appl. Phys. Lett 62 (1993) 3438.

[Jo 65] E.O. Johnson, RCA Rev. 26 (1965) 163.

[Ka 70] C.J. Kapteyns, W.F. Knippenberg, J. Cyst. Growth 7 (1970) 20.

[Ka 95] K. Kamimura, T. Miwa, T. Sugiyama, T. Ogawa, M. Nakao, Y. Onuma, Inst.Phys.Conf.Ser.No. 142, Proceedings of the Sixth International Conference on Silicon Carbide and Related Materials (1995), Kyoto, Japan, edited by S. Nakashima, H. Matsunami, S. Yoshida, H. Harima, 825.

[Ke 70] W. Kern, D.A. Puotinen, RCA Rev. 31(1970)187.

[Ke 72] R.W. Keyes, Proc. IEEE 60 (1972) 225.

[Ke 89] G. Kelner, M. Shur, S. Binari, K. Sleger, H.S. Kong, IEEE Trans.Electron Devices 36(1989)1045.

[Ki 86] H.J. Kim, R.F. Davis, J.Electrochem.Soc. 133(1986)2351.

[Kn 63] W.F. Knippenberg, Philips Res. Rep. 18 (1963) 229.

[Ko 75] F. Kobayashi, K. Ikawa, K. Iwamoto, J. Cryst. Growth 28 (1975) 395.

[Ko 88] H.S. Kong, Y.C. Wang, J.T. Glass, R.F. Davis, J. Mater. Res. 3 (1988) 521.

[Ko 93] J. Kono, Physica B 184(1993) 178.

[Ko 94] T. Kodas, M. Hampden-Smith, The Chemistry of Metal CVD, (1994).

[Ko 95] O. Kordina, L.O. Björketun, A. Henry, C. Hallin, R.C. Glass, L. Hultman, J.E. Sundgren, E. Janzen, J. Cryst. Growth 154 (1995) 303.

[Kr 95] G. Krötz, CH. Wagner, W.Legner, H. Sonntag, H. Möller, G. Müller, Inst. Phys. Conf. Ser. No. 142, Proceedings of the Sixth International Conference on Silicon Carbide and Related Materials (1995) Kyoto, Japan, edited by S. Nakashima, H. Matsunami, S. Yioshida, H. Harima, 829.

[Kr 95a] G. Krötz, W. Legner, G. Müller, H.W. Grueninger, L. Smith, B. Leese, A. Jones, S.Rushworth, Mat.Sci.Eng. B29(1995)154.

[Ku 90] D.H. Kuo, D.J. Cheng, W.J. Shyy, M.H. Hon, J. Electrochem. Soc. 137 (1990) 3688.

[Ku 93] T. Kunstmann, Diplomarbeit TU München, (1993).

[Ku 95] Th. Kunstmann, H. Angerer, J. Knecht, S. Veprek, N.W. Mitzel, H. Schmidbaur, Chemistry of Materials 7 (1995) 1675.

[Ku 96] T. Kunstmann, Darstellung und Charakterisierung Epitaktischer 3C-SiC Schichten auf Si[100] Substraten, Dissertation, TU München (1996).

[La 81] Y. Laukhe, Y.M. Tairov, V.F. Tsvetkov, F. Schepanski, Sov.Inorg.Mater. 17(1981)177.

[Le 55] J.A. Lely, Ber. Dtsch. Keram. Ges. 32 (1955) 229.

[Le 70] A.J. Learn, I.H. Khan, Thin Solid Films 5(1970)145.

[Le 01] A.A. Lebedev, N.B. Strokan, A.M. Ivanov, D.V. Davydov and V.V. Kozlovskii. Materials Science Forum Vols. 353-356 (2001) pp. 747-752.

[Li 84] H.P. Liaw, R.F. Davis, J. Electrochem. Soc. 131(1984)3014.

[Li 85] H.P. Liaw, R.F. Davis, J. Electrochem. Soc. 132 (1985) 642.

[Li 95] J. Li, A.J. Steckl, J. Electrochem. Soc. 142 (1995) 634.

[Lu 93] B.P. Luther, J. Ruzyllo, D.L. Miller, Appl.Phys.Lett. 63(1993)171.

[Ma 75] H. Matsunami, S. Nishino, S. Odaka, T. Tanaka, J. Crystl. Growth 31 (1975) 72.

[Ma 78] H. Matsuname, S. Nishino, T. Tanaka, J. Crystl. Growth 45 (1978) 138.

[Me 92] A.V. Nelnichok, Yu. A. Psaechnik, Sov. Phys. Solid State 34 (1992)227.

[Mi 84] T. Miyazawa, S. Yoshida, S. Misawa, S. Gonda, Appl.Phys.Lett. 45(1884)380.

[Mo 74] C.J. Mogab, H.J. Leamy, J. Appl. Phys. 45 (1974) 1075.

[Mo 90] S. Motojima, M. Hasegawa, Thin Solid Films 186 (1990) L39.

[Mo 92] E.N. Morkhov, M.G. Ramm, Yu.A. Vodakov, High Purity Substances 3 (1992) 98.

[Mo 93] W.J. Moore, P.J. Lin-Chung, J.A. Freitas Jr., Y.M. Altaiskii, V.L. Zuev, L.M. Ivanova, Phys.Rev. 48(1993)12889.

[Mo 94] H.Morkoc, S. Strite, G.B. Goa, M.E. Lin, B. Sverdlov, M. Burns, J. Appl. Phys. 76(1994)1363.

[Mü 76] W.v. Münch, I. Pfaffeneder, Thin Solid Films 31 (1976) 39.

[Mü 77] W.v. Münch, J. Electron. Mater. 6 (1977)449.

[Mü 78] W.V. Münch, E. Pettenpaul, J. Electrochem. Soc. 125 (1978) 1129.

[Mü 96] W.v. Münch, U. Ruhnau, J. Cryst. Growth 158 (1996) 491.

[Na 89] T. Nakata, K. Koga, Y. Matsushita, Y. Ueda, T. Niina, Springer Proc. Phys. 43 (1989) 26.

[Ne 86] J.N.Ness, T.F. Bull. Mineral. 109(1986)151.

[Ne 96] P.G. Neudeck, D.J. Larkin, J.A. Powell, Internetartikell vom 17.4.1996, NASA Lewis Research Certer, 21000 Brookpark Road, Cleveland, OH 44135, USA(1996).[Ne 86] J.N. Ness, T.F. Page, Bull. Mineral. 109 (1986) 151.

[Ng 92] T.H. Nguyen, M.M. Carrabba, T.D. Plante, R.D. Rauh, Ext.Abstr.Electrochem.Soc. 92(1992)474.

[Ni 75] S. Nishino, H. Matsunami, T. Tanaka, Jpn. J. Appl. Phys. 14(1975) 1833.

[Ni 78] S. Nishino, H. Matsunami, T. Tanaka, J. Cryst. Growth 45 [1978] 144.

[Ni 80] S. Nishino, Y. Hazuki, H. Matsunami, T. Tanaka, J. Electrochem.Soc. 127(1980)2674.

[Ni 83] S. Nishino, J.A. Powell, H.A. Will, Appl. Phys. Lett. 42 (1983) 124.

[Ni 87] S. Nishino, H. Suhura, H.Ono, H. Matsunami, J. Appl. Phys. 61 (1987) 4889.

[Ni 89] S. Nishino, J. Saraie, Springer Proceedings in Physics 34 (1989) 45.

[Ni 95] K. Nishino, T. Kimoto, H. Matsunami, Inst. Phys. Conf. Ser. No. 142, Proceedings of the Sixth International Conference on Silicon Carbide and Related Materials (1995),

Kyoto, Japan, edited by S. Nakashima, H. Matsunami, S. Yoshida, H. Harima, 89.R.B. Bartlett, R.A. Muller, Mat. Res. Bull. 4 (1969) 341.

[No 95] N. Nordell, S. Nishino, J.W. Yang, C. Jacob, P. Pirouz, J. Electrochem Soc. 142 (1995) 565.

[Nu 85] S.R. Nutt, F.E. Wawner, J. Mater. Sci. 20(1985) 1953.

[Nu 87] S.R. Nutt, D.J. Smith, H.J. Kim, R.F. Davis, Appl. Phys. Lett. 50 (1987) 203.

[Oh 95] Y. Ohshita, J. Electrochem. Soc. 142 (1995) 1002.

[Ok 87] H. Okumura, E. Sakuma, J.H. Lee, H. Mukaida, S. Misawa, K. Endo, S. Yoshida, J.Appl.Phys. 61(3)(1987)1134.

[Ok 88] H. Okumura, Jpn.J.Appl.Phys. 27(1988)1712.

[Ol 82] D. Olego, M. Cardona, P.Vogl, Phys.Rev. B25(6)(1982)3878.

[Ol 82a] D. Olego, M. Cardona, Phys.Rev. B25(1982)1151.

[Pa 58] L.J. van der Pauw, Philips Res.Rep. 13(1958)1.

[Pa 63] L. Patrick, D.R. Hamilton, W.J. Choyke, Phys.Rev. 132 (1963)2023.

[Pa 66] L. Patrick, D.R. Hamilton, W.J.Choyke, Phys. Rev. 143 (1966) 526.

[Pa 69] L. Patrick, W.J. Choyke, Phys. Rev. 186(1969) 775.

[Pa 70] L. Patrick, W.J. Choyke, Phys. Rev. B2 (1970) 2255.

[Pa 75] D. Panday, P. Krishna, J. Cryst. Growth 31 (1975) 66.

[Pa 83] D. Panday, P. Krishna, Prog. Cryst. Growth Charact 7(1983) 213.

[Pa 85] J.D. Parsons, R.F. Bunshah, O.M. Stafsudd, Solid State Technol. (1985) 133.

[Pa 86] J.W. Palmour, R.F. Davis, T.M. Wallet, K.B. Bhasin, J.Vac.Sci.Technol. A4(1986)590.

[Pa 88] J.W. Palmour, H.S. Kong, R.F. Davis, J.Appl.Phys. 64(1988)2168.

[Pa 90] W.S. Pan, A.J. Steckl, J.Electrochem.Soc. 137(1990)212.

[Pa 91] R. Padiyath, R.L. Wright, M.I. Chaudry, S.V. Babu, Appl.Phys.Lett. 58(1991)1053.

[Pa 94] J.D. Parsons, G.B. Kruval, A.K. Chaddha, Appl.Phys.Lett. 65(1994)2075.

[Pa 95] G.D. Papasouliotis, S.V. Sotirchos, J. Electrochem.Soc. 142(1995)3834.

[Pi 87] P. Pirouz, C.M. Chorey, J.A. Powell, Appl. Phys. Lett. 50 (1987) 221.

[Po 64] P. Popper, I. Mohyuddin, Special Ceramics 3 (1964) 45.

[Po 87] J.A. Powell, L.G. Matus, M.A.Kuczmarski, J. Electrochem. Soc. 134 (1987) 1558.

[Po 90] J.A. Powell, D.J. Jarkin, L.G. Matus, W.J. Choyke, J.L. Bradshaw, L. Henderson, M. Yoganathan, J. Yang, P. Pirouz, Appl. Phys. Lett 56 (1990) 1353.

[Pr 95] J. Prokop, Dissertation Technical University of Munich, (1995).

[Ra 01] C. Raffy, L. Magaud, E. Blanquet, M. Pons and A. Pasturel, Materials Science Forum Vols. 353-356 (2001) pp. 111-114

[Ro 07] H.J. Round, Electr. World 19 (1907) 309.

[Ro 95] J. Rodrigues-Viejo, J. Stemenos, N. Clavaguera, M.T. Clavaguera-Mora, J. Cryst. Growth 155 (1995) 215.

[Sa 95] R. Sauer, Phys. B1 51 (1995) 399.

[Sc 69] P.T.B. Schaffer, R.G. Naum, J.Opt.Soc.Am. 59(1969) 1498.

[Sc 80] W. Schütz, Sprechsaa 1 113 (1980) 469.

[Sh 65] P.T.B. Schaffer, J. Am. Ceram. Soc. 48(1965)601.

[Se 86] B. Segall, S.A. Altterovitz, E.J. Haugland, L.G. Matus, Appl.Phys.Let. 49(1986)584.

[Sh 86] K. Shibahara, S. Nishino, H. Matsunami, J. Cryst. Growth 78 (1986) 538.

[Sh 87] K. Shihabara, S. Nishino, H. Matsunami, Appl. Phys. Lett. 50 (1987) 1888.

[Sh 87a] A. Sherman, Chemical Vapor Deposition for Microelectronics, Noyes Publications, Park Ridge, New Jersey (1987).

[Sh 92] J.S. Shor, R.M. Osgood, A.D. Kurtz, Appl.Phys.Lett. 60(1992)1001.

[Sh 94] J.S. Shor, R.A. Weber, L.G. Provost, D. Goldstein, A.D. Kurtz, J. Electrochem.Soc. 141(1994)579.

[Sh 95] V.B. Shields, M. A. Ryan, R.M. Williams, M. G. Spencer, D. M. Collins, D. Zhang, Inst. Phys. Conf. Ser. No. 142, Proceedings of the Sixth International Conference on Silicon Carbide and Related Materials (1995), Kyoto, Japan, edited by S. Nakashima, H. Matsunami, S. Yoshida, H. Harima, 1067.

[So 83] N.D. Sorokin, Yu.M. Tairov, V.F. Tsvetkov, M.A. Chernov, Dokl. Akad. Nauk SSSR 262, (1982) 1380/2; Soviet Phys. Dokl. 27, (1982) 170/1; Kristallografyia 28, (1983) 910/4.

[So 88] M.G. So, J.S. Chun, J. Vac. Sci. Technol. A6 (1988) 5.

[So 92] A. Solangi, M.I. Chaudry, J. Mater. Res. 7(1992) 539.

[St 92a] A.J. Steckl, S.A.Mogren, M.W. Roth, J.P. Li, Appl. Phys. Lett. 60 (1992) 1495.

[St 92b] A.J. Steckl, J.P. Li, Appl. Phys. Lett 60 (1992) 2107.

[St 93] A.J. Steckl, C. Yuan, J.P. Li, M.J. Loboda, Appl. Phys. Lett. 63 (1993) 3347.

[Su 75] A. Suzuki, M. Ikeda, H. Matsunami, T. Tanaka, J. Electrochem. Soc. 122 (1975) 1741.

[Su 84] A. Suzuki, K. Furukawa, Y. Higashigaki, S. Harada, S. Nakajima, T. Inoguchi, J. Cryst. Growth 70 (1984) 287.

[Su 86] A. Suzuki, A. Uemoto, M. Ghigeta, K. Furukawa, S. Nakajima, Appl.Phys.Lett. 49(1986)450.

[Su 95] C.M. Su, M. Wuttig, A. Fekade, M. Spencer, J. Appl. Phys. 77 (1995) 5611.

[Sy 94] B.S. Sywe, Z.J. Yu, S. Burckhard, J. Edgar, J. Chaudhuri, J. Electrochem. Soc. 141 (1994) 510.

[Ta 60] A. Taylor, R.M. Jones, Silicon Carbide - A High Temperature Semiconductor Eds. J.R. O'Conner, J. Smiltens, Pergamon Press (1960) 147.

[Ta 78] Yu.M. Tairov, V.F. Tsvertkov, J. Cryst. Growth 43 (1978) 209.

[Ta 81] Yu.M. Tairov, V.F. Tsvertkov, J. Cryst. Growth 52 (1981) 146.

[Ta 90] T. Tachibana, H.S. Kong, Y.C. Wang, R.F. Davis, J.Appl.Phys. 67(1990)6475.

[Ta 92] K. Takahashi, S. Nishino, J. Saraie, J. Electrochem. Soc 139 (1992) 3565.

[Ta 92a] K. Takahashi, S. Nishino, J. Saraie, Appl.Phys.Lett. 61(1992)2081.

[Ta 94] J. Takahashi, M. Kanaya, Y. Fujiwara, J. Cryst. Growth 135 (1994) 61.

[Ta 94a] S. Tanaka, R.S. Kern, R.F. Davis, Appl.Phys.Lett. 65(1994)2851.

[Ta 95] Yu.M. Tairov, Materials Science and Engineering B29 (1995) 83.

[Ti 95] C.C. Tin, R. Hu, R.L. Coston, J. Park, J. Cryst. Growth 148 (1995) 116.

[To 69] A. Todkill, R.W. Brander, Mater. Res. Bull. 4 (1969) 293.

[Tr 91] R.J. Trewm H.B. Yan, P.M. Mock, Proc. IEEE 79(1991)598.

[Ts 95] V.F. Tsvertkov, S.T. Allen, H.S. Kong, C.H. Charter Jr., Inst. Phys. Conf. Ser. No. 142, Proceedings of the Sixth International Conference on Silicon Carbide and Related Materials (1995), Kyoto, Japan, edited by S. Nakashima, H. Matsunami, S. Yoshida, H. Harima, 17.

[Ue 97] K. Ueno, Phys.Stat.Sol. A 162(1997)299.

[Ve 96] S. Veprek, Th. Kunstmann, Proc. of the 13th Int. Conf. on Chem. Vapor Deposition, eds. T.M. Besmann, M.D. Allendorf, McD. Dobinson, R.K. Ulrich, Los Angeles (1996), The Electrochem. Soc. Proceedings 96-5,(1996) 458.

[Vo 01] A.N. Vorobev, A.K. Semennikov, A.I. Zhmakin, Yu.N. Makarov, M. Dauesberg, F. Wischmeyer, M.Heuken and H. Jürgensen Materials Science Forum Vols. 353-356 (2001) pp. 103-106.

[Wa 93] Q. Wahab, R.C. Glass, I.P. Ivanhov, J.Birch, J.E. Sundgren, M.Wilander, J.Appl.Phys. 74(1993)1663.

[Wa 94] Q. Wahab, M.R. Sardela, L. Hultman, A. Henry, M. Wilander, E. Janzen, J.E. Sundgren, Appl. Phys.Lett.65(1994)725.

[Wa 01] G. Wagner and K. Irmscher, Material Science Forum Vols. 353-356(2001) pp. 95-98.

[We 96] West, R., Denk, M. Pure and Appl. Chem. (1996), 68, 785.

[Wu 96] C.H. Wu, C. Jacob, X.J. Ning, S. Nishino, P. Pirouz, J. Cryst. Growth 158 (1996) 480.

[Xi 95] W. Xie, Y. Wang, M.R. Melloch, J.A. Cooper, G.M. Johnson, L.A. Lipkin, J.W. Palmour, C.H. Charter, Inst.Phys.Conf.Ser.No. 142, Proceedings of the Sixth International Conference on Silicon Carbide and Related Materials (1995), Kyoto, Japan, edited by S. Nakashima, H. Matsunami, S. Yoshida, H. Harima, 785.

[Ya 95] K. Yasui, H. Fujita, N. Ninagawa, T. Akahane, Inst. Phys.Conf.Ser.No.142, Proceedings of the Sixth International Conference on Silicon Carbide and Related Materials (1995), Kyoto, Japan, edited by S. Nakashima, H. Matsunami, S. Yoshida, H. Harima, 253.

[Yi 95] P.H. Yih, A.J. Steckl, J. Electrochem.Soc. 142(1995)312.

[Yo 90] T. Yoshinobu, M. Nakayama, H. Shiomi, T. Fuyuki, H. Matsunami, J. Cryst. Growth 99(1990)520.

[Yu 94] C. Yuan, A.J. Steckl, M.J. Loboda, Appl. Phys. Lett. 64 (1994) 3000.

[Za 68] G. Zanmarchi, J. Phys. Chem. Solids 29(1968) 1727.

[Za 01] S. Zappe, J. Franklin, E. Obermeier, M. Eickhoff, H. Moeller, G. Kroetz, C. Rougeot, O. Lefort and J. Stoemenos. Materials Science Forum Vols. 353-356 (2001) pp. 753-756.

[Zh 90] Z. Zheng, R.E. Tressler, K.E. Spear, J. Electrochem Soc. 137(1990)854.

[Zi 83] G. Ziegler, P. Lanig, D. Theis, C. Weyrich, IEEE Trans. Electron Devices 30 (1983) 277.

[Zo 95] C.A. Zorman, A.J. Fleischman, A.S. Dewa, M. Mehregany, C. Jacob, S. Nishino, P. Pirouz, J. Appl. Phys. 78 (1995) 5136.

14 Acknowledgements

Special thanks to Prof. Dr. Stutzmann and Prof. Dr. Hiller for their support, for their personal help and for all kind of advice to this work.

Thanks to my friends:

Claudio Miskys and Dirk Etzdorf for the great ideas, suggestions and constant motivation to improve this work.

Thanks to the following colleagues:

Dr. J. Hofmann, Mr. A. Englert for the good work atmosphere in the group,

Dr. C. Ossadnik for the introduction into X ray diffraction and Raman spectroscopy,

Dr. J. Froh for the introduction into Scanning Electron Microscopy,

Dr. X. Wu, Dr. C. Eggs, Mrs. O. Rauchenecker, Dr. Glen Horton for help and collaboration,

Mr. G. Stohwasser for the maintenance of the electronic equipment,

Dr. R. Betrovitsk for the introduction to Hall measurements,

Dr. T. Bolom and Dr. C. Eggs for XPS measurements,

Mr. F. Riedmiller for the distillation of the methyltrichlorosilane precursor,

Dr. K. Moto, Dr. P. Nesládek, Mr. J. Procházka, Dr. C. Jun and Dr. A. Niederhofer for the great ideas and discussions in the field of chemistry,

Special thanks to my parents (Omar and Leonor Carnio Zaia) and Mrs. Stephanie Gebauer for their support and constant encouragements.

Finally, thanks to everyone who indirectly supported this thesis, cooperated with this work and is not mentioned above.